Technische Universität München

TUM School of Engineering and Design

PWM-based Sensorless Control of an Electrically Excited Synchronous Machine Using Mutual Induction

Han Byul Chung

Vollständiger Abdruck der von der TUM School of Engineering and Design der Technischen Universität München zur Erlangung des akademischen Grades eines

Doktors der Ingenieurwissenschaften (Dr.-Ing)

genehmigten Dissertation.

Vorsitzender: Prof. Dr.-Ing. Ulf Schlichtmann
Prüfer der Dissertation:
1. Prof. Dr.-Ing. Dr. h. c. Ralph Kennel
2. Prof. Dr.-Ing. Mario Pacas

Die Dissertation wurde am 10.11.2021 bei der Technischen Universität München eingereicht und durch die TUM School of Engineering and Design am 31.08.2022 angenommen.

Acknowledgements

First of all, I would like to express my profound gratitude to Prof. Ralph Kennel for giving me an opportunity to pursue my research topic. For the whole research period, I could actively make decisions and realize my ideas thanks to his advice and trust in me.
I also appreciate Prof. Mario Pacas for examining my dissertation. Furthermore, his research inspired me when I found a way forward in my research period.
The research in this dissertation has been carried out at the institute for Electrical Drive Systems and Power Electronics of the Technical University Munich. From building a hypothesis to its implementation, I could overcome many challenges with my colleagues' help. It was a great pleasure for me to work together with the EAL team. I would especially like to thank my friends Darshan Manoharan and Shih-Wei Su for their contribution to my research and the memory we shared.
Finally, I would like to thank my family for all the unconditional support. This dissertation could not be made without the love and support of Gahyun. Although it was not always easy, I felt happy every moment with you. Thank you always, Gahyun.

Seoul, in November 2022
Han Byul Chung

Abstract

An electrically excited synchronous machine (EESM) produces magnetic flux by electric current in the field winding. This unique characteristic gives an additional degree of freedom to the EESM model. The controllability of field flux enables a wide constant power range and high efficiency in the high-speed range without using rare-earth magnets.
The field winding also provides additional observability. Due to the mutual induction between the stator and the rotor windings, the field current signal contains the structural saliency of the machine. As the fundamental PWM switching in the stator winding induces the field current depending on the structural saliency, the mutually induced field current can be utilized to estimate the rotor position. Therefore, the PWM-based sensorless control using mutual induction is proposed in this thesis. The position estimation algorithm was derived from the geometric relationship between the stator active vector and the derivative of field current. For the realization of the method, practical issues, such as the current response delay and the insufficient active time, were analyzed. The corresponding modification methods were suggested and verified with the experimental results.
The experimental validation was performed in the wide-speed range, the reverse rotation, and the full load condition. Although the transient estimation error was higher than existing methods, the overall operation showed satisfactory performance without divergence. Therefore, the proposed method has achieved the sensorless control of EESM with the mutually induced field current by fundamental PWM switching. The proposed method can estimate the rotor position within one or two PWM cycles with simple arithmetic operations. Moreover, neither any parameter information nor the polarity detection method is required in the proposed method.

Contents

CHAPTER 1

Introduction

Since the discovery of the electromagnetic induction phenomenon by Faraday (1831), electric machines have been becoming essential in our daily life. In the beginning, electric machines were used only for industrial applications due to the machine's big size and their limitation in dynamic operation. However, machine design and control technology have been developed actively and combined with power electronics, materials technology, and micro-controllers. As a result, a high performance and efficient machine drive was achieved. The achievement made electric machines widely being used in various fields.

1.1 Electrically Excited Synchronous Machine

For different purposes of applications, various types of electric machines are developed, and each type of machines has different characteristics. Alternating current (AC) machines can be classified as Figure 1.1. Generally, the AC machine is classified as a synchronous machine and an induction machine (asynchronous machine) depending on the synchronization of the rotor operation with AC stator voltage. By the source of the field flux or the rotor structure, AC machines can be classified further in detail. Among the various types of machines, an interior permanent magnet synchronous machine (IPMSM) is one of the most popular machines in many

applications. Thanks to the high torque density and efficiency, a large percentage of electric vehicles (EVs) use IPMSM in their drivetrains [1, 2]. However, the permanent magnet (PM) used in IPMSM is rare-earth material, which causes unstable and high manufacturing costs. Accordingly, other machine types have been examined in many researches to find an alternative machine of IPMSM. An induction machine (IM) has the advantages of mechanical robustness and high reliability but has lower efficiency. A Synchronous reluctance machine (SynRM) has also been researched for traction applications but has not yet penetrated the market due to noise and vibrations. As another alternative, an electrically excited synchronous machine (EESM*) is getting more interest in recent researches [3–5].

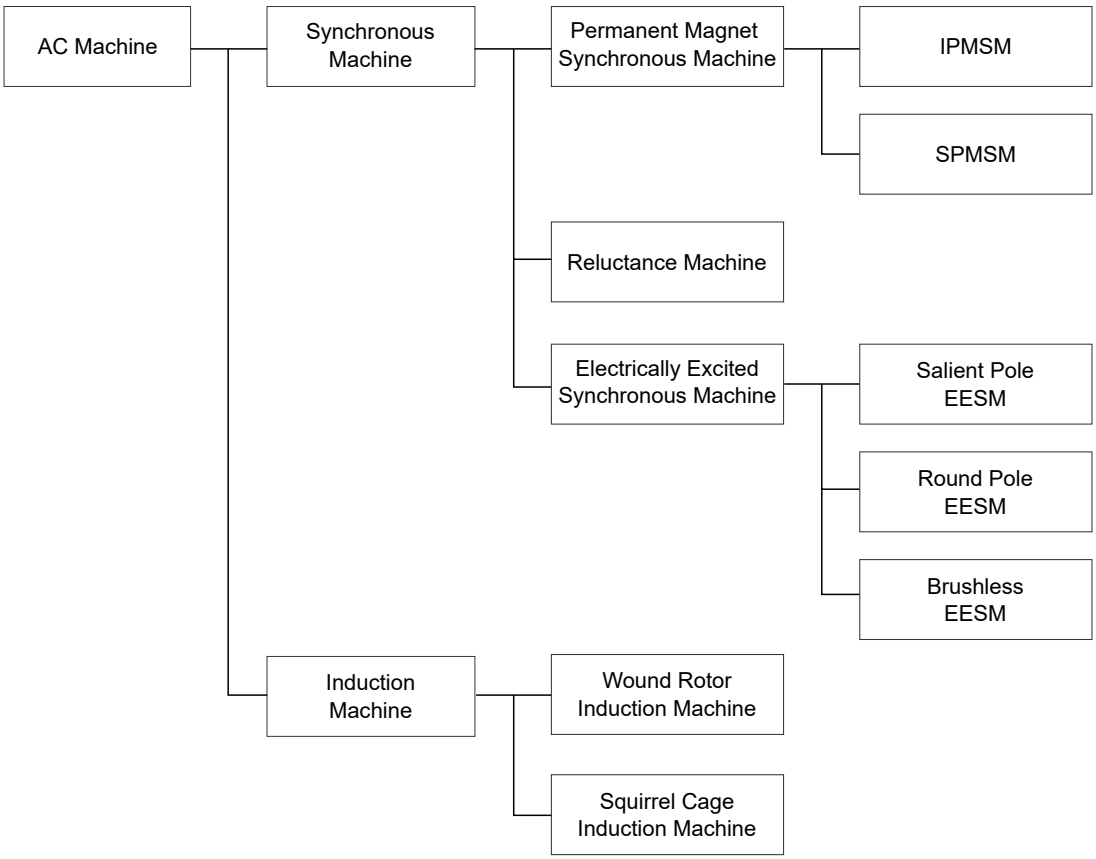

Figure 1.1: Classification of AC machines

The EESM is a synchronous machine and a non-PM machine with a field winding in a rotor to generate the magnetic flux. The rotor structures of IPMSM and salient pole EESM are depicted in Figure 1.2. EESM has field winding which produces the magnetic flux by applying current into the winding. While the field flux is constant in PMSM, the field flux of EESM can

*EESM is also called a wound rotor synchronous machine (WRSM) or a wound field synchronous machine (WFSM), but in this research, we use the term EESM.

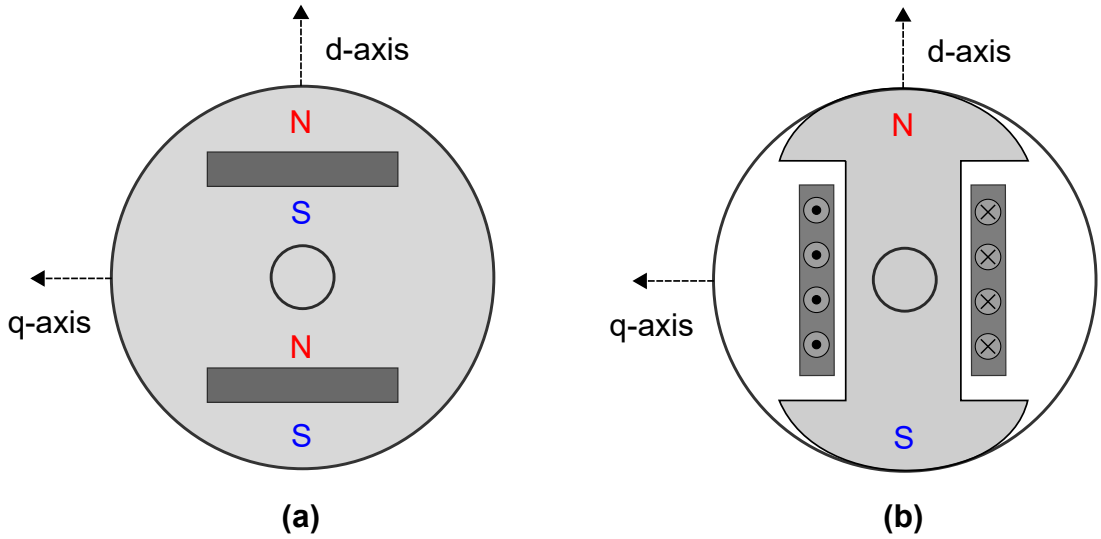

Figure 1.2: Rotor structures: (a) IPMSM and (b) EESM

be adjusted by controlling the field current. EESM has been preferred for high-power generating and motoring applications in the multi-MW range [6]. Due to the recent development of machine design, it is now also used for automotive traction applications in the market [7,8]. Especially, the applications of EESM to the micro-hybrid system[†] and mild-hybrid system[‡] have been actively researched [11, 12].

EESM has the following advantages compared to IPMSM:

1. Magnet-free
2. Wide-speed range operation with high-efficiency
3. Fail-safety in case of inverter failure

Owing to the field winding, EESM does not require a permanent magnet. As a result, the magnet-free structure prevents the unstable cost variation and a chance of demagnetization under the high-temperature condition. In addition, the controllability of the field flux enables the ideal field weakening control. Therefore, EESM has a wider constant power speed range and higher efficiency in the high-speed range than PMSM [13, 14]. On the other hand, since EESM does not induce electromotive force (EMF) in case of inverter failure, it has inherent fail-safety even in the high-speed region [15]. Those advantages satisfy the main requirements

[†]A micro hybrid system primarily has auto start-stop functionality with less than 5 kW power capability [9].

[‡]A mild hybrid system is a type of hybrid system that assists engine torque and regenerates braking force within a limited output power. The electric machine in mild hybrids is rated between 5 and 20 kW [10].

for a traction application, such as high torque output at the low-speed range, high efficiency, and wide-speed operation range.

The use of brush and the copper loss in the field winding are the main concerns of EESM. The wear of brush can reduce the mechanical robustness of the machine. However, it was claimed that the coal brushes in the slip ring wear less than those in direct current (DC) machines and are practically maintenance-free [16]. On the other hand, brushless EESM has been actively researched to eliminate the problem caused by the brush and slip ring structure [17–19]. Regarding the concern of the copper loss in the field winding, the optimal control that considers the copper loss of the field winding was studied to prevent the low system efficiency and thermal problem [20]. Considering the advantages and the solutions for the disadvantages of EESM, EESM is expected to be used in more applications, especially in automotive traction applications. Therefore, this thesis deals with the EESM and a control method for EESM.

1.2 Related Works

In terms of the machine control method, the vector control or the field-oriented control (FOC) method enabled high performance and efficiency control. The vector control controls the magnitude and the direction of the current vector with respect to the field flux vector. The control method enables decoupled control of flux and torque, thus achieving instantaneous torque control. However, it also increases the dependency on the position sensor in machine control. The position sensor, such as a resolver and an encoder, requires hardware cost, installation space, cables, and additional signal processing integrated circuits (ICs). As a result, the position sensor can restrict the usage in various applications and reduce the system's reliability. Therefore, to overcome the side effects of the position sensor, sensorless control [§] has been suggested and actively researched. Sensorless control is a vector control method with estimated position. Thus the position sensor can be removed.

Based on the position estimation principle, sensorless control is classified as a model-based method and a saliency-based method. The model-based method uses the EMF and shows excellent performance in the middle- and high-speed range. However, the method depends on model parameters and fails to estimate position in a standstill or low-speed range. The saliency-based method estimates the rotor position by injecting high-frequency (HF) signal in general. Com-

[§]It is correct to refer to the control method as "encoderless control" or "self-sensing control," but this study follows the common terminology, "sensorless control."

pared to the model-based method, the saliency-based method shows excellent performance in a standstill and the low-speed range, but its application is limited in the high-speed range due to the decreasing control voltage margin. Therefore, both methods need to be combined to control the machine from a standstill to a high-speed range. However, the combination of two methods requires a strategy for the transition region to prevent unstable operation. Therefore, this thesis aims to design a sensorless control method that can work in a wide speed range with a single algorithm.

Sensorless control of EESM has been researched in a number of publications. As a unique characteristic of EESM, the rotor winding gives more chances in the design of the sensorless control method. Regarding the saliency-based method, the rotor winding was exploited as excitation winding of HF signal injection in [21–23]. In [21], the HF voltage signal was injected into the rotor winding, and the corresponding current response was detected in the stator winding. Since this method was affected by the cross-coupling effect, the estimation method was compensated with a lookup table of model parameters. The experimental results showed good torque control performance for a standstill and the low-speed range. On the contrary, the rotor winding was used to detect HF response induced by the injected carrier signal into the stator winding [24, 25]. The HF voltage signal was injected into the stator winding in the papers, and the current response in the rotor winding was investigated. The proposed method was validated experimentally and showed satisfactory control performance in the low-speed range, including standstill condition.

As an attempt to reduce the side effects of signal injection, a fundamental rotor switching signal was used as an HF carrier signal. Generally, due to the different time constant of the rotor and the stator windings, the two switching frequencies are different. The frequency of mutually induced stator voltage is decided by the rotor switching frequency, which differs from the stator switching frequency. Therefore, the mutually induced stator voltage can be extracted from the fundamental stator switching voltage by a filter such as a bandpass filter. As the mutually induced voltage contains the saliency of a machine, the rotor switching can be used as an HF carrier signal. In [22], fundamental rotor switching voltage was exploited as a carrier signal, and the stator current response was obtained with a frequency demodulation method. Besides, the fundamental rotor current ripple was also employed as a carrier signal [23]. The mutually induced voltage in the stator winding was evaluated, and then the rotor position was estimated. Both methods showed satisfactory estimation performance from a standstill to the low-speed range with the fundamental switching signal in the rotor winding. In summary, the saliency-based method of EESM has been researched based on the relationship between the injected

carrier signal and its response in the other winding. Those methods showed good results in a standstill and the low-speed range. However, the estimation performance deteriorated over the middle-speed range. Moreover, the bandwidth of the current controller is limited by the signal injection. Thus the dynamic performance of a machine is also limited.

The model-based method of EESM has been researched in a certain number of papers [23, 25, 26]. The concept of active flux was suggested in [26], and the disturbance observer (DO) was applied to calculate the EMF of the machine [23]. Since the magnitude of EMF is proportional to the rotor speed, the method guarantees the estimation performance mainly in the middle- and high-speed range. Therefore, the model-based method has been combined with the saliency-based method for a whole speed range sensorless control method [23, 25]. The proposed methods showed satisfactory estimation performance for a whole speed range with experimental results. The transition region and the switch-over strategy should be decided carefully for a stable transition between the two methods.

As a new approach, the pulse-width modulation (PWM)-based sensorless control was proposed in [27–29]. In those methods, the fundamental PWM switching voltage or PWM frequency injection signal was considered as HF carrier signal, and corresponding current response was used to estimate the rotor position. In [27], a current derivative sensor was used to measure the current response. In [28], the derivative of current was computed by calculating the current slope while an active voltage vector was applied. PWM frequency signal injection was proposed in [29], and both rotating and pulsating signal injection were applied. Although the PWM-based method requires a high sampling rate, it can estimate the rotor position over a wide speed range with a single algorithm.

1.3 Contribution

The PWM-based sensorless control of EESM using mutual induction is proposed in this thesis. The change of stator flux and rotor flux of EESM induces EMF mutually, and this phenomenon is referred to as mutual induction. The mutual inductance can be expressed as a function of the angle between the stator and the rotor windings. The proposed method estimates the rotor position by evaluating the mutually induced current in the rotor winding by fundamental PWM switching voltage in the stator winding. Following advantages are expected by the proposed method:

1. Wide-speed range operation with a single algorithm

2. Parameter-free estimation

3. Simple estimation algorithm

Firstly, the proposed method works for a wide-speed range by using the fundamental PWM switching voltage. Due to the high frequency of PWM switching and no signal injection in the high-speed range, a wide-speed range operation can be achieved with a single algorithm. Only for the case that the stator reference voltage is too low to induce the measurable amplitude of rotor current, signal injection is applied. Secondly, the estimation equation does not require any parameter information. Since the position can be estimated only with measured current and voltage command, parameter uncertainty does not affect the proposed method. Lastly, the proposed method can estimate the rotor position by calculating the current slope during a PWM cycle. Therefore the estimation consists of simple arithmetic operations and does not require complex frequency demodulation methods.

1.4 Structure

This chapter has introduced EESM and sensorless control methods of EESM. Based on the technical background, the research topic of this thesis was defined. Following this introduction, Chapter 2 explains the model of EESM, which is essential to derive the proposed method in this study. Also, the unique feature of EESM, the mutual induction between the stator and the rotor windings, is analyzed in detail. Chapter 3 presents the state of the art of sensorless control methods for EESM. Based on the estimation principle, related researches are classified as the saliency-based method and the model-based method. Additionally, recent researches on the PWM-based method are explained at the end of the chapter.

Chapter 4 describes the PWM-based sensorless control of EESM using mutual induction, which is the topic of this thesis. Firstly, the proposed method is derived theoretically from the mathematical model. Secondly, practical issues and related modification methods are presented in detail. Thirdly, the configuration of the test bench is given to describe the experimental environments. The experimental validation is carried out with the modification methods and presented at the end of the chapter. Finally, Chapter 5 presents the conclusion of this thesis.

CHAPTER 2

Electric Machine Model

A model describes system behavior with mathematical equations. It is the basis of system analysis and controller design. In this chapter, a reference frame theory is explained to express the EESM model. And then, the EESM model is introduced and analyzed. In the last section, the mutual inductance between the stator and the rotor winding, which is the main parameter in the proposed position estimation algorithm, is analyzed in detail.

2.1 Reference Frame Theory

2.1.1 Symbols and nomenclature

The symbol notation used in this study is introduced to clarify the meaning of symbols in mathematical equations. The basic form of a symbol is given as

$$\boldsymbol{x}_i^j \tag{2.1}$$

where x, i, and j represent a variable, a winding associated with the variable, and a reference frame. For example, u_s^r means a voltage variable of the stator winding in the rotor reference

Superscript	Description
s	Stator reference frame
r	Rotor reference frame
a	Arbitrary reference frame

Table 2.1: List of superscripts

Subscript	Description
a, b, c	a-, b-, and c-phase stator windings
α, β	α- and β-axis stator windings
d, q	d- and q-axis stator windings
f	Field winding (rotor winding)

Table 2.2: List of subscripts

frame. Lists of superscripts and subscripts used in the model are summarized in Table 2.1 and Table 2.2.

2.1.2 Reference frame transformation

The electric machine model is expressed as a time-varying system. The time-varying model equations give difficulties in analyzing and controlling the model behavior. By transforming the model equations to a different reference frame, the time-invariant model equations can be obtained. Also, the number of model variables can be reduced. As a result, the analysis and the controller design become more straightforward.

Figure 2.1 shows the relationship between different reference frame axes. In the symmetric three-phase electric machine, the three windings have a $2\pi/3$ rad spatial displacement to each other and consist of a-, b-, and c-axis. The stator reference frame, which is depicted with red color, is a stationary frame and consists of α- and β-axis. The α-axis is defined to be aligned with the a-axis. The β-axis is defined as orthogonal to the α-axis and $\pi/2$ rad ahead of the α-axis in the rotating direction. The rotor reference frame consists of a direct axis (d-axis) and a quadrature axis (q-axis) and is depicted with a blue dotted line in Figure 2.1. The d-axis is defined to be aligned with a rotor flux direction in the rotor reference frame. The q-axis is $\pi/2$ rad ahead of the d-axis in the rotating direction. The rotor reference frame rotates as the rotor rotates with respect to the stator frame, and both rotations are synchronized together. There is one more axis in the stator and the rotor reference frame, the neutral axis (n-axis), which is perpendicular to the other two axes. Since the n-axis is orthogonal to the plane, where the rotating magnetic field is placed, it does not contribute to the torque generation but losses [30].

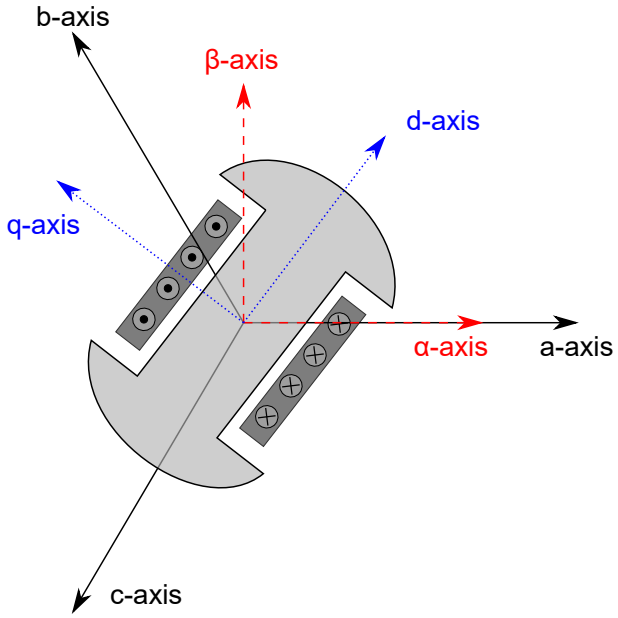

Figure 2.1: Axes of various reference frames

Therefore, the n-axis is not considered in this study under the definition that the three windings are balanced ($f_a + f_b + f_c = 0$), and the neutral point is in an open connection.

The transformation of the three-phase variables to the stator reference frame is a vector projection process shown in Figure 2.2. The three-phase variables can be projected on the α- and β-axes, and the projection results in two stator variables in the stator reference frame.

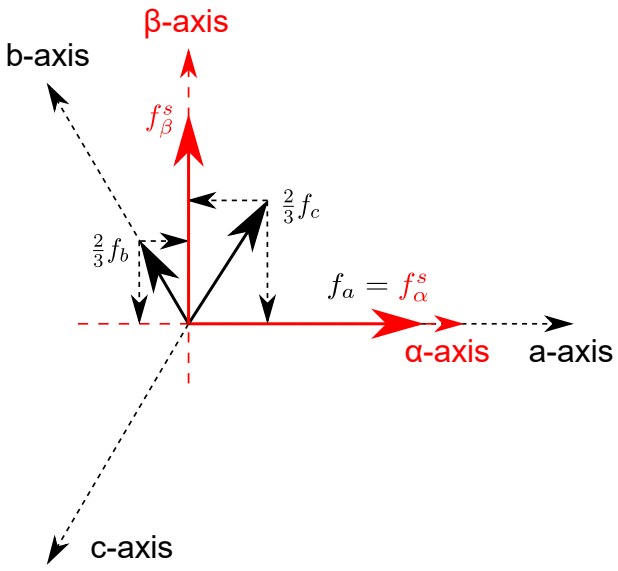

Figure 2.2: Transformation to the stator reference frame

By the vector projection process in Figure 2.2, the transformation equation is expressed as

$$\begin{aligned} f_\alpha^s &= \frac{2}{3}(f_a \cos 0 + f_b \cos \frac{2\pi}{3} + f_c \cos \frac{-2\pi}{3}) \\ &= \frac{2f_a - f_b - f_c}{3} \end{aligned} \tag{2.2}$$

$$\begin{aligned} f_\beta^s &= \frac{2}{3}(f_a \sin 0 + f_b \sin \frac{2\pi}{3} + f_c \sin \frac{-2\pi}{3}) \\ &= \frac{f_b - f_c}{\sqrt{3}} \end{aligned} \tag{2.3}$$

where f represents a variable such as voltage, current, and flux linkage of electric machines. This transformation is also called as Clarke transformation. In the transformation, the constant $2/3$ is multiplied to make the variable's amplitude the same after the transformation. However, the constant causes the variance of power after the transformation. Therefore, $3/2$ should be multiplied when calculating power with the transformed variables. Equations (2.2) and (2.3) can be expressed in a matrix form as

$$\boldsymbol{f}_s^s = \begin{bmatrix} f_\alpha^s \\ f_\beta^s \end{bmatrix} = \boldsymbol{T}_c \boldsymbol{f}_{abc} = \frac{2}{3} \begin{bmatrix} 1 & -\frac{1}{2} & -\frac{1}{2} \\ 0 & \frac{\sqrt{3}}{2} & -\frac{\sqrt{3}}{2} \end{bmatrix} \begin{bmatrix} f_a \\ f_b \\ f_c \end{bmatrix} \tag{2.4}$$

where $\boldsymbol{T}_c$ represents the Clarke transformation matrix. The transformation of the variables in the stator reference frame to the three-phase variables is expressed simply with the inverse matrix of the $\boldsymbol{T}_c$, and the equation is given as

$$\boldsymbol{f}_{abc} = \begin{bmatrix} f_a \\ f_b \\ f_c \end{bmatrix} = \boldsymbol{T}_c^{-1} \boldsymbol{f}_s^s = \begin{bmatrix} 1 & 0 \\ -\frac{1}{2} & \frac{\sqrt{3}}{2} \\ -\frac{1}{2} & -\frac{\sqrt{3}}{2} \end{bmatrix} \begin{bmatrix} f_\alpha^s \\ f_\beta^s \end{bmatrix} \tag{2.5}$$

The transformation of the stator reference frame to the rotor reference frame is a vector rotation process, as shown in Figure 2.3. The rotor reference frame is a rotating frame, and the rotating angle and the angular velocity are given as θ and ω. As the reference frame is synchronized with the rotor rotation, the rotating angle of the reference frame equals an electrical angle of the rotor. The electrical angle is defined as the number of pole pairs times the mechanical angle of the rotor.

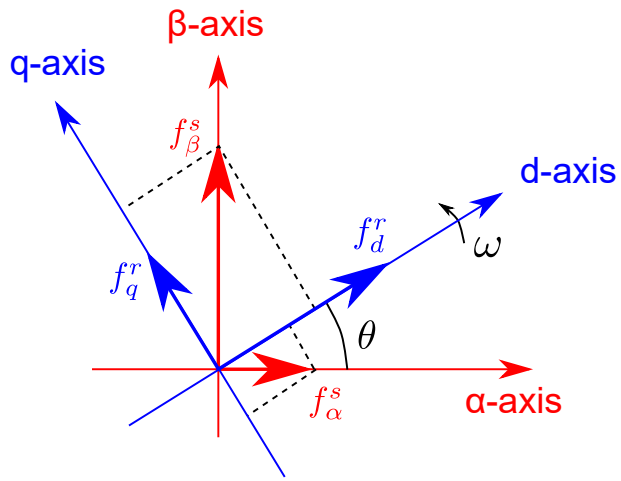

Figure 2.3: Transformation to the rotor reference frame

The transformation is expressed as

$$f^r_d = f^s_\alpha \cos\theta + f^s_\beta \sin\theta \tag{2.6}$$

$$f^r_q = -f^s_\alpha \sin\theta + f^s_\beta \cos\theta \tag{2.7}$$

where θ is defined as the angle from α-axis to d-axis. This transformation is called as Park transformation. Equations (2.6) and (2.7) can be expressed in a matrix form as

$$\boldsymbol{f}^r_s = \begin{bmatrix} f^r_d \\ f^r_q \end{bmatrix} = \boldsymbol{T}_p \boldsymbol{f}^s_s = \begin{bmatrix} \cos\theta & \sin\theta \\ -\sin\theta & \cos\theta \end{bmatrix} \begin{bmatrix} f^s_\alpha \\ f^s_\beta \end{bmatrix} \tag{2.8}$$

where $\boldsymbol{T}_p$ represents the Park transformation matrix.

As shown in (2.8), model variables in the stator reference frame can be easily transformed to the rotor reference frame. With the inverse transformation matrix of $\boldsymbol{T}_p$, the transformation of the rotor reference frame to the stator reference frame is given as

$$\boldsymbol{f}^s_s = \begin{bmatrix} f^s_\alpha \\ f^s_\beta \end{bmatrix} = \boldsymbol{T}_p^{-1} \boldsymbol{f}^r_s = \begin{bmatrix} \cos\theta & -\sin\theta \\ \sin\theta & \cos\theta \end{bmatrix} \begin{bmatrix} f^r_d \\ f^r_q \end{bmatrix} \tag{2.9}$$

By the Clarke and Park transformation, variables of electric machines can be transformed to a different reference frame. As a generalized reference frame transformation, the arbitrary reference frame transformation is presented in [31]. The arbitrary reference frame is a rotating

reference frame, which rotates with an arbitrary rotating angle. The transformation is expressed as

$$\boldsymbol{f}_s^a = \begin{bmatrix} f_d^a \\ f_q^a \\ f_n^a \end{bmatrix} = \boldsymbol{T}(\theta)\boldsymbol{f}_{abc} = \frac{2}{3}\begin{bmatrix} \cos\theta & \cos(\theta - \frac{2\pi}{3}) & \cos(\theta + \frac{2\pi}{3}) \\ -\sin\theta & -\sin(\theta - \frac{2\pi}{3}) & -\sin(\theta + \frac{2\pi}{3}) \\ \frac{1}{2} & \frac{1}{2} & \frac{1}{2} \end{bmatrix}\boldsymbol{f}_{abc} \tag{2.10}$$

where $\boldsymbol{f}_s^a$ and $\boldsymbol{T}$ represent the stator variables in the arbitrary reference frame and the arbitrary reference frame transformation matrix. The transformation matrix can be the Clarke or Park transformation matrix, depending on the arbitrary rotating angle. By substituting 0 for θ, the transformation becomes the transformation to the stator reference frame, and by substituting the rotor angle for θ, it becomes the transformation to the rotor reference frame.

By the reference frame transformation, model variables can be easily expressed in a different reference frame. Although the mathematical models in the stator and the rotor reference frame describe the same behavior of an electrical machine, each model provides a different perspective in analyzing the machine's behavior. In the following section, the EESM models in the stator and the rotor reference frame are presented.

2.2 Electrically Excited Synchronous Machine Model

The electric machine used in this study is a salient pole EESM, which is designed for a mild hybrid system of a vehicle. The machine has no damper winding in the rotor structure. The EESM structure on different reference frames is displayed in 2.1, and further information on the machine can be found in Appendix B. A voltage equation of electric machines consists of voltage drop by winding resistance and induced voltage by the change of flux linkage in windings. By Ohm's law and Faraday's law, the voltage equations for the three-phase stator windings and the rotor winding are expressed as [30]

$$\boldsymbol{u}_{abc} = \boldsymbol{R}_s\boldsymbol{i}_{abc} + \frac{d}{dt}\boldsymbol{\psi}_{abc} \tag{2.11}$$

$$u_f = R_f i_f + \frac{d}{dt}\psi_f \tag{2.12}$$

where u, i, and ψ are voltage, current, and flux linkage, respectively. The field winding is the rotor winding in EESM. R_s and R_f denote stator winding resistance and field winding resistance. The variables written with a bold character represent vector variables, and they are given as

$$\boldsymbol{u}_{abc} = \begin{bmatrix} u_a & u_b & u_c \end{bmatrix}^T \tag{2.13}$$

$$\boldsymbol{i}_{abc} = \begin{bmatrix} i_a & i_b & i_c \end{bmatrix}^T \tag{2.14}$$

$$\boldsymbol{R}_s = \begin{bmatrix} R_s & 0 & 0 \\ 0 & R_s & 0 \\ 0 & 0 & R_s \end{bmatrix} \tag{2.15}$$

$$\boldsymbol{\psi}_{abc} = \begin{bmatrix} \psi_a & \psi_b & \psi_c \end{bmatrix}^T \tag{2.16}$$

With the transformation matrix explained in the previous section, this model can be expressed in the stator and the rotor reference frame. To transform the three-phase variables to the arbitrary reference frame, the transformation matrix is multiplied to the equation in (2.11) as

$$\boldsymbol{T}(\theta)\boldsymbol{u}_{abc} = \boldsymbol{T}(\theta)\boldsymbol{R}_s\boldsymbol{i}_{abc} + \boldsymbol{T}(\theta)\frac{d}{dt}\boldsymbol{\psi}_{abc} \tag{2.17}$$

By transforming the three-phase current and flux linkages vectors to the arbitrary reference frame with the inverse transformation matrix, (2.17) can be rewritten as

$$\boldsymbol{T}(\theta)\boldsymbol{u}_{abc} = \boldsymbol{T}(\theta)\boldsymbol{R}_s(\boldsymbol{T}^{-1}(\theta)\boldsymbol{i}_s^a) + \boldsymbol{T}(\theta)\frac{d}{dt}(\boldsymbol{T}^{-1}(\theta)\boldsymbol{\psi}_s^a) \tag{2.18}$$

$$\boldsymbol{u}_s^a = \boldsymbol{R}_s\boldsymbol{i}_s^a + \boldsymbol{T}(\theta)\frac{d}{dt}(\boldsymbol{T}^{-1}(\theta)\boldsymbol{\psi}_s^a) \tag{2.19}$$

where $\boldsymbol{T}(\theta)\boldsymbol{R}_s\boldsymbol{T}^{-1}(\theta) = \boldsymbol{R}_s$ by the property of the transformation matrix. Using the product rule of the derivatives, (2.19) becomes

$$\begin{aligned} \boldsymbol{u}_s^a &= \boldsymbol{R}_s\boldsymbol{i}_s^a + \boldsymbol{T}(\theta)\frac{d}{dt}\boldsymbol{T}^{-1}(\theta)\boldsymbol{\psi}_s^a + \boldsymbol{T}(\theta)\boldsymbol{T}^{-1}(\theta)\frac{d}{dt}\boldsymbol{\psi}_s^a \\ &= \boldsymbol{R}_s\boldsymbol{i}_s^a + \boldsymbol{T}(\theta)\frac{d}{dt}\boldsymbol{T}^{-1}(\theta)\boldsymbol{\psi}_s^a + \frac{d}{dt}\boldsymbol{\psi}_s^a \end{aligned} \tag{2.20}$$

Applying the chain rule to the time derivative in the second term on the right-hand side, (2.20) becomes

$$\boldsymbol{u}_s^a = \boldsymbol{R}_s \boldsymbol{i}_s^a + \boldsymbol{T}(\theta)\frac{\partial}{\partial\theta}\frac{\partial\theta}{\partial t}\boldsymbol{T}^{-1}(\theta)\boldsymbol{\psi}_s^a + \frac{d}{dt}\boldsymbol{\psi}_s^a \tag{2.21}$$

where $\frac{\partial\theta}{\partial t} = \omega$ and by taking the derivative of $\boldsymbol{T}^{-1}(\theta)$ with respect to θ, (2.21) becomes

$$\boldsymbol{u}_s^a = \boldsymbol{R}_s \boldsymbol{i}_s^a + \omega \boldsymbol{J}\boldsymbol{\psi}_s^a + \frac{d}{dt}\boldsymbol{\psi}_s^a \tag{2.22}$$

where the matrix $\boldsymbol{J}$ is given as

$$\boldsymbol{J} = \boldsymbol{T}(\theta)\frac{\partial}{\partial\theta}\boldsymbol{T}^{-1}(\theta) = \begin{bmatrix} 0 & -1 & 0 \\ 1 & 0 & 0 \\ 0 & 0 & 0 \end{bmatrix} \tag{2.23}$$

Based on the voltage equation in the arbitrary reference frame shown in (2.22), the voltage equation in the stator or the rotor reference frame can be obtained by substituting zero or the rotor angle for the arbitrary rotating angle. The voltage equation of the rotor winding has the same form in (2.12) regardless of the type of a reference frame since the variables of the rotor winding are scalar values and independent from the rotor angle.

The flux linkage equations of the stator winding and rotor winding are given as [30]

$$\boldsymbol{\psi}_{abc} = \boldsymbol{L}_{abc}\boldsymbol{i}_{abc} + \boldsymbol{M}_{sf} i_f \tag{2.24}$$

$$\psi_f = L_f i_f + \left(\boldsymbol{M}_{sf}\right)^T \boldsymbol{i}_{abc} \tag{2.25}$$

where $\boldsymbol{L}_{abc}$, $\boldsymbol{M}_{sf}$, and L_f represent the stator inductance matrix, the mutual inductance matrix between the stator and the field windings, and the field winding inductance.

The inductance matrix of the stator winding is defined as

$$\boldsymbol{L}_{abc} = \begin{bmatrix} L_{aa} & L_{ab} & L_{ac} \\ L_{ba} & L_{bb} & L_{bc} \\ L_{ca} & L_{cb} & L_{cc} \end{bmatrix} \tag{2.26}$$

where L_{ij} represents the inductance between i- and j- phase windings, i.e., the diagonal ele-

ments are stator self-inductance, and the other elements are stator mutual inductance of each winding. Also, $L_{ij} = L_{ji}$ because the circuit is reciprocal. Since a salient synchronous machine has a variable effective air gap, the inductance varies depending on the air gap, which is decided by the rotor position. Therefore, the inductance is expressed as a function of the rotor position. The stator inductance matrix can be expressed as

$$\boldsymbol{L}_{abc} = \begin{bmatrix} L_{ls} + L_A + L_B \cos 2\theta_r & -\frac{1}{2}L_A + L_B \cos 2\left(\theta_r - \frac{\pi}{3}\right) & -\frac{1}{2}L_A + L_B \cos 2\left(\theta_r + \frac{\pi}{3}\right) \\ -\frac{1}{2}L_A + L_B \cos 2\left(\theta_r - \frac{\pi}{3}\right) & L_{ls} + L_A + L_B \cos 2\left(\theta_r + \frac{\pi}{3}\right) & -\frac{1}{2}L_{_A} + L_B \cos 2\theta_r \\ -\frac{1}{2}L_A + L_B \cos 2\left(\theta_r + \frac{\pi}{3}\right) & -\frac{1}{2}L_{_A} + L_B \cos 2\theta_r & L_{ls} + L_A + L_B \cos 2\left(\theta_r - \frac{\pi}{3}\right) \end{bmatrix} \tag{2.27}$$

where L_{ls}, L_A, L_B, and θ_r represent leakage inductance, the average value of magnetizing inductance, the amplitude of magnetizing inductance varying component, and the rotor position. As shown in (2.27), the stator inductance matrix is expressed with the rotor position.

The mutual inductance between the stator and the field winding is also dependent on the rotor position. By the spatial relationship of the three-phase winding and the field winding, the mutual inductance matrix is given as

$$\boldsymbol{M}_{sf} = M_{sf} \begin{bmatrix} \cos\theta_r & \cos\left(\theta_r - \frac{2\pi}{3}\right) & \cos\left(\theta_r + \frac{2\pi}{3}\right) \end{bmatrix}^T \tag{2.28}$$

where M_{sf} is the maximum value of the mutual inductance.

The flux linkage equation of stator winding can be transformed to the arbitrary reference frame analogously to the transformation of voltage equations.

$$\begin{aligned} \boldsymbol{T}(\theta)\,\boldsymbol{\psi}_{abc} &= \boldsymbol{T}(\theta)\,\boldsymbol{L}_{abc}\boldsymbol{i}_{abc} + \boldsymbol{T}(\theta)\,\boldsymbol{M}_{sf} i_f \\ &= \boldsymbol{T}(\theta)\,\boldsymbol{L}_{abc}(\boldsymbol{T}^{-1}(\theta)\,\boldsymbol{i}_s^a) + \boldsymbol{T}(\theta)\,\boldsymbol{M}_{sf} i_f \end{aligned} \tag{2.29}$$

By rearranging (2.29), the flux linkage equation in the arbitrary reference frame is given as

$$\begin{aligned} \boldsymbol{\psi}_s^a &= \left(\boldsymbol{T}(\theta)\,\boldsymbol{L}_{abc}\boldsymbol{T}^{-1}(\theta)\right)\boldsymbol{i}_s^a + \boldsymbol{T}(\theta)\,\boldsymbol{M}_{sf} i_f \\ &= \boldsymbol{L}_s^a\,\boldsymbol{i}_s^a + \boldsymbol{M}_{sf}^a\,i_f' \end{aligned} \tag{2.30}$$

where i'_f is the field current scaled to the stator side, and the scaled field current is expressed as

$$i'_f = \frac{2}{3}\frac{N_f}{N_s}\, i_f \tag{2.31}$$

where N_f and N_s represent the effective number of turns of the field winding and the stator winding. The prime symbol is used to express the scaled value of the field variables and parameters.

In (2.30), the calculation results of inductance matrices are given as

$$\boldsymbol{L}_s^a = \begin{bmatrix} L_{ls} + \frac{3}{2}\left(L_A + L_B \cos 2\left(\theta - \theta_r\right)\right) & -\frac{3}{2} L_B \sin 2\left(\theta - \theta_r\right) & 0 \\ -\frac{3}{2} L_B \sin 2\left(\theta - \theta_r\right) & L_{ls} + \frac{3}{2}\left(L_A - L_B \cos 2\left(\theta - \theta_r\right)\right) & 0 \\ 0 & 0 & L_{ls} \end{bmatrix} \tag{2.32}$$

$$\boldsymbol{M}_{sf}^a = M_{sf} \begin{bmatrix} \cos\left(\theta - \theta_r\right) \\ -\sin\left(\theta - \theta_r\right) \\ 0 \end{bmatrix} \tag{2.33}$$

In both inductance matrices, the elements in the third row are related to the n-axis of EESM. As mentioned in the previous section, the n-axis variable is not considered in the EESM model. Therefore, (2.32) and (2.33) are rewritten as

$$\boldsymbol{L}_s^a = \begin{bmatrix} L_{ls} + \frac{3}{2}\left(L_A + L_B \cos 2\left(\theta - \theta_r\right)\right) & -\frac{3}{2} L_B \sin 2\left(\theta - \theta_r\right) \\ -\frac{3}{2} L_B \sin 2\left(\theta - \theta_r\right) & L_{ls} + \frac{3}{2}\left(L_A - L_B \cos 2\left(\theta - \theta_r\right)\right) \end{bmatrix} \tag{2.34}$$

$$\boldsymbol{M}_{sf}^a = M_{sf} \begin{bmatrix} \cos\left(\theta - \theta_r\right) \\ -\sin\left(\theta - \theta_r\right) \end{bmatrix} \tag{2.35}$$

The voltage and flux linkage equations of EESM in the stator reference frame can be obtained by substituting zero for the arbitrary rotating angle. The EESM model in the stator reference frame is expressed as

$$\boldsymbol{u}_s^s = \boldsymbol{R}_s \boldsymbol{i}_s^s + \omega \boldsymbol{J} \boldsymbol{\psi}_s^s + \frac{d}{dt}\boldsymbol{\psi}_s^s \tag{2.36}$$

$$u'_f = R'_f i'_f + \frac{d}{dt}\psi'_f \tag{2.37}$$

where the stator voltage, current, flux linkages, and stator winding resistance are given as

$$\boldsymbol{u}_s^s = \begin{bmatrix} u_\alpha & u_\beta \end{bmatrix}^T \tag{2.38}$$

$$\boldsymbol{i}_s^s = \begin{bmatrix} i_\alpha & i_\beta \end{bmatrix}^T \tag{2.39}$$

$$\boldsymbol{\psi}_s^s = \begin{bmatrix} \psi_\alpha & \psi_\beta \end{bmatrix}^T \tag{2.40}$$

$$\boldsymbol{R}_s = \begin{bmatrix} R_s & 0 \\ 0 & Rs \end{bmatrix} \tag{2.41}$$

The flux linkage equation in the stator reference frame is given as

$$\boldsymbol{\psi}_s^s = \boldsymbol{L}_s^s \boldsymbol{i}_s^s + \boldsymbol{M}_{sf}^s i_f' \tag{2.42}$$

$$\psi_f' = L_f' i_f' + (\boldsymbol{M}_{sf}^s)^T \boldsymbol{i}_s^s. \tag{2.43}$$

where the inductance and mutual inductance matrices are given as

$$\boldsymbol{L}_s^s = \begin{bmatrix} L_{ls} + \frac{3}{2}\left(L_A + L_B \cos 2\theta_r\right) & \frac{3}{2} L_B \sin 2\theta_r \\ \frac{3}{2} L_B \sin 2\theta_r & L_{ls} + \frac{3}{2}\left(L_A - L_B \cos 2\theta_r\right) \end{bmatrix} \tag{2.44}$$

$$\boldsymbol{M}_{sf}^s = M_{sf} \begin{bmatrix} \cos\theta_r \\ \sin\theta_r \end{bmatrix} \tag{2.45}$$

Since the stator reference frame is stationary regardless of machine rotation, the model in the stator reference frame is expressed as time-varying equations and dependent on the rotor position.

The voltage and flux linkage equations of EESM in the rotor reference frame can be obtained by substituting the rotor angle for the arbitrary rotating angle. The EESM model in the rotor reference frame is expressed as [32]

$$\boldsymbol{u}_s^r = \boldsymbol{R}_s \boldsymbol{i}_s^r + \omega \boldsymbol{J} \boldsymbol{\psi}_s^r + \frac{d}{dt} \boldsymbol{\psi}_s^r \tag{2.46}$$

$$u_f' = R_f' i_f' + \frac{d}{dt} \psi_f' \tag{2.47}$$

where the stator voltage, current, and flux linkages are given as

$$\boldsymbol{u}_s^r = \begin{bmatrix} u_d & u_q \end{bmatrix}^T \tag{2.48}$$

$$\boldsymbol{i}_s^r = \begin{bmatrix} i_d & i_q \end{bmatrix}^T \tag{2.49}$$

$$\boldsymbol{\psi}_s^r = \begin{bmatrix} \psi_d & \psi_q \end{bmatrix}^T \tag{2.50}$$

The flux linkage equation in the rotor reference frame is given as

$$\boldsymbol{\psi}_s^r = \boldsymbol{L}_s^r \boldsymbol{i}_s^r + \boldsymbol{M}_{df}^r i_f' \tag{2.51}$$

$$\psi_f' = L_f' \, i_f' + (\boldsymbol{M}_{df}^r)^T \boldsymbol{i}_s^r \tag{2.52}$$

where the inductance and mutual inductance matrices are given as

$$\boldsymbol{L}_s^r = \begin{bmatrix} L_{ls} + \frac{3}{2}(L_A + L_B) & 0 \\ 0 & L_{ls} + \frac{3}{2}(L_A - L_B) \end{bmatrix} \tag{2.53}$$

$$\boldsymbol{M}_{df}^r = M_{df} \begin{bmatrix} 1 \\ 0 \end{bmatrix} \tag{2.54}$$

Here, the magnetizing inductances on the d-axis and q-axis, L_d and L_q, are defined as

$$L_d = \frac{3}{2}(L_A + L_B) \tag{2.55}$$

$$L_q = \frac{3}{2}(L_A - L_B) \tag{2.56}$$

Since the leakage inductance is not involved in the electromagnetic energy conversion, it is not included in (2.55) and (2.56).

By the definition of d- and q-axis inductance, the inductance matrix in (2.53) becomes

$$\boldsymbol{L}_s^r = \begin{bmatrix} L_d & 0 \\ 0 & L_q \end{bmatrix} \tag{2.57}$$

In the rotor reference frame, the frame rotates synchronously with the rotor rotation. As a

result, the model becomes independent of the rotor position, which is the rotor speed multiplied by time. Therefore, the EESM model in the rotor reference frame is expressed as a time-invariant model. With the reference frame transformation, we can intuitively analyze the model behavior and design an estimator or a controller.

Based on the rotor reference model in (2.46) and (2.47), the equivalent circuit of EESM is depicted in Figure 2.4.

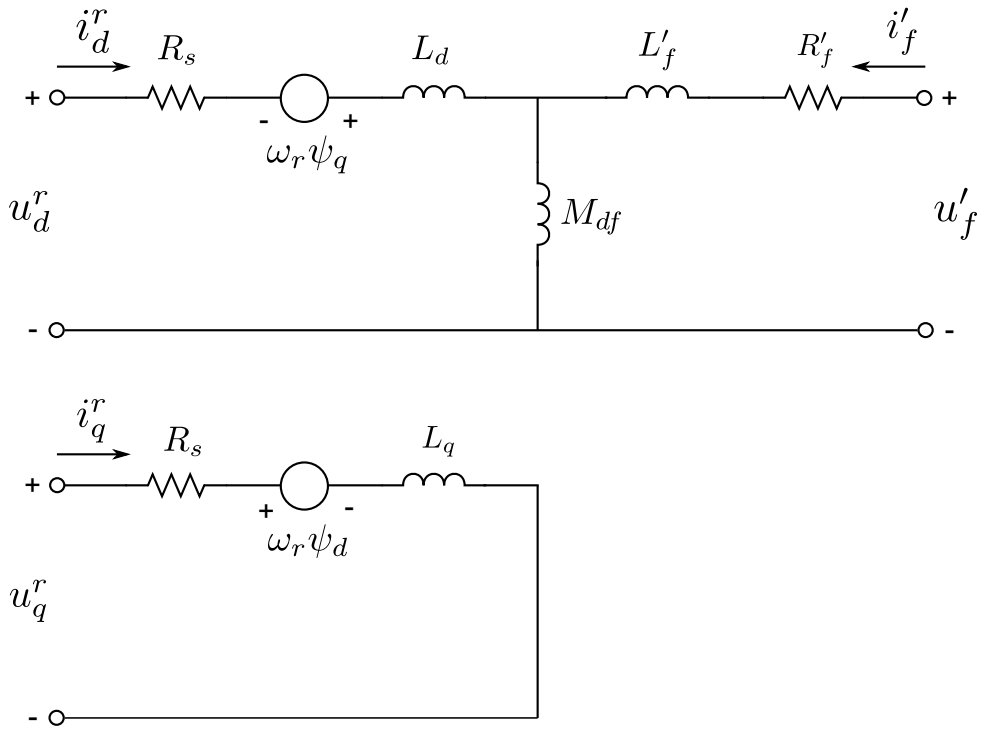

Figure 2.4: Equivalent circuit of EESM in the rotor reference frame

The torque equation of EESM is defined as a vector product of flux linkages and current. In the rotor reference frame, the torque equation is given as

$$\begin{aligned} T &= \frac{3}{2}\frac{P}{2}\left(\boldsymbol{\psi}_s^r \times \boldsymbol{i}_s^r\right) \\ &= \frac{3}{4}P\left(\psi_d i_q - \psi_q i_d\right) \\ &= \frac{3}{4}P\left(\left(L_d i_d + M_{df} i'_f\right) i_q - \left(L_q i_q\right) i_d\right) \\ &= \frac{3}{4}P(M_{df} i'_f i_q + \left(L_d - L_q\right) i_d i_q) \end{aligned} \tag{2.58}$$

where T and P represent the torque and the number of poles of EESM. In comparison with the torque equation of IPMSM, EESM has additional controllability in the model, i.e., the field cur-

rent. As a result, field weakening control for a wide-speed range can be achieved by controlling the field current of EESM. Besides, various optimal control methods have been researched with the controllability of the field current. Energy optimal controls, including the unity power factor control and copper loss minimization, were examined in [33–36]. Particularly, optimal control methods specialized in automotive traction applications have been widely researched [37–42].

Various EESM models have been suggested with finite element analysis (FEA) or analytic design models [43–45]. The models were designed to analyze and predict machine behavior under the saturation effect and cross-coupling effect.

2.3 Mutual Inductance

One of the characteristics of EESM is the existence of the mutual inductance between the stator winding and the rotor winding. As the rotor rotates, the geometric relationship between the rotor and the stator windings varies. Thus the mutual inductance changes with respect to the rotor position. Since the mutual inductance is one of the main parameters in this study, this section gives a detailed explanation regarding the mutual inductance of EESM.

2.3.1 Derivation of mutual inductance

Mutual induction is an electromagnetic induction phenomenon between a pair of adjacent coils. When a pair of coils are placed close to each other, the change of flux in one coil induces EMF in the other coil. As the magnetic flux generated by current in one coil passes through the inside of the other coil, the mutual induction occurs. Mutual inductance is defined as the relationship between the current and the magnetic flux and expressed with the geometric relationship of two coils and the magnetic permeability of the flux path.

A pair of concentric coils are depicted in Figure 2.5. The outer coil is a primary coil in which current flows, and the inner coil is a secondary coil in which the EMF is induced by the current in the primary coil. R_p, R_s, and θ_s represent the radius of the primary and the secondary coils, and the rotating angle of the secondary coil. The secondary coil rotates inside the primary coil. In the beginning of the derivation, the secondary coil is fixed to be aligned with the primary coil ($\theta_s = 0$). As current flows in the primary coil, the magnetic field is produced inside the coil. The magnetic field at the center of the coil can be computed by the Biot-Savart law, and it is

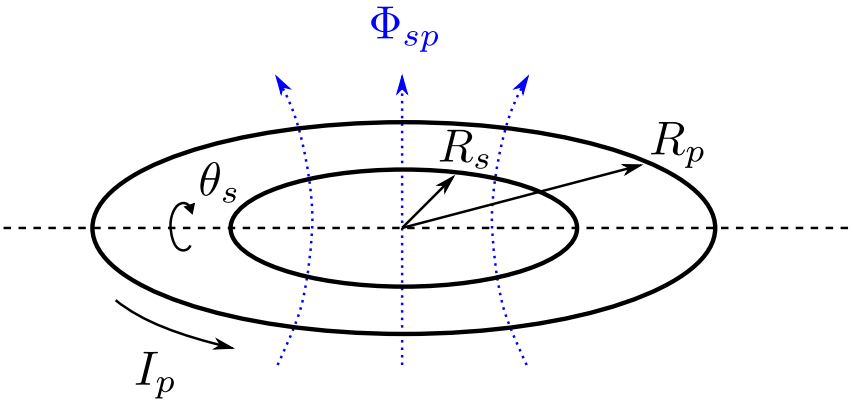

Figure 2.5: A pair of concentric coils

expressed as [46]

$$B_p = \frac{\mu_0 I_p}{2R_p} \tag{2.59}$$

where B_p, μ_0, and I_p represent the magnetic field of the primary coil, the magnetic permeability of air, and the current of the primary coil, respectively. By the magnetic field of the primary coil, magnetic flux passes through the inside of the secondary coil. The magnetic flux is expressed as

$$\Phi_{sp} = B_p A_s = \frac{\mu_0 I_p}{2R_p}\pi R_s^2 \tag{2.60}$$

where Φ_{sp} and A_s represent the magnetic flux inside the secondary coil by the primary coil and the area of the secondary coil. By the definition of mutual inductance, the mutual inductance between the primary and the secondary coils is expressed as

$$M_{sp} = \frac{\Phi_{sp}}{I_p} = \frac{\mu_0 \pi R_s^2}{2R_p} \tag{2.61}$$

(2.61) shows the mutual inductance while both coils are aligned. When the secondary coil rotates, the effective area of the secondary winding, $A_{s.eff.}$, is changed. By the geometry of both coils, the effective area is expressed as

$$A_{s.eff.} = A_s \cos\theta_s \tag{2.62}$$

Consequently, the mutual inductance with the rotating secondary coil can be expressed as

$$M_{sp} = \frac{\Phi_{sp}}{I_p} \cos\theta_s = \frac{\mu_0 \pi R_s^2}{2R_p} \cos\theta_s \tag{2.63}$$

As shown in (2.63), the mutual inductance in a pair of concentric coils is related to the geometric parameters of a coil and the magnetic permeability of the material in the flux path. Especially for the case of inner coil rotation, the mutual inductance is proportional to the cosine function of the rotating angle.

Mutual inductance between the stator and the rotor windings of EESM can be derived from the concentric coils example. The stator and the rotor windings correspond to the outer coil and the inner coil in Figure 2.5. The differences are: First, there are two outer coils, which are α- and β-axis windings, in EESM. Second, the numbers of turns in the stator winding and the field winding are given as N_s and N_f.

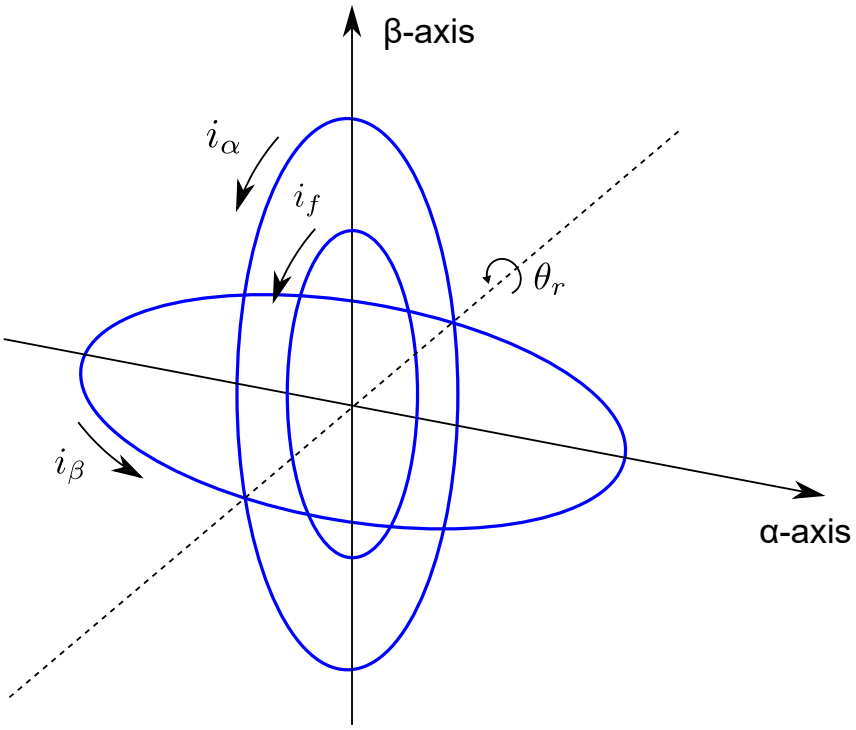

Figure 2.6: Stator and rotor windings in the stator reference frame ($\theta_r = 0$)

The stator and the rotor windings in the stator reference frame are depicted in Figure 2.6. The rotor winding is placed and rotates inside the stator winding. When the rotor angle is zero, the rotor winding faces the same direction as the α-axis stator winding. As a result, the change of the flux linkage in the α-axis stator winding induces the EMF in the rotor winding. However,

when the rotor angle is $\pi/2$ rad, the mutual induction between the α-axis stator winding and the rotor winding does not occur. This phenomenon appears with $\pi/2$ rad phase shift in between the β-axis stator winding and the rotor winding. Therefore, the mutually induced EMF in the rotor winding by the change of the stator winding flux linkage is expressed as

$$\begin{aligned} u'_{f.EMF} &= M_{sf}\left(\frac{d}{dt}\psi_\alpha \cos\theta_r + \frac{d}{dt}\psi_\beta \sin\theta_r\right) \\ &= M_{sf}\begin{bmatrix}\cos\theta_r & \sin\theta_r\end{bmatrix}\frac{d}{dt}\boldsymbol{\psi}_s^s \\ &= \boldsymbol{M}_{sf}^s \frac{d}{dt}\boldsymbol{\psi}_s^s \end{aligned} \tag{2.64}$$

where $u_{f.EMF}$ denotes the mutually induced EMF in the field winding. The mutual inductance matrix is expressed as

$$\boldsymbol{M}_{sf}^s = M_{sf}\begin{bmatrix}\cos\theta_r & \sin\theta_r\end{bmatrix} \tag{2.65}$$

The M_{sf}, the maximum value of the mutual inductance between the stator and the rotor windings, can be expressed as [30]

$$M_{sf} = KN_sN_f\frac{1}{g_{min}} \tag{2.66}$$

where K and g_{min} represent the proportional constant of the mutual inductance and the minimum length of the air gap. As shown in (2.64), the mutual induction components by the α- and β-windings are dependent on the rotor angle and have $\pi/2$ rad phase difference to each other. As a result of the two mutual induction components, the mutually induced field voltage is expressed as the sum of the two components. In practice, the mutual inductance is also affected by the winding types, i.e., concentrated or distributed winding. The winding function theory, which is presented in [47], can be applied to express the detailed behavior of the mutual induction.

2.3.2 Identification of mutual inductance

Inductance has nonlinear characteristics due to the magnetic saturation effect. Therefore, the inductance value varies depending on the operating point. Moreover, the mutual inductance of EESM varies with respect to the rotor position. As a result, direct measurement of the mutual inductance requires a complicated procedure. Therefore, the mutual inductance of EESM is

obtained by parameter identification in a steady-state operation condition in this study.

In the steady-state operation, the EESM model in the rotor reference frame shown in (2.46) and (2.47) is expressed as

$$\begin{aligned} U_d &= R_s I_d - \omega \Psi_q \\ &= R_s I_d - \omega L_q I_q \end{aligned} \tag{2.67}$$

$$\begin{aligned} U_q &= R_s I_q + \omega \Psi_d \\ &= R_s I_q + \omega \left(L_d I_d + M_{df} I'_f \right) \end{aligned} \tag{2.68}$$

$$U'_f = R'_f I'_f \tag{2.69}$$

In (2.68), the q-axis voltage equation is expressed with the mutual inductance term. By regulating the d- and q-axis current to be zero ($i_d = i_q = 0$), the q-axis voltage equation is simplified as

$$U_q = \omega M_{df} I'_f \tag{2.70}$$

By rearranging (2.70), the mutual inductance of EESM is expressed as

$$M_{df} = \frac{U_q}{\omega I'_f} \tag{2.71}$$

Since the variables on the right-hand side of (2.71) are measurable and computable, the mutual inductance can be identified in steady-state operation with (2.71). The measurement of variables has been performed under the following procedure: First, EESM is connected to a load machine, and the load machine rotates at a constant speed. Second, the field current is controlled to a certain current reference while d- and q-axis current are regulated to be zero. Third, during the steady-state operation condition, the computed q-axis reference voltage, the field current, and the machine speed are measured together. Fourth, the field current is increased stepwise, and variables are measured.

The identification results of the mutual inductance are presented in Figure 2.7. In the identification, the unscaled field current, i_f, has been used since the exact value of the scaled field current, i'_f, is related to the unmodeled winding effect, such as the effective number of turns of the field winding. Nevertheless, this identification is valid to evaluate the tendency of the mutual inductance variation.

In Figure 2.7, the result shows that the mutual inductance is inverse proportional to the mag-

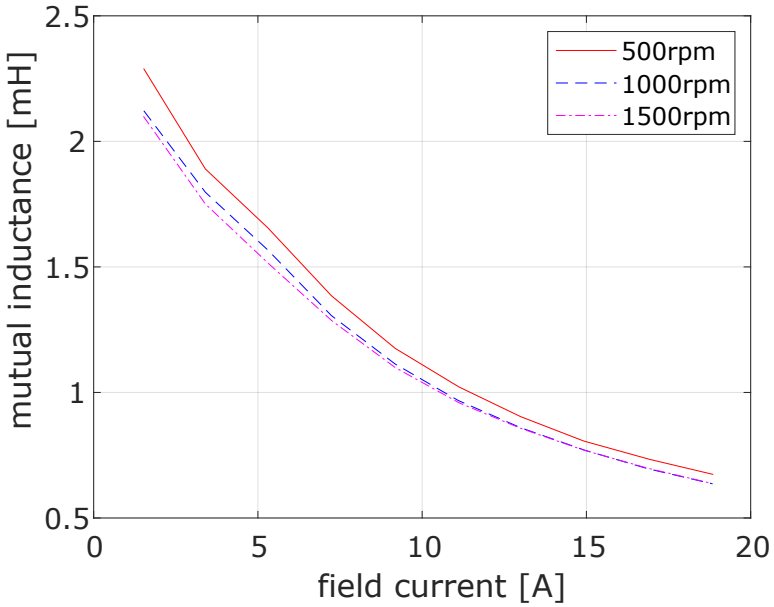

Figure 2.7: Identification of mutual inductance

nitude of the field current. It can be analyzed that as the field current is increased, the field winding material can be saturated. As a result, the mutual inductance is decreased in the field winding saturation condition. Therefore, the effect of mutual induction is expected to be less detectable in the saturation condition.

CHAPTER 3

State of the Art

Electric machine drive has achieved high precision and dynamic control performance due to the development of vector control. With the developments of power electronics and micro-controllers, vector control has made wide use of electric machines in various applications. The rotor position is essential in the vector control to decompose the current vector into flux and torque components. As a result, the vector control is highly dependent on a position sensor, and the dependency can reduce the reliability of the vector control. Besides, the position sensor of electric machines has installation, cost, and signal noise issues in practice. Therefore, sensorless control has been researched intensively for the last few decades [48, 49]. The main aims of the researches are: 1) Comparable control performance to the vector control with a position sensor, 2) Wide-speed range operation from a standstill to the high-speed range, and 3) Robustness to model uncertainty and inverter nonlinearity. Various approaches have been suggested to accomplish the aims, and they can be classified into a saliency-based method and a model-based method depending on the position estimation principle. The classification of sensorless control methods is depicted in Figure 3.1.

The saliency-based method utilizes the machine's anisotropic effects, such as magnetic saliency, stator saturation, slotting effect, and other mechanical anisotropies. Since the effect is not dominant in the fundamental signal, the saliency-based method requires an excitation signal to enlarge the anisotropic effects. According to the type of excitation signal, the saliency-based

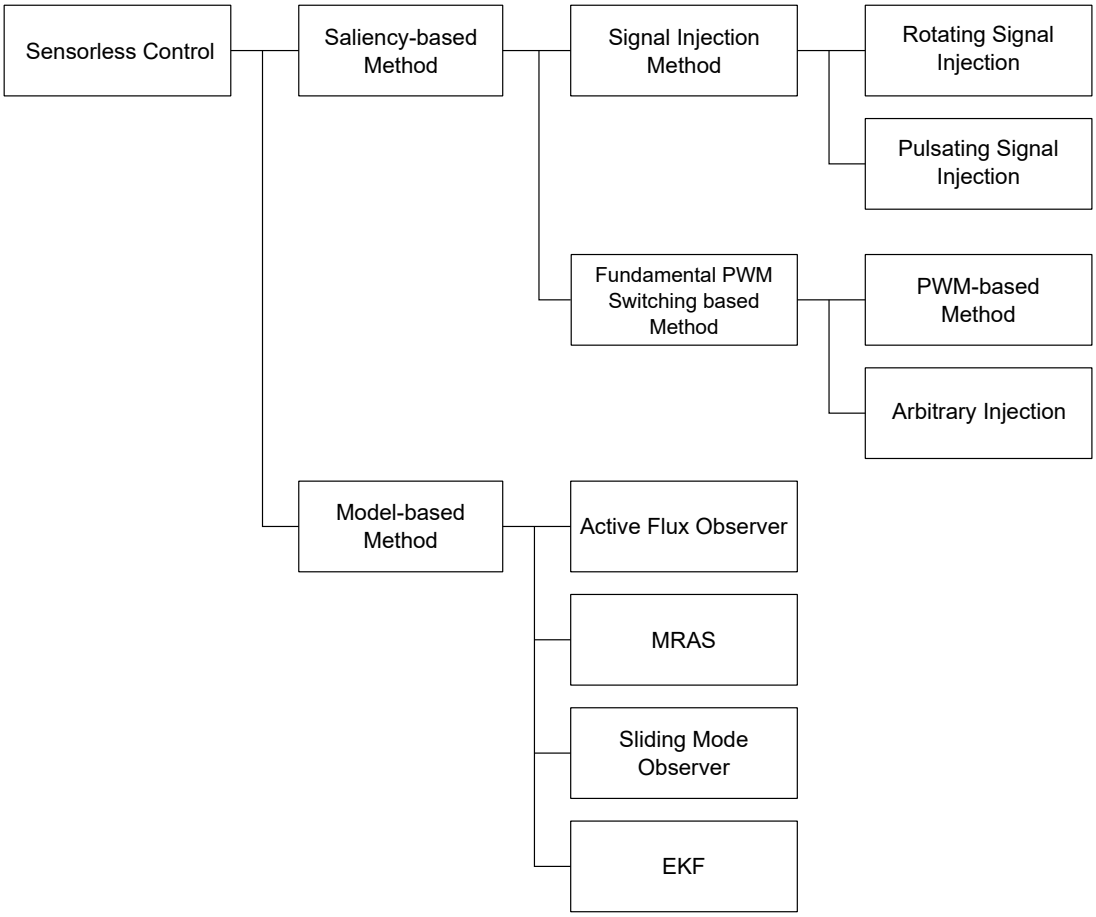

Figure 3.1: Classification of sensorless control methods

method can be classified into the signal injection method and the fundamental PWM switching-based method. The signal injection method injects an HF carrier signal over a fundamental drive signal and has been widely researched [50–53]. With the HF injection signal, the rotor position can be estimated in a standstill and low-speed range while the HF signal does not affect mechanical output. On the other hand, the fundamental switching-based method exploits the PWM switching signal as an excitation signal [27–29, 54, 55]. This method can reduce the side effects caused by the signal injection, such as audible noise, controller bandwidth limitation, and voltage margin reduction.

The model-based method employs a model of electric machines to estimate the rotor position. The model is based on the EMF, which is expressed as a function of the machine's rotation speed. Thanks to the introduction of the modern control theory, this method has enabled position estimation and showed good performance in the middle- and high-speed range. However, since the EMF is proportional to the rotation speed, the machine model loses its observability in standstill condition. Therefore, the combination of both methods has been researched for a

whole-speed range operation [56–58].

The type of electric machine is also a decisive factor in the design of the sensorless control. EESM is a synchronous machine and has field winding in the rotor to generate the field flux. The rotor winding provides an additional degree of freedom in the model compare to other types of synchronous machines. Hence there are more possibilities in the design of a sensorless control method of EESM. In this chapter, the state of the art of sensorless control of EESM is presented.

3.1 Saliency-based Method

3.1.1 High-frequency signal injection method

As shown in (2.42) and (2.43), the inductance matrix is expressed as a trigonometric function of the rotor position due to the salient pole structure of EESM. Based on the property, the rotor position can be estimated from the effect of the inductance variation. It is the main principle of the saliency-based sensorless control method. However, the inductance variation is affected by an operating point and appears with the fundamental signal. Consequently, the direct measurement of inductance from the fundamental model becomes complicated. Therefore, the HF signal injection method, which intensifies the saliency signal, has been proposed and developed with various approaches. In this method, the HF signal is injected into the fundamental signal, and the HF response is obtained by frequency demodulation. In the HF-model, the resistive voltage drop and the back EMF can be neglected. Thus the model is expressed as an inductive load. The HF-model can be expressed as

$$\begin{aligned} \boldsymbol{u}^s_{s.HF} &= \frac{d}{dt}\boldsymbol{\psi}^s_{s.HF} \\ &= \frac{d}{dt}\left(\boldsymbol{L}^s_s\, \boldsymbol{i}^s_{s.HF}\right) \end{aligned} \tag{3.1}$$

where the inductance matrix is given as

$$\boldsymbol{L}^s_s = \begin{bmatrix} L_A + L_B\cos 2\theta_r & L_B \sin 2\theta_r \\ L_B \sin 2\theta_r & L_A - L_B \cos 2\theta_r \end{bmatrix} \tag{3.2}$$

As shown in (3.2), the inductance matrix is a function of the rotor position. Therefore, the rotor position can be estimated based on the inductance variation in the HF response.

Rotating signal injection and pulsating signal injection are the most common types of the signal injection method. The rotating signal means that the injection signal vector rotates in the stator reference frame at the speed of ω_{HF}. Here, the rotating speed of the injection signal is much higher than the rotor speed $(\omega_{HF} \gg \omega_r)$. The pulsating signal means that the injection signal is applied on the estimated d- or q-axis, and its amplitude pulsates with the frequency of ω_{HF}. Figure 3.2 shows each injection signal and the corresponding response in EESM.

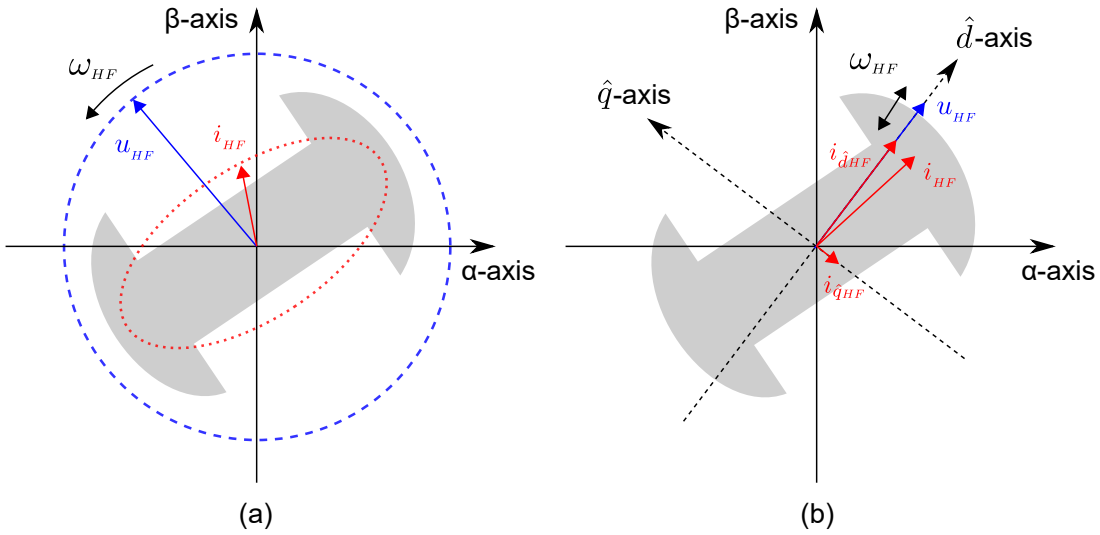

Figure 3.2: Concept of signal injection method: (a) rotating signal and (b) pulsating signal [59]

In Figure 3.2 (a), the outer circle represents the trajectory of the rotating voltage injection signal, and the inner ellipse depicts the trajectory of current response in the stator reference frame. Due to the machine saliency, the ellipse's major axis lies in the rotor flux direction. Therefore, the rotor position can be estimated by the induced HF current. In figure 3.2 (b), the injected voltage signal pulsates at the frequency of ω_{HF} along the estimated d-axis ($\hat{d}$-axis). If $\hat{d}$-axis is aligned with d-axis, the HF current response occurs only on the d-axis due to decoupling property between d- and q-axes. However, since the rotor position is unknown in sensorless control, the estimation error, $\tilde{\theta}_r$, may exist and cause the HF current response in the estimated q-axis as well. Since the HF response in the estimated q-axis contains the estimation error, the rotor position can be estimated by regulating the HF response to be zero. In both methods, frequency demodulation methods are required to obtain the HF response and extract the position-related information. In comparison with the two methods, it is found that the pulsating signal injection is more robust to different machine geometry and generates less

torque ripple under the same estimation error [60].

Both injection methods do not rely on back EMF, which is proportional to rotor speed, but on the magnetic saliency of machines. Therefore, the rotor position can be estimated in a low-speed range, including standstill condition. Since the frequency of the injection signal is much higher than the mechanical frequency range, the signal injection does not affect speed and torque control performance. However, it can increase acoustic noise and eddy current loss.

The HF-model of EESM is expressed differently from the HF-model of PMSM due to the existence of field winding, and it can be expressed as

$$\begin{aligned} \boldsymbol{u}^r_{s.HF} &= \frac{d}{dt}\boldsymbol{\psi}^r_{s.HF} \\ &= \frac{d}{dt}\left(\boldsymbol{L}^r_s\, \boldsymbol{i}^r_{s.HF} + \boldsymbol{M}^r_{df}\, i_{f.HF}\right) \qquad (3.3) \\ u_{f.HF} &= \frac{d}{dt}\psi_{f.HF} \\ &= \frac{d}{dt}(L_f\, i_{f.HF} + \left(\boldsymbol{M}^r_{df}\right)^T\, \boldsymbol{i}^r_{s.HF}) \qquad (3.4) \end{aligned}$$

The HF-model of EESM has a mutual inductance term between the stator and the rotor windings. Therefore, the response of the injected signal into the stator winding appears not only in the stator winding but also in the rotor winding. This phenomenon is also the same for the injection signal into the rotor winding. In other words, the rotor winding provides either an additional degree of controllability or observability of the machine. That means the HF signal can be injected into the rotor winding, or the HF signal response can be detected from the rotor winding. The conceptual block diagram of the sensorless control of EESM is illustrated in Figure 3.3.

Two general signal injection methods of EESM are illustrated in Figure 3.3. The block and arrow with red color represent the stator to rotor (S2R) method. In the S2R method, the HF signal is injected into the stator winding, and the rotor position is estimated from the HF response in the rotor winding. The signal injection into the stator winding can be applied as either the rotating signal or the pulsating signal. Thus, the HF signal also can be injected between the reference frame transformation block and the PWM block in Figure 3.3. The HF response is extracted from the field current, and the position estimation is performed with the HF field current in the S2R method.

On the contrary to the S2R method, the HF signal can be injected into the rotor winding and its response can be obtained from the stator winding. This method is referred to as the rotor to

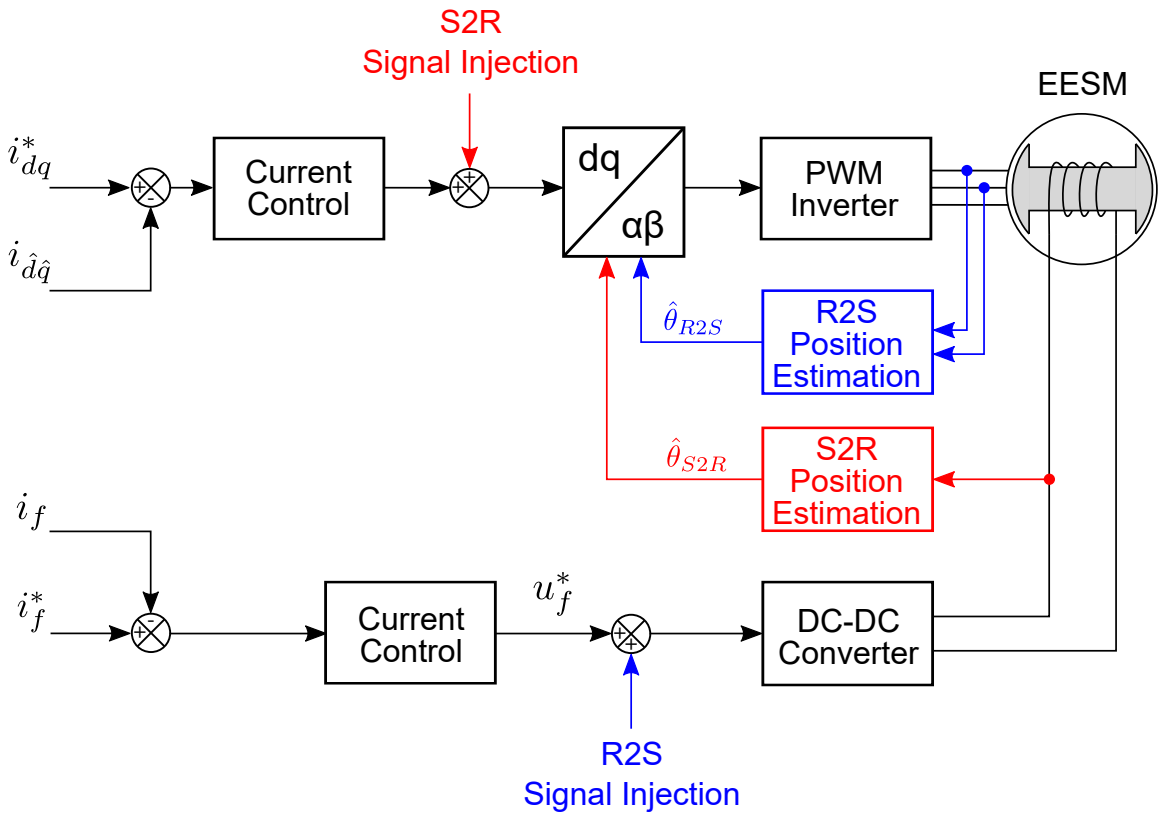

Figure 3.3: Concept of HF signal injection methods of EESM

stator (R2S) method in this study. The R2S method is depicted with blue color in Figure 3.3. The HF signal is injected to the rotor winding with the concept of amplitude modulation. The corresponding response in the stator winding is used in the R2S method.

3.1.1.1 Stator to Rotor (S2R) method

To explain the estimation principle of the S2R method, (3.3) is modified to analyze the relationship between stator voltage and rotor current as

$$\boldsymbol{u}^r_{s.HF} = \boldsymbol{M}^r_{df} \frac{d}{dt} i_{f.HF} \tag{3.5}$$

$$\begin{bmatrix} u_{d.HF} \\ u_{q.HF} \end{bmatrix} = \begin{bmatrix} M_{df} \\ 0 \end{bmatrix} \frac{d}{dt} i_{f.HF} \tag{3.6}$$

(3.6) shows that the rotor current is coupled to the d-axis voltage but decoupled to the q-axis voltage. In the same manner with the pulsating signal injection of PMSM, a pulsating signal

is injected into the estimated q-axis. If the rotor position is estimated correctly, the signal injection into the estimated q-axis does not induce HF current response in the rotor winding. However, if the estimation has an error, the HF current response appears in the rotor winding. The phenomenon can be expressed with the concept of the misaligned frame presented in [61]. According to the concept, the estimated dq-frame is expressed simply with the rotation matrix of the position estimation error. The misaligned frame is expressed as

$$\begin{bmatrix} f_{\hat{d}} \\ f_{\hat{q}} \end{bmatrix} = \boldsymbol{R}\left(\tilde{\theta}_r\right) \begin{bmatrix} f_d \\ f_q \end{bmatrix} = \begin{bmatrix} \cos\tilde{\theta}_r & \sin\tilde{\theta}_r \\ -\sin\tilde{\theta}_r & \cos\tilde{\theta}_r \end{bmatrix} \begin{bmatrix} f_d \\ f_q \end{bmatrix} \tag{3.7}$$

where the estimation error, $\tilde{\theta}_r$, is defined as

$$\tilde{\theta}_r = \hat{\theta}_r - \theta_r \tag{3.8}$$

The HF voltage equation in the estimated dq-frame is expressed as

$$\begin{aligned} \begin{bmatrix} u_{\hat{d}} \\ u_{\hat{q}} \end{bmatrix} &= \boldsymbol{R}\left(\tilde{\theta}_r\right) \begin{bmatrix} u_d \\ u_q \end{bmatrix} \\ &= \boldsymbol{R}\left(\tilde{\theta}_r\right) \begin{bmatrix} M_{df} \\ 0 \end{bmatrix} \frac{d}{dt} i_f \\ &= \begin{bmatrix} \cos\tilde{\theta}_r & \sin\tilde{\theta}_r \\ -\sin\tilde{\theta}_r & \cos\tilde{\theta}_r \end{bmatrix} \begin{bmatrix} M_{df} \\ 0 \end{bmatrix} \frac{d}{dt} i_f \\ &= \begin{bmatrix} M_{df}\cos\tilde{\theta}_r \\ -M_{df}\sin\tilde{\theta}_r \end{bmatrix} \frac{d}{dt} i_f \end{aligned} \tag{3.9}$$

where the mutual inductance matrix in the estimated dq-frame is defined as

$$\boldsymbol{M}_{\hat{d}f} = \begin{bmatrix} M_{df}\cos\tilde{\theta}_r \\ -M_{df}\sin\tilde{\theta}_r \end{bmatrix} \tag{3.10}$$

The left pseudoinverse of the mutual inductance matrix in the estimated dq-frame in (3.10) is defined as

$$\begin{aligned}\boldsymbol{I} &= \boldsymbol{M}_{\hat{d}f}^{+}\boldsymbol{M}_{\hat{d}f} \\ &= \boldsymbol{M}_{\hat{d}f}^{+}\begin{bmatrix} M_{df}\cos\tilde{\theta}_r \\ -M_{df}\sin\tilde{\theta}_r \end{bmatrix}\end{aligned} \tag{3.11}$$

By the definition in (3.11), the left pseudoinverse of the mutual inductance matrix in the estimated dq-frame is obtained as

$$\boldsymbol{M}_{\hat{d}f}^{+} = \frac{1}{M_{df}}\begin{bmatrix}\cos\tilde{\theta}_r & -\sin\tilde{\theta}_r\end{bmatrix} \tag{3.12}$$

To make $\frac{d}{dt}i_f$ subject of the equation in (3.9), the pseudoinverse matrix is multiplied to the equation in (3.9) as

$$\boldsymbol{M}_{\hat{d}f}\frac{d}{dt}i_f = \begin{bmatrix} u_{\hat{d}} \\ u_{\hat{q}} \end{bmatrix} \tag{3.13}$$

$$\boldsymbol{M}_{\hat{d}f}^{+}\boldsymbol{M}_{\hat{d}f}\frac{d}{dt}i_f = \boldsymbol{M}_{\hat{d}f}^{+}\begin{bmatrix} u_{\hat{d}} \\ u_{\hat{q}} \end{bmatrix} \tag{3.14}$$

$$\frac{d}{dt}i_f = \boldsymbol{M}_{\hat{d}f}^{+}\begin{bmatrix} u_{\hat{d}} \\ u_{\hat{q}} \end{bmatrix} \tag{3.15}$$

Therefore, the HF rotor current response in the estimated dq-frame is rewritten as

$$\begin{aligned}\frac{d}{dt}i_f &= \frac{1}{M_{df}}\begin{bmatrix}\cos\tilde{\theta}_r & -\sin\tilde{\theta}_r\end{bmatrix}\begin{bmatrix} u_{\hat{d}} \\ u_{\hat{q}} \end{bmatrix} \\ &= \frac{1}{M_{df}}\left(\cos\tilde{\theta}_r u_{\hat{d}} - \sin\tilde{\theta}_r u_{\hat{q}}\right)\end{aligned} \tag{3.16}$$

Suppose that the injected HF signal into the estimated q-axis is given as

$$u_{\hat{q}.HF} = U_{HF}\sin\left(\omega_{HF}t\right) \tag{3.17}$$

By the injection signal, the rotor current response is expressed as

$$\begin{aligned}\frac{d}{dt}i_f &= \frac{1}{M_{df}}\begin{bmatrix}\cos\tilde{\theta}_r & -\sin\tilde{\theta}_r\end{bmatrix}\begin{bmatrix}0\\ u_{\hat{q}.HF}\end{bmatrix}\\ &= -\frac{1}{M_{df}}\sin\tilde{\theta}_r u_{\hat{q}.HF}\\ &= -\frac{U_{HF}}{M_{df}}\sin\tilde{\theta}_r\sin\left(\omega_{HF}t\right)\end{aligned} \tag{3.18}$$

(3.18) indicates that the amplitude of the rotor current response is proportional to the estimation error under the assumption of the estimation error is small $(\sin\tilde{\theta}_r \approx \tilde{\theta}_r)$. Therefore, by minimizing the HF current response with a tracking observer, the rotor position can be estimated correctly.

In [62], the S2R method was proposed with the rotating and the pulsating signal injection. As a frequency demodulation method, the Goertzel algorithm was used to obtain the HF response, and pre-identified model parameters were stored in a lookup table (LUT) to compensate for the cross-coupling inductance. Both methods showed different error dynamics but could estimate the rotor position within a certain level of error.

3.1.1.2 Rotor to Stator (R2S) method

The R2S method employs the HF-model between the rotor voltage and the stator current. By separating the rotor current term from (3.4), the equation is rewritten as

$$\begin{aligned}u_{f.HF} &= \left(\boldsymbol{M}_{df}^{r}\right)^{T}\frac{d}{dt}\boldsymbol{i}_{s.HF}^{r}\\ &= \begin{bmatrix}M_{df} & 0\end{bmatrix}\frac{d}{dt}\begin{bmatrix}i_d\\ i_q\end{bmatrix}\end{aligned} \tag{3.19}$$

In the estimated rotor reference frame, the stator current can be expressed as

$$\frac{d}{dt}\begin{bmatrix}i_d\\ i_q\end{bmatrix} = \boldsymbol{R}^{-1}\left(\tilde{\theta}_r\right)\frac{d}{dt}\begin{bmatrix}i_{\hat{d}}\\ i_{\hat{q}}\end{bmatrix} \tag{3.20}$$

Therefore, the HF-model in the estimated rotor reference frame is given as

$$
\begin{aligned}
u_{f.HF} &= \begin{bmatrix} M_{df} & 0 \end{bmatrix} \boldsymbol{R}^{-1}\left(\tilde{\theta}_r\right) \frac{d}{dt} \begin{bmatrix} i_{\hat{d}} \\ i_{\hat{q}} \end{bmatrix} \\
&= \begin{bmatrix} M_{df} & 0 \end{bmatrix} \begin{bmatrix} \cos\tilde{\theta}_r & -\sin\tilde{\theta}_r \\ \sin\tilde{\theta}_r & \cos\tilde{\theta}_r \end{bmatrix} \frac{d}{dt} \begin{bmatrix} i_{\hat{d}} \\ i_{\hat{q}} \end{bmatrix} \\
&= \begin{bmatrix} M_{df}\cos\tilde{\theta}_r & -M_{df}\sin\tilde{\theta}_r \end{bmatrix} \frac{d}{dt} \begin{bmatrix} i_{\hat{d}} \\ i_{\hat{q}} \end{bmatrix} \\
&= M_{df}\cos\tilde{\theta}_r \frac{d}{dt} i_{\hat{d}} - M_{df}\sin\tilde{\theta}_r \frac{d}{dt} i_{\hat{q}}
\end{aligned} \tag{3.21}
$$

As shown in (3.21), the HF injection signal into the rotor winding yields the current response in the stator winding. The response is related to the position estimation error. The estimated q-axis current response appears as the estimation error occurs. Therefore, the position estimation can be achieved by minimizing the current response in the estimated q-axis.

R2S method has been researched in several papers due to the accessibility of signal injection in the rotor winding and the availability of the fundamental switching component as an injection signal [21, 22, 63, 64]. In [21], the HF current signal is injected into the rotor winding. Self- and mutual-inductance parameters are calculated with a finite element method (FEM) and compensated in the estimation algorithm. As a different approach, [22] utilizes the fundamental rotor PWM switching voltage as an injection signal. The square wave of the switching voltage is considered as an AC signal by a Fourier transform. That is, the first harmonic of the square wave is taken as the injection signal. With the compensation of parameters in a LUT, the method estimates the rotor position in the low-speed range. This method estimates the rotor position without injecting any signal. Another R2S method without injecting signal was proposed in [23]. In this method, rotor current ripple by PWM switching is utilized as an injection signal. The induced stator voltage by the rotor current ripple is calculated by a DO and used in the position estimation method.

The structure of EESM is similar to a resolver. A resolver is a position sensor with rugged and reliable rotor position sensing performance [65]. Both EESM and a resolver have a structure like a rotating transformer. As the reluctance varies with respect to the rotor position, the rotor position of EESM can be estimated in the same manner as a resolver. However, estimation error can be increased depending on the operation condition of EESM. There are differences between

a resolver and an EESM, e.g., the excitation signal is not sinusoidal, and the inductance of the stator winding varies. Therefore, those differences should be considered to apply the position calculation method of a resolver to EESM. The application of the position estimation method motivated by a resolver is presented in section 4.1.

General signal injection methods of PMSM inject the excitation signal into the stator and detect the saliency signal from the stator. The method can be referred to as the stator to stator (S2S) method. The S2S method was utilized for the sensorless control of EESM in [66]. The experiments verified the estimation performance in the low-speed range, while the estimation failed in the high-speed range. In [67], it was claimed that the field winding acts like a damper winding for HF signal in the S2S method. Thus the sensorless control performance differs from the one in PMSM. As a different approach, it is also possible to inject the HF signal into the rotor winding and to detect the response in the rotor winding. However, it is known that the estimation requires a complex algorithm since the stator slotting effect saturates very quickly [67].

In the previous saliency-based sensorless control methods of EESM, various methods have been suggested and investigated by using the rotor winding. The S2R and R2S methods are unique approaches to the saliency-based method. In the estimation algorithm, the mutual inductance between the stator and the rotor windings is crucial. The previous methods have shown satisfactory estimation results in the low-speed range, but the estimation in the middle- and high-speed range has not been validated.

3.1.2 PWM-based method

The PWM-based method is a saliency-based method that utilizes the PWM switching signal as an excitation signal. As the excitation signal frequency becomes as high as the PWM frequency, the bandwidth of current control and position control can be increased. Moreover, an additional signal injection may not be required in the high-speed range with the method. The PWM-based method can be divided into a PWM frequency signal injection method and a fundamental PWM switching-based method. The PWM frequency signal injection method injects the PWM frequency excitation signal continuously, and the fundamental PWM switching-based method applies the signal injection conditionally for the case that the magnitude of the response signal is insufficient. The PWM-based method has been proposed for a PMSM and a reluctance machine in [27–29]. Although the method has not been applied to EESM, this subsection presents the method since it is adopted to the proposed method.

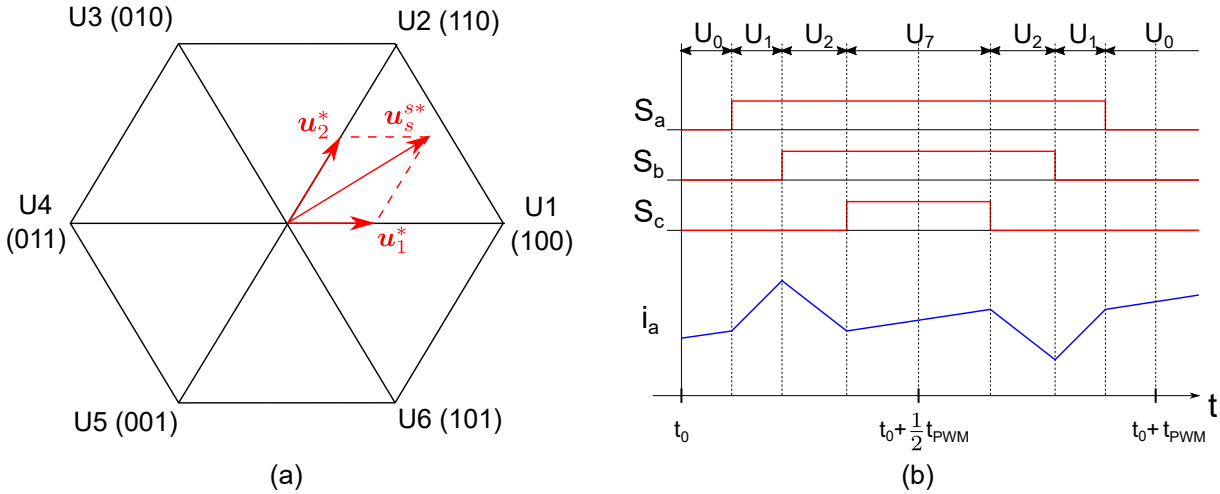

Figure 3.4: Stator reference voltage with current response: (a) SVM diagram and (b) switching states with current response

To explain the basic concept of the method, stator reference voltage in space vector modulation (SVM) and corresponding current response are shown in Figure 3.4. There are eight voltage vectors in the SVM diagram with a combination of three-phase on/off-states. In Figure 3.4 (a), U1 $\sim$ U6 represent six active voltage vectors, and the zero voltage vectors, U0 and U7, are not depicted. The three binary numbers indicate the on/off-state of abc-phase, e.g., '100' means that the a-phase high-side switch is in the on-state and the b- and c-phase high-side switches are in the off-state. Naturally, low-side switches are in a complementary state to the three binary numbers. In the diagram, the reference voltage vector, $\boldsymbol{u}_s^{s*}$, is applied as a vector sum of two adjacent active voltage vectors (u_1^* and u_2^*) and zero voltage vectors (u_0^* and u_7^*). The lower case u represents the scaled active voltage vector and is expressed as

$$u_n = \frac{t_n}{t_{PWM}} U_n \tag{3.22}$$

where n is 0, 1, 2, and 7. The applying time of the active and zero voltage vectors are defined as

$$\frac{1}{2} t_{PWM} = \frac{1}{2} t_0 + t_1 + t_2 + \frac{1}{2} t_7 \tag{3.23}$$

$$t_0 = t_7 \tag{3.24}$$

Given the reference active voltage vector, the actual switching signal is generated as Fig-

ure 3.4 (b). In Figure 3.4 (b), Sx (x=a, b, or c) represents the switching state of the phase. In SVM, the switching states are symmetric about the half PWM cycle, $\frac{1}{2}t_{PWM}$. That is, the active voltage vectors are applied twice per PWM cycle. The average current slope for a PWM period shows a fundamental current signal slope. When zero voltage vector is applied, the current response shows the effect of the back EMF. During the active time for u_1^* and u_2^*, a corresponding transient response appears in the current signal, as shown in Figure 3.4 (b). Like the HF current response in the signal injection method, the transient current response of the active voltage vector reflects the saliency of the machine. Therefore, the rotor position can be estimated in the same manner as the signal injection method.

Kim et al. proposed the PWM frequency signal injection method for IPMSM [29]. In the proposed method, the frequency of the injection signal is the same as the PWM frequency, and both concepts of the rotating and the pulsating signal injection have been applied. The PWM frequency pulsating signal injection and the corresponding current response are illustrated in Figure 3.5.

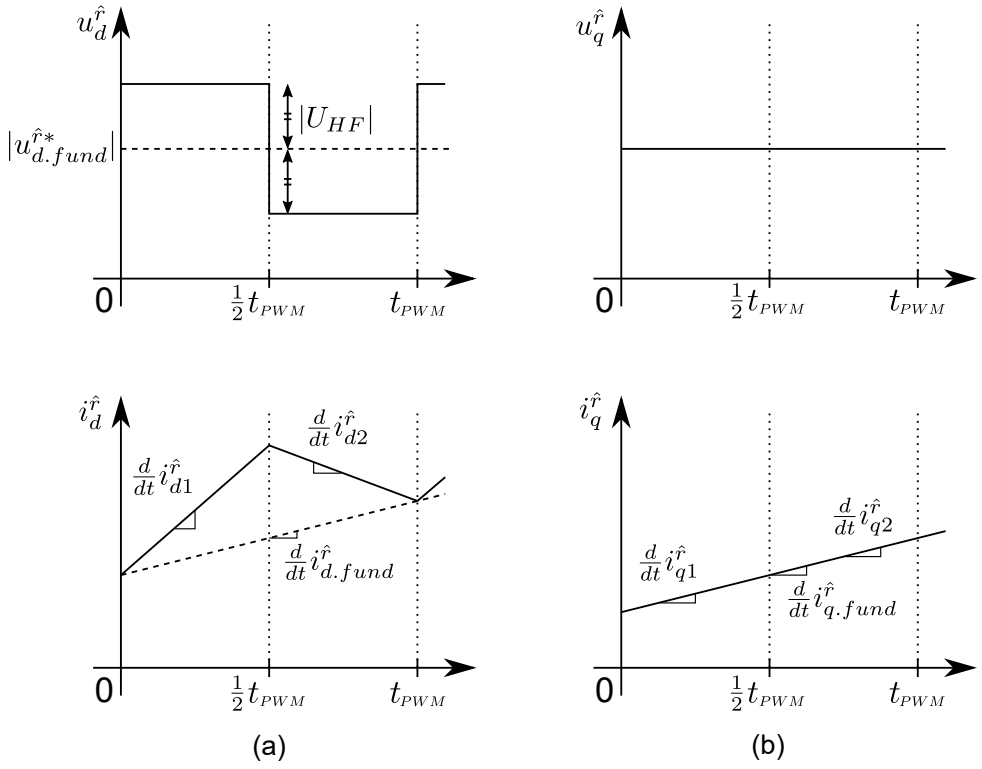

Figure 3.5: Stator reference voltage and stator current: (a) signal injection in the estimated d-axis and (b) no signal injection in the estimated q-axis

Figure 3.5 shows the stator reference voltage and the stator current in the estimated rotor reference frame under the assumption that the estimation is correct. In Figure 3.5, the solid

line represents the actual voltage with the injection signal and corresponding current response, and the dashed line represents the fundamental voltage and corresponding current signal. The pulsating signal is injected into the estimated d-axis, as shown in Figure 3.5 (a). The injection signal is expressed as

$$\boldsymbol{u}_{s.HF}^{r} = \begin{cases} U_{HF} \begin{bmatrix} 1 \\ 0 \end{bmatrix}, & \text{if } 0 < t \leq \frac{1}{2} t_{PWM} \\ -U_{HF} \begin{bmatrix} 1 \\ 0 \end{bmatrix}, & \text{if } \frac{1}{2} t_{PWM} < t \leq t_{PWM} \end{cases} \tag{3.25}$$

In the estimated rotor reference frame, the pulsating signal is expressed as

$$\boldsymbol{u}_{s.HF}^{\hat{r}} = \boldsymbol{R}\left(\tilde{\theta}_r\right) \boldsymbol{u}_{s.HF}^{r} = \pm U_{HF} \begin{bmatrix} \cos\tilde{\theta}_r \\ -\sin\tilde{\theta}_r \end{bmatrix} \tag{3.26}$$

As the pulsating signal is injected into the estimated d-axis, the current slope is changed from the fundamental current slope shown in Figure 3.5 (a). The current slope in the estimated q-axis is also changed as the estimation error occurs. Since the frequency of the injection signal is as high as the PWM frequency, the HF-model of IPMSM can be used to derive the current response. The current slope can be expressed as

$$\begin{aligned} \frac{d}{dt} \boldsymbol{i}_{s.HF}^{r} &= \left(\boldsymbol{L}_s^{r}\right)^{-1} \boldsymbol{u}_{s.HF}^{r} \\ &= \begin{bmatrix} \frac{1}{L_d} & 0 \\ 0 & \frac{1}{L_q} \end{bmatrix} \begin{bmatrix} \pm U_{HF} \\ 0 \end{bmatrix} \end{aligned} \tag{3.27}$$

Given the PWM frequency pulsating signal in (3.26), the current response in the estimated rotor

reference frame is expressed as

$$\begin{aligned}
\frac{d}{dt}\boldsymbol{i}_{s.HF}^{\hat{r}} &= \boldsymbol{R}\left(\tilde{\theta}_r\right)\left(\boldsymbol{L}_s^r\right)^{-1}\boldsymbol{u}_{s.HF}^{\hat{r}} \\
&= \pm U_{HF}\begin{bmatrix}\cos\tilde{\theta}_r & \sin\tilde{\theta}_r \\ -\sin\tilde{\theta}_r & \cos\tilde{\theta}_r\end{bmatrix}\begin{bmatrix}\frac{1}{L_d} & 0 \\ 0 & \frac{1}{L_q}\end{bmatrix}\begin{bmatrix}\cos\tilde{\theta}_r \\ -\sin\tilde{\theta}_r\end{bmatrix} \\
&= \pm U_{HF}\begin{bmatrix}\frac{\cos^2\tilde{\theta}_r}{L_d} - \frac{\sin^2\tilde{\theta}_r}{L_q} \\ -\left(\frac{1}{L_d}+\frac{1}{L_q}\right)\cos\tilde{\theta}_r\sin\tilde{\theta}_r\end{bmatrix} \\
&= \pm U_{HF}\begin{bmatrix}\frac{\cos^2\tilde{\theta}_r}{L_d} - \frac{\sin^2\tilde{\theta}_r}{L_q} \\ -\frac{1}{2}\left(\frac{1}{L_d}+\frac{1}{L_q}\right)\sin 2\tilde{\theta}_r\end{bmatrix}
\end{aligned} \tag{3.28}$$

As shown in (3.28), the current slope is proportional to the magnitude of the injected signal and depends on the position estimation error. Especially for the estimated q-axis current, the current derivative is proportional to the estimation error when the error is small enough for the assumption of $2\tilde{\theta}_r \approx \sin 2\tilde{\theta}_r$. With the same manner of the general pulsating signal injection method, the rotor position can be estimated by minimizing the current slope in the estimated q-axis.

The current slope in the estimated q-axis during a half PWM cycle can be expressed as

$$\frac{d}{dt}i_{q1}^{\hat{r}} = \frac{d}{dt}i_{q.fund}^{\hat{r}} + U_{HF}\left(-\frac{1}{2}\left(\frac{1}{L_d}+\frac{1}{L_q}\right)\sin 2\tilde{\theta}_r\right) \tag{3.29}$$

$$\frac{d}{dt}i_{q2}^{\hat{r}} = \frac{d}{dt}i_{q.fund}^{\hat{r}} - U_{HF}\left(-\frac{1}{2}\left(\frac{1}{L_d}+\frac{1}{L_q}\right)\sin 2\tilde{\theta}_r\right) \tag{3.30}$$

Subtracting the current derivative in the first and the second half PWM cycle yields

$$\frac{d}{dt}i_{q2}^{\hat{r}} - \frac{d}{dt}i_{q1}^{\hat{r}} = U_{HF}\left(\frac{1}{L_d}+\frac{1}{L_q}\right)\sin 2\tilde{\theta}_r \tag{3.31}$$

Consequently, the position estimation error can be obtained as

$$\sin 2\tilde{\theta}_r = K\left(\frac{d}{dt}i_{q2}^{\hat{r}} - \frac{d}{dt}i_{q1}^{\hat{r}}\right) \tag{3.32}$$

where the K is given as

$$K = \frac{1}{U_{HF}\left(\frac{1}{L_d} + \frac{1}{L_q}\right)} \tag{3.33}$$

While the general signal injection method requires a complex frequency demodulation method, the HF current response can be extracted by simple arithmetic operations in the PWM-based method. For example, the current derivative in (3.32) can be calculated as

$$\frac{d}{dt} i_{q1}^{\hat{r}} = \frac{\Delta i_{q1}^{\hat{r}}}{\Delta t} = \frac{i_{q.t_{\frac{1}{2}PWM}}^{\hat{r}} - i_{q.t_0}^{\hat{r}}}{\frac{1}{2}t_{PWM} - t_0} \tag{3.34}$$

$$\frac{d}{dt} i_{q2}^{\hat{r}} = \frac{\Delta i_{q2}^{\hat{r}}}{\Delta t} = \frac{i_{q.t_{PWM}}^{\hat{r}} - i_{q.t_{\frac{1}{2}PWM}}^{\hat{r}}}{t_{PWM} - \frac{1}{2}t_{PWM}} \tag{3.35}$$

where $i_{q.t_n}^{\hat{r}}$ represents the estimated q-axis current at the time t_n in Figure 3.5.

Moreover, the subtraction operation of the two current slopes corresponds to the frequency demodulation method in the signal injection method. Therefore, the fundamental frequency components can be removed by a simple operation.

As another PWM-based method, fundamental PWM switching is exploited to estimate position without injecting additional signal continuously [27, 28]. Paulus et al. proposed the arbitrary injection method in [28]. Regardless of the type of excitation signal, the current ripple by additional injection signal or fundamental PWM signal can be utilized to estimate the rotor position in the proposed method. The only requirement for the method is the presence of current derivative by active voltage vector. The transient current response by active voltage vector is extracted analogously to the PWM-based method, and the saliency in the current response is used in position estimation. Since the magnitude of the active voltage vector is sufficient in the middle- and high-speed range, the position can be estimated without the signal injection. However, signal injection is required to amplify the HF current response in the low-speed range. Unlike general signal injection methods that employ a specific type of injection signal, this method can utilize the arbitrary injection signal. This is because the signal injection aims only to obtain the detectable magnitude of the current derivative. The experimental results showed satisfactory control performance from a standstill to the rated speed thanks to the wide bandwidth of the method.

Compared with the general signal injection method, the PWM-based method has achieved the wide-speed operation range with a simple calculation. Also, side effects of the signal injection method such as audible noise, voltage margin reduction can be reduced. To detect the current

change within a PWM period, high-speed current sampling and high bandwidth current sensors are necessary.

3.2 Model-based Method

The model-based method estimates the rotor position with a fundamental model of EESM. Given the reference voltage and measured current, the model calculates the EMF of the machine. Since the EMF is proportional to the rotor speed, the rotor position and speed can be estimated by EMF estimation. For speed and position estimation, a phase-locked loop (PLL) or a Luenberger type observer is used in general. This method shows good estimation results in the middle- and high-speed range. However, the whole speed range sensorless control is not guaranteed, and the estimation can be inaccurate due to the reasons below:

1. The EMF diminishes to zero as the rotor speed becomes zero since the EMF is proportional to the rotor speed.
2. The parameter values vary depending on the operation condition. Therefore the model may result in inaccurate position estimation.
3. The integration process in the position estimation algorithm is vulnerable to offset error.
4. The reference voltage differs from the actual applied voltage due to inverter nonlinearities such as deadtime and voltage drop of switching devices.

The above effects are dominant in the voltage equation for the low-speed range, where the induced EMF is insufficient. Therefore, the performance in the range is not suitable for the model-based method. To improve the method in the low-speed range, modern control theory and parameter identification methods have been suggested. In this section, model-based methods of EESM are introduced and discussed.

3.2.1 Active flux observer

The concept of the active flux vector for EESM has been proposed in [26]. The active flux vector is defined as the torque-producing flux in the torque equation. The active flux is expressed as

$$\boldsymbol{\psi}_{af}^{r} = M_{df} i_f + (L_d - L_q)\, i_d \tag{3.36}$$

where $\boldsymbol{\psi}_{af}^{r}$ represents the active flux of EESM in the rotor reference frame. The active flux vector is defined to be aligned with the rotor angle. Given the active flux vector, the torque equation is expressed as

$$T = \frac{3}{2}\frac{P}{2}\boldsymbol{\psi}_{af}^{r} i_q \tag{3.37}$$

As shown in (3.37), the salient pole EESM can be modeled as an equivalent non-salient model with the active flux vector. As a result, the estimation model becomes more straightforward than the salient machine model [68].

In comparison with the flux linkage equation in (2.51), the relationship between the stator flux linkage and the active flux linkage is given as

$$\boldsymbol{\psi}_{af}^{r} = \boldsymbol{\psi}_{s}^{r} - L_q \boldsymbol{i}_{s}^{r} \tag{3.38}$$

The stator flux linkage is estimated by combining the voltage-flux model and the current-flux model. The two models are expressed as

$$\boldsymbol{\psi}_{s}^{s} = \int \left(\boldsymbol{u}_{s}^{s} - R_s \boldsymbol{i}_{s}^{s} + \boldsymbol{u}_{comp}^{s} \right) dt \tag{3.39}$$

$$\boldsymbol{\psi}_{s}^{r} = \begin{bmatrix} L_d & 0 \\ 0 & L_q \end{bmatrix} \boldsymbol{i}_{s}^{r} + \begin{bmatrix} M_{df} \\ 0 \end{bmatrix} i_f \tag{3.40}$$

where $\boldsymbol{u}_{comp}^{s}$ represents a total compensator vector, which compensates integral offset, initial rotor position error, parameter variations, and inverter nonlinearities. (3.39) and (3.40) represent the voltage-flux model and the current-flux model. The block diagram of the active flux observer (AFO) is depicted in Figure 3.6.

In Figure 3.6, the current-flux model and the voltage-flux model are illustrated in the red and blue boxes. The current-flux model in the (3.40) is an open-loop model in the estimated rotor reference frame and works dominantly at a low-speed range. The estimation result depends on the q-axis inductance, which varies notably as the magnitude of stator current increases. Therefore, the current-flux saturation model is used to compensate for the q-axis inductance variation. The voltage-flux model in (3.39) composes a closed-loop in the stator reference frame with the PI compensator. The PI compensator yields the total compensator vector from the difference between the voltage-flux model and the current-flux model. The voltage-flux model is dominant at the middle- and high-speed range. By combining both models, the estimation

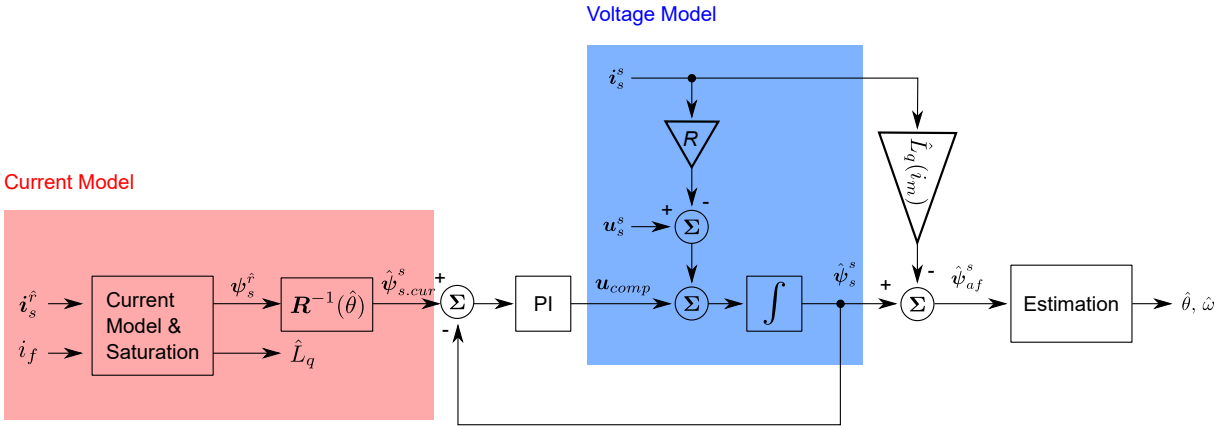

Figure 3.6: Block diagram of active flux observer

can be used in a wide speed range.

Because of the simple estimation model and wide operation range, AFO was exploited for the sensorless control of EESM in other researches. In [7], AFO is analyzed and compared with other estimation methods such as the extended Kalman filter (EKF) and HF signal injection method. The improved method of AFO was implemented by compensating the stator current harmonics with rotor current ripple components in [69]. Although the low-speed range performance is improved, AFO requires an additional initial position identification method for standstill condition. Besides, the compensation of parameter variation demands pre-identification of model parameters under various operation conditions.

3.2.2 State observers

To enhance the estimation performance, modern control theory has been applied to the model-based method. A state feedback structure is used to analyze the system's observability and improve the estimation performance under measurement noise and system nonlinearity.

The DO is a robust control method and has been actively used due to its simple structure and suitability in various applications. In the DO-based control, internal and external disturbances are estimated by using a plant model and system states. As a result, the robustness of a system is simply achieved by disturbance rejection control [70]. A general block diagram of DO in the frequency domain is illustrated in Figure 3.7.

In Figure 3.7, $u(s)$, $d(s)$, $y(s)$, $G(s)$, and $Q(s)$ represent the system input, disturbance, system output, system model and Q-filter. The Q-filter is essential in practical realization because it makes the system's inverse transfer function, $1/G(s)$, into a causal system. Therefore, a low

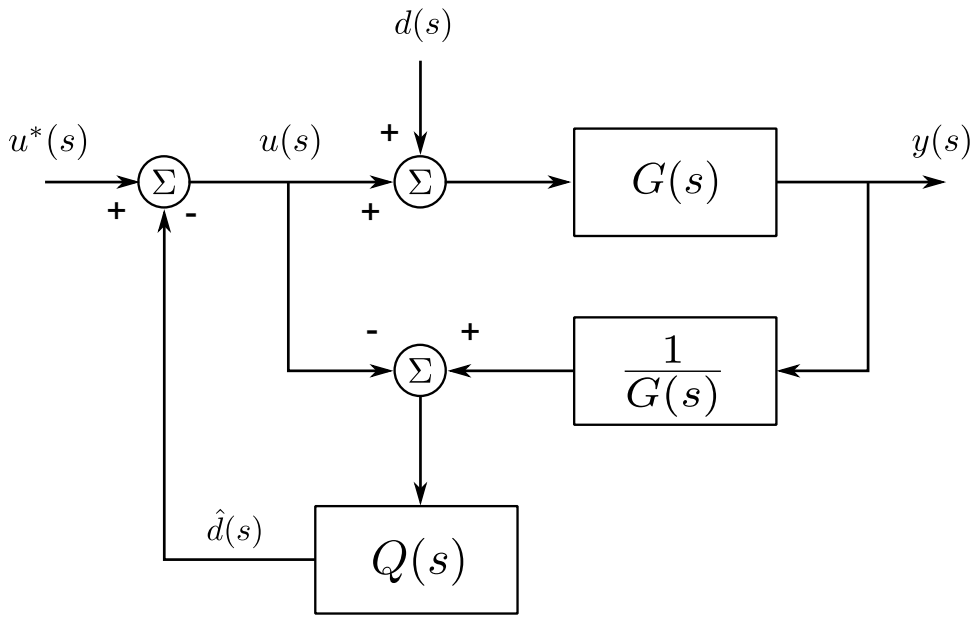

Figure 3.7: Block diagram of disturbance observer (DO)

pass filter (LPF) is generally used in the design of the Q-filter. As the disturbance rejection property mainly depends on the frequency characteristics of the Q-filter, the design of the Q-filter is crucial [71]. In Figure 3.7, the disturbance, $d(s)$, can be estimated by subtracting the input signal, $u(s)$, from the inversely calculated input signal. The system output is expressed as

$$\begin{aligned} y(s) &= G(s)\left(u(s) + d(s)\right) \\ &= G(s)\,u(s) + G(s)\,d(s) \end{aligned} \tag{3.41}$$

As shown in (3.41), the system is expressed as a two-input system, which has inputs of $u(s)$ and $d(s)$. From the DO structure, the estimated disturbance is expressed as

$$\hat{d}(s) = \left(\frac{1}{G(s)}y(s) - u(s)\right)Q(s) \tag{3.42}$$

Since the Q-filter is designed as a LPF having a steady-state gain of 1, the Q-filter in the low-frequency range is given as

$$\lim_{\omega \to 0} Q(j\omega) = 1 \tag{3.43}$$

Generally disturbance is dominant in the low-frequency range. Supposing the frequency

characteristics hold in Figure 3.7, (3.42) can be expressed in the low-frequency range as

$$\hat{d}(s) = \frac{1}{G\left(s\right)} y\left(s\right) - u\left(s\right) \tag{3.44}$$

Substituting (3.41) for (3.44) yields

$$\begin{aligned} \hat{d}(s) &= \frac{1}{G(S)}\Big(G(s)u(s) + G(s)d(s)\Big) - u(s) \\ &= u(s) + d(s) - u(s) \\ &= d(s) \end{aligned} \tag{3.45}$$

As shown in (3.45), the disturbance can be estimated with the DO. As a result, the compensation of disturbance can be achieved effectively.

By extending the concept of the disturbance, unmeasurable model variables, model uncertainty, and parameter perturbation can be considered as the disturbance. As a result, DO has been widely used also in estimation methods.

In [23], the DO was adopted to estimate the rotor position by defining the disturbance term as the mutually induced voltage in the stator winding by the field current. In the estimated rotor reference frame, the EESM model is expressed as

$$\boldsymbol{u}_s^{\hat{r}} = R_s \boldsymbol{i}_s^{\hat{r}} + \frac{d}{dt}\boldsymbol{L}_s^r \boldsymbol{i}_s^{\hat{r}} + \frac{d}{dt}\boldsymbol{R}\left(\tilde{\theta}_r\right)\boldsymbol{M}_{df}^r i_f + \omega \boldsymbol{J}\boldsymbol{L}_s^r \boldsymbol{i}_s^{\hat{r}} + \omega \boldsymbol{R}\left(\tilde{\theta}_r\right)\boldsymbol{J}\boldsymbol{M}_{df}^r i_f \tag{3.46}$$

To apply the DO for the rotor position estimation, the system model and two disturbance terms are defined as

$$\boldsymbol{u}_{s.fund}^r = R_s \boldsymbol{i}_s^{\hat{r}} + \frac{d}{dt}\boldsymbol{L}_s^r \boldsymbol{i}_s^{\hat{r}} + \omega \boldsymbol{J}\boldsymbol{L}_s^r \boldsymbol{i}_s^{\hat{r}} \tag{3.47}$$

$$\boldsymbol{d}_{HF} = \begin{bmatrix} d_{d.HF} \\ d_{q.HF} \end{bmatrix} = \frac{d}{dt}\begin{bmatrix} M_{df}\cos\tilde{\theta}_r \\ M_{df}\sin\tilde{\theta}_r \end{bmatrix} i_f \tag{3.48}$$

$$\boldsymbol{d}_{ind} = \begin{bmatrix} d_{d.ind} \\ d_{q.ind} \end{bmatrix} = \omega \begin{bmatrix} -M_{df}\sin\tilde{\theta}_r \\ M_{df}\cos\tilde{\theta}_r \end{bmatrix} i_f \tag{3.49}$$

where $\boldsymbol{u}_{s.fund}^r$, $\boldsymbol{d}_{HF}$, and $\boldsymbol{d}_{ind}$ represent the fundamental system model, the high-frequency

disturbance, and the induced disturbance. The high-frequency disturbance is generated by the rotor current ripple and dominant in the low-speed range of EESM. The induced disturbance is the back EMF and dominant in the middle- and high-speed range. The disturbance terms can be calculated with the proposed disturbance observer. Therefore the estimation angle error can be obtained. From (3.48) and (3.49), the position estimation error can be obtained as

$$\tilde{\theta}_{HF} = \arctan\left(\frac{d_{q.HF}}{d_{d.HF}}\right) \tag{3.50}$$

$$\tilde{\theta}_{ind} = \arctan\left(\frac{-d_{d.ind}}{d_{q.ind}}\right) \tag{3.51}$$

The rotor position can be calculated by a tracking type observer, which has an input signal of position estimation error in either (3.50) or (3.51).

The two estimations are based on two different principles, which emerge in the different frequency ranges. The rotor current ripple induces the high-frequency disturbance. As a result, the frequency of $\boldsymbol{d}_{HF}$ is identical to the PWM frequency of the rotor winding. The frequency of the induced disturbance is proportional to the rotor speed. Hence, $\boldsymbol{d}_{ind}$ is used to estimate the rotor position in the middle- and high-speed range. $\boldsymbol{d}_{HF}$ is used in the low-speed range, where the frequency separation is guaranteed. Therefore, two estimation results are combined linearly with respect to the estimated rotor speed. The combination equation will be presented in 3.3. The experimental results show that the proposed method estimates the rotor angle under a certain error level, including the estimator transition region. Therefore, the method yields satisfactory results without injecting an addition signal for a wide-speed operation range.

As another approach with modern control theory, the model reference adaptive system (MRAS) is exploited for speed sensorless control of EESM in [72]. MRAS is an adaptive tracking method that can be applied to estimate model variables or parameters by comparing two models: a reference model and an adjustable model. In the proposed method, a current model flux observer is used as a reference model, and a reduced-order flux observer is used as an adjustable model. By the adaptive controller, the two models are compared, and the rotor speed can be estimated. The sensorless speed control with MRAS is validated under load torque varying conditions in the paper.

To understand the model-based methods analytically, the observability of EESM has been analyzed in [73]. According to the analysis, the observability of EESM is guaranteed if the speed of the observability vector is different from the rotor speed. The most common case, which does not satisfy the condition, is when the rotor is at a standstill with no flux changing

in all windings. Therefore, to prevent the loss of the observability of EESM, high-frequency signal injection to the rotor or stator winding is necessary at zero speed.

3.3 Hybrid Sensorless Control Method

As shown in the previous sections, the saliency-based method and the model-based method utilize different characteristics of an electric machine. As a result, the saliency-based method results in an excellent performance in the low-speed range, including a standstill. On the other hand, the model-based method achieves accurate position estimation in the middle- and high-speed range, where sufficient EMF is induced. To achieve the whole-speed range sensorless control, the hybrid sensorless control method has been investigated [23, 25]. The hybrid sensorless control method combines the two types of sensorless control. The combination strategy is generally defined as

$$\hat{\theta}_h = \begin{cases} \hat{\theta}_{saliency}, & \text{if } \hat{\omega}_h < \omega_1 \\ (1-\omega_{trans})\,\hat{\theta}_{saliency} + \omega_{trans}\hat{\theta}_{model}, & \text{if } \omega_1 \leq \hat{\omega}_h \leq \omega_2 \\ \hat{\theta}_{model}, & \text{if } \hat{\omega}_h > \omega_2 \end{cases} \tag{3.52}$$

where ω_{trans} is defined as

$$\omega_{trans} = \frac{\hat{\omega}_h - \omega_1}{\omega_2 - \omega_1} \tag{3.53}$$

In (3.52), $\hat{\theta}_{saliency}$, $\hat{\theta}_{model}$, and $\hat{\theta}_h$ represent the estimated position by the saliency-based, model-based, and hybrid sensorless control method. In (3.53), $\hat{\omega}_h$, ω_1 and ω_2 represent the estimated speed by the hybrid method, the low-speed threshold, and the high-speed threshold for the transition region. As shown in (3.52), the two methods estimate the position independently in the low- and high-speed range. In the transition region, the estimated positions are combined linearly.

The hybrid sensorless method in previous research has been validated experimentally and achieved the wide-speed range sensorless control. Nevertheless, the transition speed threshold and strategy need to be decided carefully. Since the transition is depending on the estimated speed, the stability problem should be considered.

3.4 Summary

The sensorless control of EESM is categorized as a saliency-based and a model-based method. The saliency-based method of EESM injects the HF signal or utilizes inherent HF components to extract the saliency of EESM. Therefore the method has low dependency on model parameters. However, the current controller bandwidth has a frequency limitation due to the high-frequency injection signal and the use of filters. Moreover, the voltage margin for the signal injection may not be sufficient in the high-speed range. On the other category, the model-based method estimates the rotor position by using a mathematical model of EESM. The active flux concept or state observers are applied in the method. The method provides satisfactory performance in the middle- and high-speed range. However, estimation performance is not guaranteed at a standstill and in the low-speed range owing to insufficient EMF. Therefore, a hybrid sensorless control , which combines the saliency-based method and the model-based method, was applied to EESM for the whole speed range operation. The method applies the saliency-based method for a low-speed range and the model-based method for high-speed range. In combining two types of sensorless control, stable estimator transition is crucial since the transition is based on the estimated rotor speed. Although the hybrid sensorless control has achieved the whole speed range sensorless control, some previous issues still remain, such as the parameter dependency, the limitation in control bandwidth, and complex frequency demodulation methods.

CHAPTER 4

Sensorless Control based on Mutual Induction

Sensorless control of EESM has been researched with the unique variable, field current. The S2R and R2S methods utilize the field winding as receiver winding and transmitter winding of the HF excitation signal. As a result, various approaches have been suggested in previous researches. On the other hand, PWM-based sensorless control methods proved estimation performance in a wide-speed operation range due to the wide bandwidth of the position estimation. The method can also reduce the side effects of the signal injection method by using the fundamental PWM signal as an excitation signal.

The PWM-based sensorless control method of EESM using the mutual induction is proposed in this thesis. The proposed method utilizes the additional variable of field current and the benefit of the PWM-based method. The advantages of the proposed method are a wide-speed operation range with a single algorithm, a parameter-free position estimation algorithm, and fast position estimation within a PWM cycle.

In this chapter, a sensorless control method motivated by a resolver is discussed shortly. After that, the relationship between the field current and the stator PWM signal is derived from the analysis of the field current. Given the relationship, a position estimation method is suggested, and the implementation of the proposed method is presented. In the realization of the method, practical issues and corresponding modification methods are explained.

4.1 Position Estimation Motivated by a Resolver

A resolver is an electromechanical position sensor, which is installed on the rotor shaft. Due to its ruggedness and reliability, resolvers are widely used in industrial, automotive, and military applications. Resolvers require installation space and interface electronics, such as a resolver to-digital-converter (RDC).

A resolver consists of a primary winding and a secondary winding. Generally, the primary winding is on the rotor structure, and a sinusoidal excitation signal is applied to the primary winding. The two secondary windings are placed orthogonally to each other on the stator. As the excitation signal is applied to the primary winding, voltage is induced in the secondary winding depending on the rotor angle. The induced signals in the secondary windings have 90 degrees phase difference due to the orthogonality of the windings. Based on this property, the rotor position is measured.

The structure of EESM is similar to the structure of a resolver. In the stator reference frame, the windings of EESM can be illustrated as Figure 4.1.

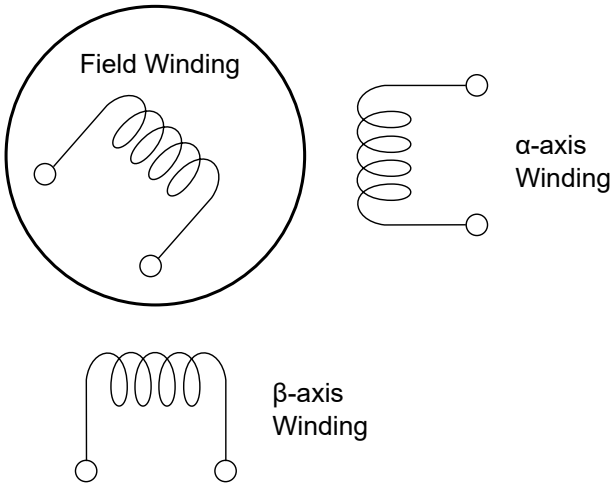

Figure 4.1: EESM field and stator windings

As shown in Figure 4.1, the field and stator windings of EESM correspond to the primary and secondary windings of a resolver. That means, if a sinusoidal excitation signal is applied to the field winding, the induced signals in the α- and β-axes stator windings can be used to calculate the rotor position. Therefore, the position estimation method motivated by a resolver is presented in this chapter.

The field current of EESM has inherent current ripples by the PWM switching. In this study, 1 kHz field current ripple occurs by the PWM setup. Therefore, the field current ripple is

considered as the excitation signal, and the α- and β-axes current are used as the induced signal in the secondary windings of a resolver. The induced signal in the stator current appears with the fundamental stator current. Thus, a BPF is applied to extract the induced signal. The transfer function of the second-order BPF with 1 kHz bandwidth is given as

$$\begin{aligned} H_{BPF}(s) &= \frac{2\zeta\omega_n s}{s^2 + 2\zeta\omega_n s + \omega_n^2} \\ &= \frac{8884s}{s^2 + 8884s + 3.948 \times 10^7} \end{aligned} \tag{4.1}$$

where ζ and ω_n represent the damping ratio and the natural frequency of the filter. In the design of the filter, ζ and ω_n are set to 0.707 and $2\pi * 1000$. With the BPF in (4.1), the 1 kHz frequency components in the stator current signal can be extracted without a phase delay.

Figure 4.2 shows the induced stator current obtained with the BPF. In Figure 4.2, EESM rotates at 1,000 rpm with no load condition. The field current ripple shows 1 kHz PWM frequency, and the ripple is assumed as a sinusoidal signal. The bandpass filtered stator current signals in the α- and β-axes windings show the induced signals by the excitation signal. As shown in Figure 4.2, the frequency of the induced signals is also 1 kHz, and the amplitude varies depending on the rotor angle. Those results are well-matched with the resolver signals in the primary and secondary windings. The field current and the induced stator current signals can be expressed as

$$i_{exc} = I_0 \sin(\omega_{exc} t) \tag{4.2}$$

$$BPF(i_\alpha) = I_1 \cos\theta_r \sin(\omega_{exc} t) \tag{4.3}$$

$$BPF(i_\beta) = I_1 \sin\theta_r \sin(\omega_{exc} t) \tag{4.4}$$

where I_0, I_1, and ω_{exc} represent the amplitude of the excitation signal, the amplitude of the induced signal, and the frequency of the excitation signal, respectively. As shown in (4.3) and (4.4), the amplitudes of the induced signals contain the rotor position information. Therefore, the rotor position can be calculated as

$$\theta_r = \arctan\left(\frac{BPF(i_\beta)}{BPF(i_\alpha)}\right) \tag{4.5}$$

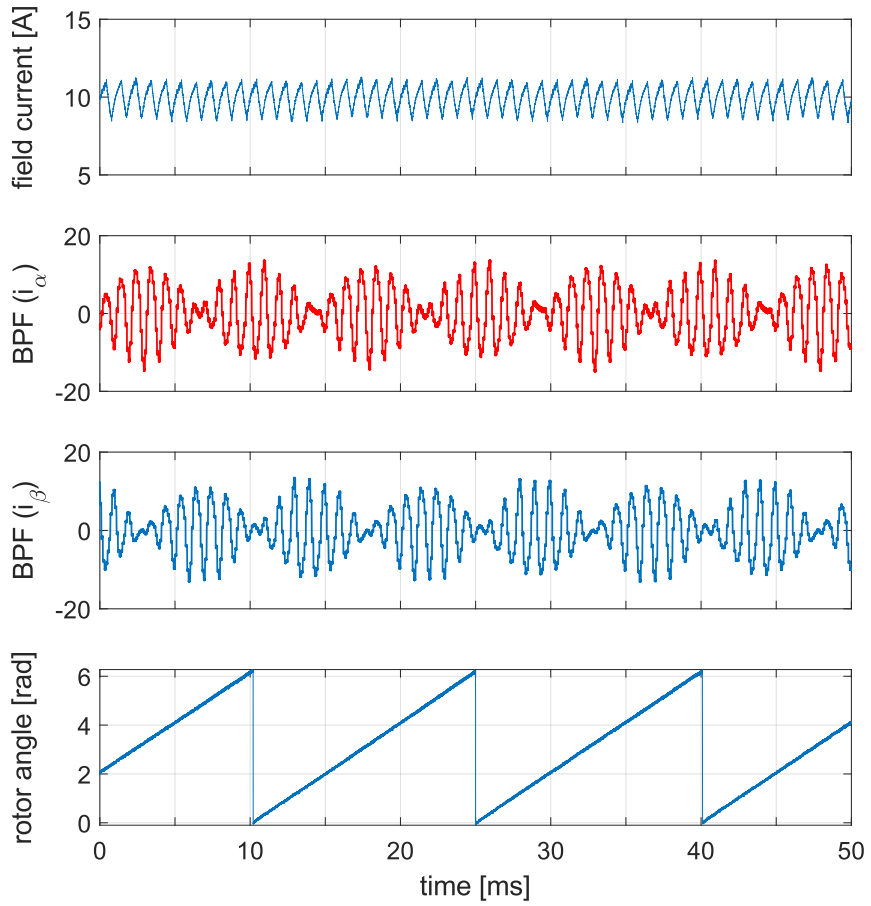

Figure 4.2: Bandpass filtered stator current

In this study, the envelope of the induced signal is obtained by sampling the induced current when the field winding PWM signal is switched on and off. As the stator current is sampled with respect to the field winding switching signal, the peak amplitude of the induced signal can be obtained with the simple sampling method. The rotor position is estimated from the induced stator current and (4.5) as shown in Figure 4.3.

Figure 4.3 shows the experimental results of the position estimation method motivated by a resolver while EESM rotates at 1,000 rpm. The maximum estimation error is 0.32 radian, and the average estimation error is 0.16 radian in the experimental results. As shown in Figure 4.3, the position estimation method shows satisfactory results.

Although it was shown that the resolver-motivated method could be applied to EESM, there are differences between a resolver and an EESM: First, the excitation signal in the field current is not sinusoidal and depends on the PWM duty. The assumption of the sinusoidal excitation

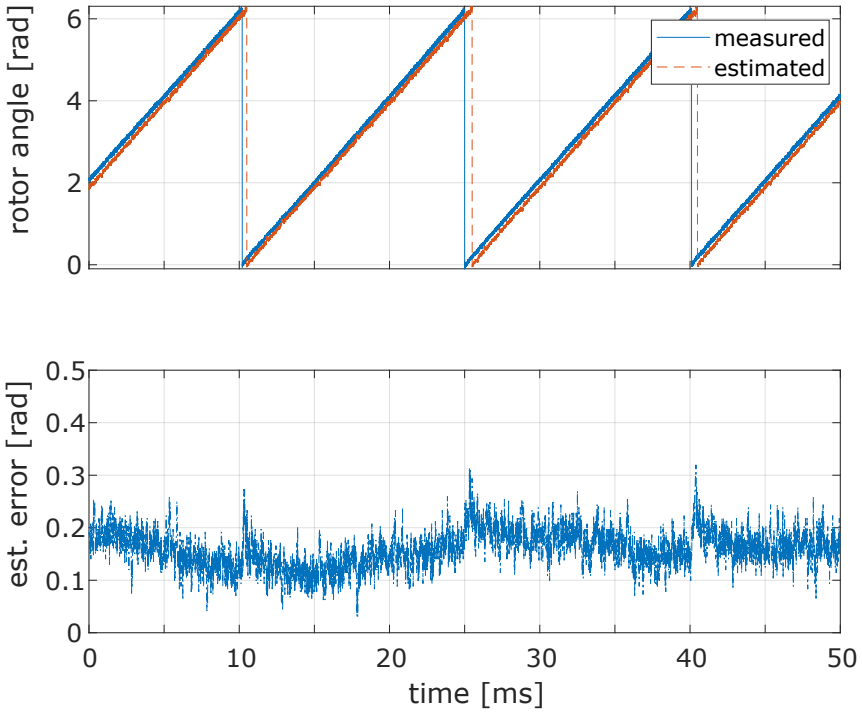

Figure 4.3: Position estimation motivated by a resolver

signal holds when the PWM duty is around 50 %. Second, the induced current in the stator winding is affected by the saturation effect of the winding. Thus, the estimation error can be increased in the load condition. Third, the frequency of the excitation signal is fixed to the PWM frequency of the field winding. Considering that the general frequency range of the resolver excitation signal is between 8 and 16 kHz [65], the estimation in the high-speed range can be limited with low PWM frequency. Therefore, the resolver-motivated estimation method can be applied to the sensorless control under the consideration of those differences.

The position estimation method motivated by a resolver can estimate the rotor position in one PWM cycle of the field winding. That is, the estimation bandwidth is ideally maximum 1 kHz, which can limit the sensorless control in the wide-speed range operation. Therefore, the method is not investigated further in this thesis.

4.2 Rotor Position Estimation

4.2.1 Field current analysis

The proposed method is based on the mutual induction between the stator and rotor windings. Specifically, the relationship between the stator voltage and the corresponding mutually induced field current* is exploited in the method. Since the characteristic of field current is essential in the proposed method, the field current signal is analyzed in a frequency domain and a time domain.

The frequency spectrum of the field current during constant current control is obtained with fast Fourier transform (FFT) to analyze the field current in a frequency domain. Figure 4.4 shows the frequency spectrum of the field current.

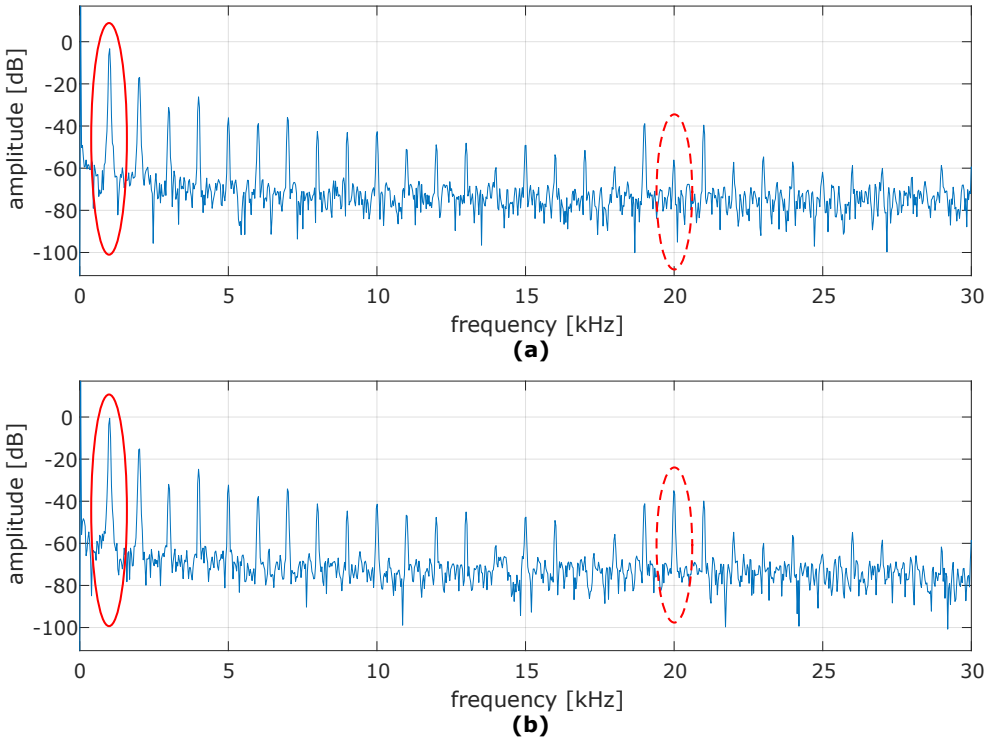

Figure 4.4: Frequency spectrum of field current: (a) $I_f = 10$ A, $I_d = I_q = 0$ A and (b) $I_f = 10$ A, $I_d = 100$ A, $I_q = 0$ A

In Figure 4.4, the field current and q-axis current are controlled to 10 A and 0 A, respectively.

*The mutually induced field voltage produces field current, and the field current is referred to as the mutually induced field current in this study.

The d-axis current is controlled to 0 A in Figure 4.4 (a) and 100 A in Figure 4.4 (b). The PWM switching frequencies of the rotor and stator winding are 1 kHz and 10 kHz in the experiment. In both results, 1 kHz of PWM frequency in the field current is found clearly in red circles. As the d-axis current is increased to 100 A, 20 kHz harmonic appears in the dashed red circle in Figure 4.4 (b). However, when the d-axis current is 0 A, noticeable 20 kHz harmonic does not appear in the dashed red circle in Figure 4.4 (a). In SVM, the actual active voltage vector is applied twice per PWM cycle, i.e., the frequency of active voltage vector in the stator winding is 20 kHz. Therefore, the frequency spectrum shows that the active vector in the stator winding induces the field current, and its frequency is two times faster than the stator PWM frequency in SVM.

To analyze the field current response by the stator active vector in a time domain, the field current under alternating stator active voltage is shown in Figure 4.5. The field current is measured while the current is controlled to 10 A, and the stator reference voltage is commanded as: $|u_s^{s*}| = 5$ (V), $\angle u_s^{s*} = \pi/6, 7\pi/6$ rad. To keep the rotor speed constant, the phase of stator reference voltage alternates $\pi/6$ and $7\pi/6$ rad (π rad difference) in every PWM cycle. During the measurement, the rotor is rotated by a load machine with a constant speed of 2,000 rpm.

Figure 4.5 (a) shows the field current while alternating stator voltage is applied, and the rotor is rotating. The fundamental field current fluctuates by the rotor PWM switching, of which the frequency is 1 kHz. However, the HF ripple of the field current does not show the same pattern but a periodic pattern with respect to the rotor angle. Figure 4.5 (b), (c), and (d) show the field current for one stator PWM cycle when the rotor angle is about $\pi/6$, $2\pi/3$, and $7\pi/6$ rad, respectively. The three cases are captured when the stator voltage vector is $|u_s^{s*}| = 5$ (V), $\angle u_s^{s*} = \pi/6$ in common. The gray area shows the period of the active voltage is applied. As shown in Figure 4.5 (b), (c), and (d), the field current response has a different pattern from each other. It seems that the mutually induced field current is related to the rotor angle. The field current slope in the gray area is symmetric with respect to the middle of a stator PWM cycle. Besides, the change of current slope is found in the area. Those phenomena correspond to the active vector applying pattern in SVM. Therefore, the mutually induced field current is related to the stator active voltage vector. The uncolored area shows the field current when a zero voltage vector is applied in the stator winding. Thus the current response reflects the fundamental field current.

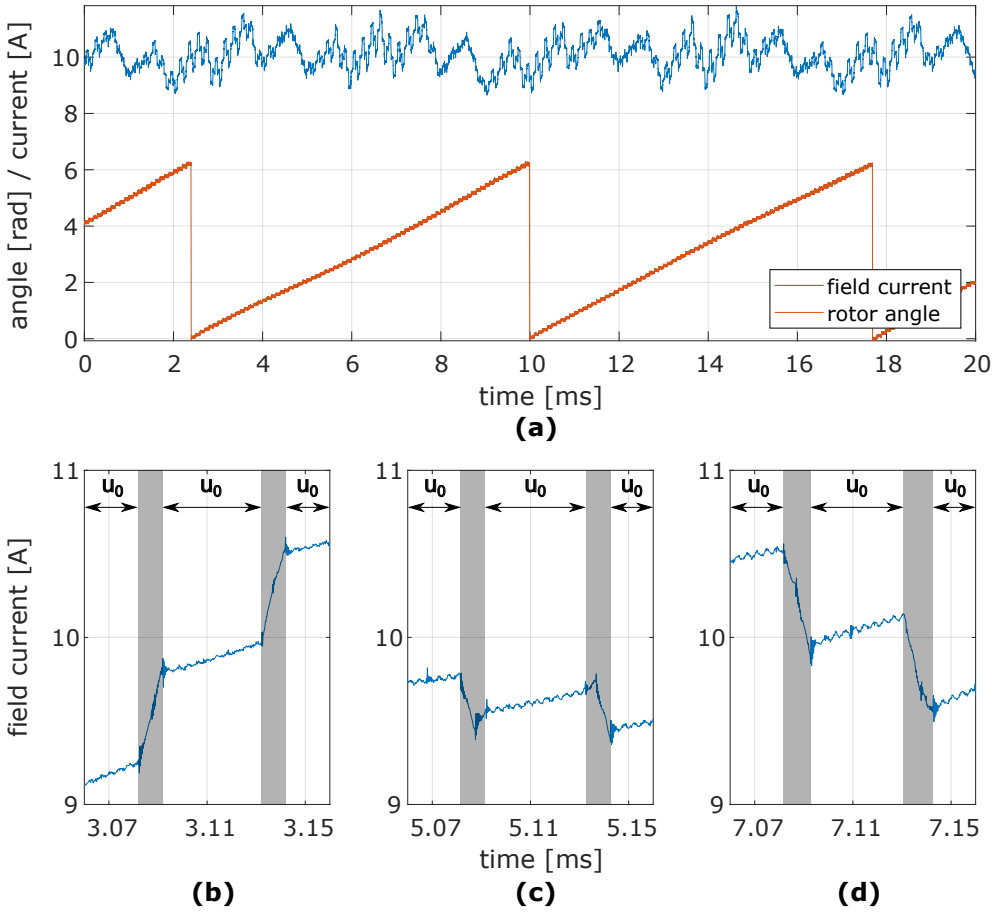

Figure 4.5: Field current response by alternating stator voltage: (a) $\omega_r = 2000$ rpm, (b) $\theta_r \approx \pi/6$, (c) $\theta_r \approx 2\pi/3$, and (d) $\theta_r \approx 7\pi/6$

4.2.2 Derivation of rotor position estimation equation

As shown in (2.65), the mutual inductance between the stator and rotor windings can be expressed as a function of the rotor angle in the stator reference frame. Therefore, the rotor angle can be calculated by measuring the mutual inductance. However, the mutual inductance of EESM cannot be measured directly since the fundamental current response appears in the field current simultaneously. To separate the mutual induction component from the fundamental current response, PWM excitation is utilized in the proposed method. Due to the frequency difference between the PWM excitation and the fundamental response, the mutual induction component can be extracted. Therefore, the mutual inductance can be calculated.

The HF-model of EESM in the stator reference frame is given as

$$\boldsymbol{u}^s_{s.HF} = \boldsymbol{L}^s_s \frac{d}{dt}\boldsymbol{i}^s_{s.HF} + \boldsymbol{M}^s_{sf}\frac{d}{dt}i_{f.HF} \tag{4.6}$$

$$u_{f.HF} = L_f \frac{d}{dt}i_{f.HF} + \boldsymbol{M}^{s\,T}_{sf}\frac{d}{dt}\boldsymbol{i}^s_{s.HF} \tag{4.7}$$

As shown in (4.6) and (4.7), the HF voltage equations of stator and rotor winding consist of self- and mutual inductance terms. Fundamental responses, resistive voltage drop and EMF, are neglected in the HF-model. In (4.6) and (4.7), two terms related to the field current are found: One is the second term on the right-side in (4.6), which is the mutually induced field current by stator voltage. The other is the first term on the right-side in (4.7), which is the self-induced field current by rotor voltage. The two HF-signals in the field winding appear in different frequency range by the different PWM switching frequency. Therefore, they can be separated by applying a filter to the field current. In the proposed method, the field current response of interest is the HF field current by stator voltage switching, which is expressed as $\boldsymbol{M}^s_{sf}\frac{d}{dt}i_{f.HF}$ in (4.6). The relationship between the stator voltage and the HF field current is given as

$$\boldsymbol{u}^s_{s.HF} = \boldsymbol{M}^s_{sf}\frac{d}{dt}i_{f.HF} \tag{4.8}$$

The geometric relationship between the stator voltage and the field current in the stator reference frame is illustrated in Figure 4.6.

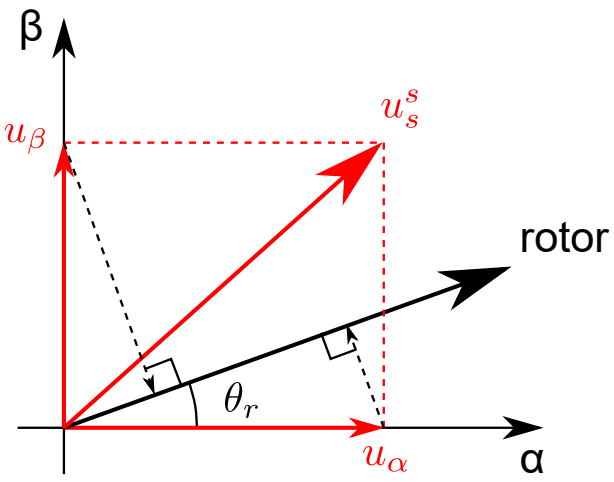

Figure 4.6: Relationship between stator voltage and field current

In Figure 4.6, the stator voltage vector, $\boldsymbol{u}^s_s$, is decomposed to u_α and u_β, and the two voltage vectors induce the field current. By the vector projection of u_α and u_β onto the rotor-axis, the

induced field current is given as

$$\begin{aligned} M_{sf}\frac{d}{dt}i_f &= u_\alpha \cos\theta_r + u_\beta \cos\left(\frac{\pi}{2} - \theta_r\right) \\ &= u_\alpha \cos\theta_r + u_\beta \sin\theta_r \\ &= \begin{bmatrix}\cos\theta_r & \sin\theta_r\end{bmatrix} \begin{bmatrix} u_\alpha \\ u_\beta \end{bmatrix} \end{aligned} \tag{4.9}$$

As shown in (2.66), M_{sf} is decided by the minimum air gap distance, the effective number of turns of the stator and field windings. By transposing the M_{sf}, the derivative of field current is expressed as

$$\begin{aligned} \frac{d}{dt}i_f &= \frac{1}{M_{sf}} \begin{bmatrix}\cos\theta_r & \sin\theta_r\end{bmatrix} \begin{bmatrix} u_\alpha \\ u_\beta \end{bmatrix} \\ &= \boldsymbol{M}_{sf}^{s}{}^{+}\, \boldsymbol{u}_s^s \end{aligned} \tag{4.10}$$

The mutually induced field current derived by the geometric relationship in (4.10) coincides with the HF-model of the field current in (4.8). In (4.10), the derivative of field current is decided by the stator voltage and the mutual inductance, which is expressed as a function of the rotor angle. Therefore, this relationship is used in the derivation of the position estimation equation.

In vector control, the stator voltage is applied as active voltage vectors and zero voltage vectors in the SVM method. SVM is one of the most commonly used PWM algorithms in AC machine drives due to the advantages of higher output voltage, less harmonic distortion, and lower switching losses [74]. Since the PWM excitation is utilized in the proposed method, the field current induced by the active voltage vector is used in the proposed method. Therefore, the relationship between the active voltage vector and corresponding field current response needs to be derived. Figure 4.7 shows the geometric relationship between the active voltage vector and the rotor in a space vector diagram.

In Figure 4.7, the stator reference voltage, $\boldsymbol{u}_s^{s*}$, is applied as two active voltage vectors of u_I^* and u_{II}^* in practice. Here, u_I and u_{II} are scaled active voltage vectors, and the relationship is

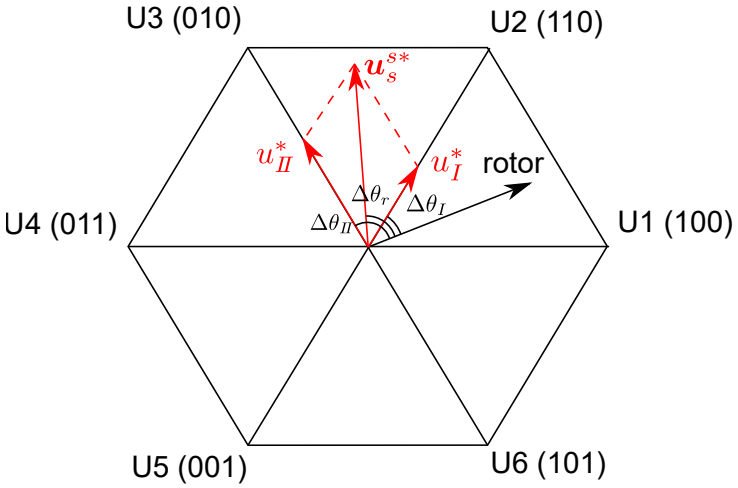

Figure 4.7: Active voltage vectors and the rotor position in a space vector diagram

defined as

$$\angle u_I = \angle u_{II} - \frac{\pi}{3} \tag{4.11}$$

The angle between the rotor and stator voltage vectors are defined as

$$\Delta\theta_r = \angle \boldsymbol{u}_s^{s*} - \theta_r \tag{4.12}$$

$$\Delta\theta_I = \angle u_I^* - \theta_r \tag{4.13}$$

$$\Delta\theta_{II} = \angle u_{II}^* - \theta_r \tag{4.14}$$

As the reference voltage is applied with active voltage vectors, the current response depends on the applied active voltage vectors. In the space vector diagram, the mutual induction is expressed as a vector projection of the active voltage vector onto the rotor-axis. The current response by the stator voltage vector is given as

$$\frac{d}{dt} i_f = \frac{1}{M_{sf}} |\boldsymbol{u}_s^{s*}| \cos \Delta\theta_r \tag{4.15}$$

$$\frac{d}{dt} i_{fI} = \frac{1}{M_{sf}} |u_I^*| \cos \Delta\theta_I \tag{4.16}$$

$$\frac{d}{dt} i_{fII} = \frac{1}{M_{sf}} |u_{II}^*| \cos \Delta\theta_{II} \tag{4.17}$$

where $\frac{d}{dt} i_f$, $\frac{d}{dt} i_{fI}$, and $\frac{d}{dt} i_{fII}$ represent the rate of change of the mutually induced field current

by the stator reference voltage, active voltage vector I, and active voltage vector II, respectively. As shown in (4.15) $\sim$ (4.17), the mutually induced field current is decided by the mutual inductance, the magnitude of the stator voltage vector, and the angle between the stator voltage vector and the rotor.

To derive the angle estimation equation, (4.16) and (4.17) are rearranged as

$$\cos\Delta\theta_I = \frac{M_{sf}}{|u_I^*|}\frac{d}{dt}i_{fI} \tag{4.18}$$

$$\cos\Delta\theta_{II} = \frac{M_{sf}}{|u_{II}^*|}\frac{d}{dt}i_{fII} \tag{4.19}$$

In (4.18) and (4.19), the derivative of field current can be obtained by calculating the slope of the field current. Therefore, the field current slope is defined as

$$m_I = \frac{d}{dt}i_{fI} \tag{4.20}$$

$$m_{II} = \frac{d}{dt}i_{fII} \tag{4.21}$$

where m_I and m_{II} represent the field current slopes when the active vectors u_I^* and u_{II}^* are applied. Considering the magnitude of the active voltage vector in (4.18) and (4.19), the slopes of the mutually induced field current scaled by the corresponding active voltage vector are defined as

$$m_I' = \frac{m_I}{|u_I^*|} \tag{4.22}$$

$$m_{II}' = \frac{m_{II}}{|u_{II}^*|} \tag{4.23}$$

With the scaled current slopes in (4.22) and (4.23), (4.18) and (4.19) are rewritten as

$$\cos\Delta\theta_I = M_{sf}\, m_I' \tag{4.24}$$

$$\cos\Delta\theta_{II} = M_{sf}\, m_{II}' \tag{4.25}$$

To verify (4.24) and (4.25), m_I' and m_{II}' are calculated while EESM is rotated by a load machine. Figure 4.8 shows the experimental result. In the experiment, the field current is controlled to 10 A, and the stator reference voltage is given as: $|u_s^{s*}| = 5$ (V), $\angle u_s^{s*} = \pi/6$ (=

$30°$), $7\pi/6$ $(= 210°)$ rad. In the experiment, the speed of EESM is 2,000 rpm.

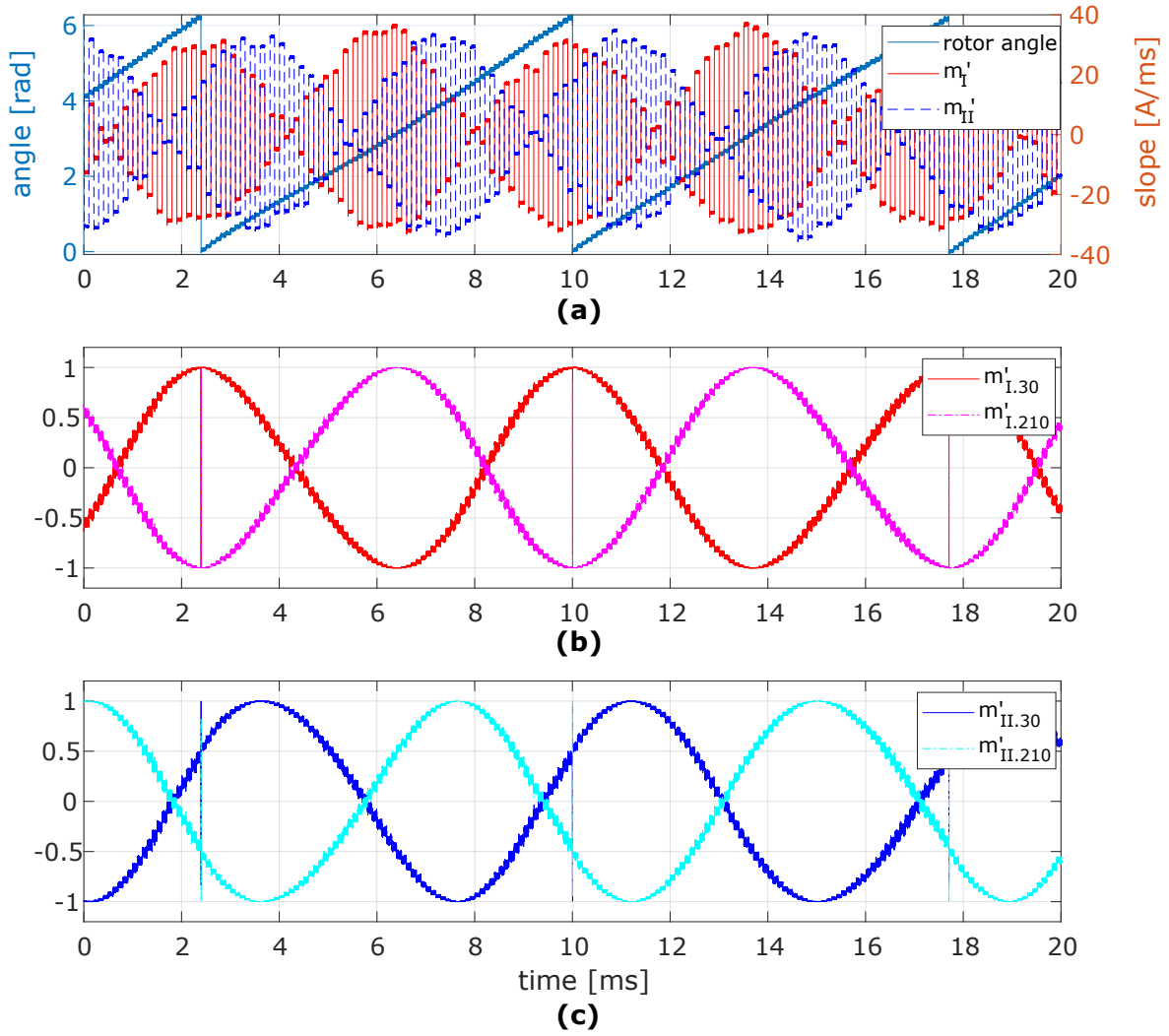

Figure 4.8: Slope of mutually induced field current: (a) measurement of current slope and rotor angle, (b) calculated current slope by (4.26) and (4.27) in offline, and (c) calculated current slope by (4.28) and (4.29) in offline

Figure 4.8 (a) shows the slope of the mutually induced field current, and the slope calculation was done by the main controller online. The y-axis on the left side of Figure 4.8 indicates the rotor angle, and the y-axis on the right side indicates the slope of the field current. In Figure 4.8 (a), inductance parameters are not considered, but the applied active voltage and the corresponding field current change. To verify the result, offline calculation results with the measured rotor angle are shown in Figure 4.8 (b) and (c). The equations for the offline

calculation are given as

$$m'_{I.30} = \cos(0^\circ - \theta_r) \tag{4.26}$$

$$m'_{I.210} = \cos(180^\circ - \theta_r) \tag{4.27}$$

$$m'_{II.30} = \cos(60^\circ - \theta_r) \tag{4.28}$$

$$m'_{II.210} = \cos(240^\circ - \theta_r) \tag{4.29}$$

As the phase of stator voltage vector alternates 30° and 210° with PWM frequency, the pair of applied active vector angle, $(\angle u_I, \angle u_{II})$, alternates (0°, 60°) and (180°, 240°). In Figure 4.8 (a), m'_I and m'_{II} show the field current slope by u_I and u_{II} while the rotor is rotating. Due to the alternating voltage vector, m'_I and m'_{II} show the combined result of two alternating vectors. That is, the slope result of m'_I in Figure 4.8 (a) corresponds to the combination of $(m'_{I.30}, m'_{I.210})$ in Figure 4.8 (b). The m'_{II} in Figure 4.8 (a) corresponds to the combination of $(m'_{II.30}, m'_{II.210})$ in Figure 4.8 (c). By comparing the slope results in Figure 4.8 (a), (b) and (c), it is verified that the field current slope can be expressed as a cosine function of the angle between the active voltage vector and the rotor angle.

Additionally, Figure 4.8 (a) shows that a period of the current slopes, m'_I and m'_{II}, are identical to the period of rotor angle. Since the change of field current slope is caused by the structural saliency of EESM, the periods of the rotor and the field current slope are to be the same. This is different from the general saliency-based method, which is based on the magnetic saliency of a machine. The saliency term is expressed generally as a trigonometric function of $2\theta_r$, as shown in (3.2). Therefore, the field current slope contains the rotor position information, including the polarity of a rotor.

As the slope of the mutually induced field current contains the rotor angle information, the rotor angle can be estimated from the current slope. To derive the estimation equation, two current slopes are exploited. In the space vector diagram, two active voltage vectors have a phase difference of $\pi/3$. Using this property and the trigonometric identity, (4.25) is expressed

as

$$\begin{aligned} M_{sf} m'_{II} &= \cos \Delta\theta_{II} \\ &= \cos\left(\Delta\theta_I + \frac{\pi}{3}\right) \\ &= \cos \Delta\theta_I \cos\frac{\pi}{3} - \sin \Delta\theta_I \sin\frac{\pi}{3} \\ &= \frac{1}{2}\cos \Delta\theta_I - \frac{\sqrt{3}}{2}\sin \Delta\theta_I \end{aligned} \tag{4.30}$$

To make $\sin \Delta\theta_I$ the subject of the equation, (4.30) is rearranged as

$$\begin{aligned} \sin \Delta\theta_I &= \frac{1}{\sqrt{3}}\cos \Delta\theta_I - \frac{2}{\sqrt{3}} M_{sf} m'_{II} \\ &= \frac{M_{sf}\ m'_I - 2M_{sf} m'_{II}}{\sqrt{3}} \end{aligned} \tag{4.31}$$

Given the (4.24) and (4.31), the $\Delta\theta_I$ can be calculated with an arctangent function. The calculation equation is given as

$$\begin{aligned} \Delta\theta_I &= \arctan\left(\frac{\sin \Delta\theta_I}{\cos \Delta\theta_I}\right) \\ &= \arctan\left(\frac{\frac{M_{sf} m'_I - 2M_{sf} m'_{II}}{\sqrt{3}}}{M_{sf} m'_I}\right) \\ &= \arctan\left(\frac{m'_I - 2m'_{II}}{\sqrt{3} m'_I}\right) \end{aligned} \tag{4.32}$$

Consequently, the angle between the rotor position and the active voltage vector can be calculated with (4.32). In the derivation of (4.32), the mutual inductance is canceled out in the fraction formula. The mutual inductance varies depending on the operating point, as shown in 2.3.2. Thus, a position estimation algorithm, which uses the inductance parameter, requires a LUT of inductance or an inductance identification method. However, the proposed method can estimate the rotor position without any parameter values. Hence the parameter measurement or identification is not necessary. Only the field current slope and the active voltage vector are required to estimate the rotor position with the proposed method.

In the derivation of the position estimation equation in (4.30), $\Delta\theta_{II}$ can be expressed differ-

ently depending on the rotor angle. Considering all cases, $\Delta\theta_{II}$ is expressed as

$$\Delta\theta_{II} = \begin{cases} \Delta\theta_I + \frac{\pi}{3}, & \text{if } \theta_r < \angle u_I^* \\ -\Delta\theta_I + \frac{\pi}{3}, & \text{if } \angle u_I^* \leq \theta_r \leq \angle u_{II}^* \\ \Delta\theta_I - \frac{\pi}{3}, & \text{if } \theta_r > \angle u_{II}^* \end{cases} \tag{4.33}$$

where the relationship $\angle u_I^* < \angle u_{II}^*$ holds by the definition in (4.11).

Due to the y-axis symmetry of the cosine function, $\cos\Delta\theta_{II}$ results the same value in the above conditions. Therefore, (4.32) can be used for the position estimation in any active voltage vector and rotor position.

Since $\Delta\theta_I$ is the relative angle between the rotor and the active voltage vector, the absolute rotor angle can be obtained by including the angle of the active vector. Based on the space vector diagram shown in Figure 4.7, the absolute rotor angle can be calculated as

$$\theta_r = \angle u_I^* - \Delta\theta_I \tag{4.34}$$

As shown in (4.34), the rotor angle can be estimated with the proposed method.

4.2.3 Signal processing of mutually induced field current

The mutually induced field current by the stator PWM switching appears dominantly in the HF range. Generally, the HF response is obtained with a bandpass filter (BPF) or a frequency demodulation method. In the proposed method, the HF field current is obtained by simple arithmetic operations with respect to the PWM switching sequence. This subsection presents the signal processing method to obtain the mutually induced field current.

To extract the mutual induction term from the field current, the rotor voltage is assumed as constant voltage, and the field current is measured with a high sampling rate. The assumption can be considered valid due to the difference in PWM frequency in the stator and rotor windings. Given the resistance and inductance value of the stator and rotor windings in Appendix B, the time constants of the stator and rotor winding are calculated as 2.7 and 24.9 ms. As a result, the PWM frequencies for the stator and rotor windings are set to 10 kHz and 1 kHz, respectively. Therefore, the switching of the rotor voltage is not considered in the measurement of the field current. The high sampling rate of field current is implemented with an oversampling method

in this study, and the fundamental response is removed in the field current signal processing. Consequently, the HF field current response by the stator voltage switching can be obtained with the assumption of constant rotor voltage, the oversampling method, and the field current signal processing.

In the proposed estimation method, input signals of the algorithm are active voltage vector and the derivative of mutually induced field current by active voltage vector. The active voltage vector is already calculated in the previous sampling time, thus it is known information. The current derivative can be measured directly by a current derivative sensor. However, the sensor is not commonly used in general AC drive configurations. Therefore, the derivative of current is obtained by measuring the initial and final current value in the active time and calculating the rate of change of the current. The concept of current sampling with PWM switching states is depicted in Figure 4.9.

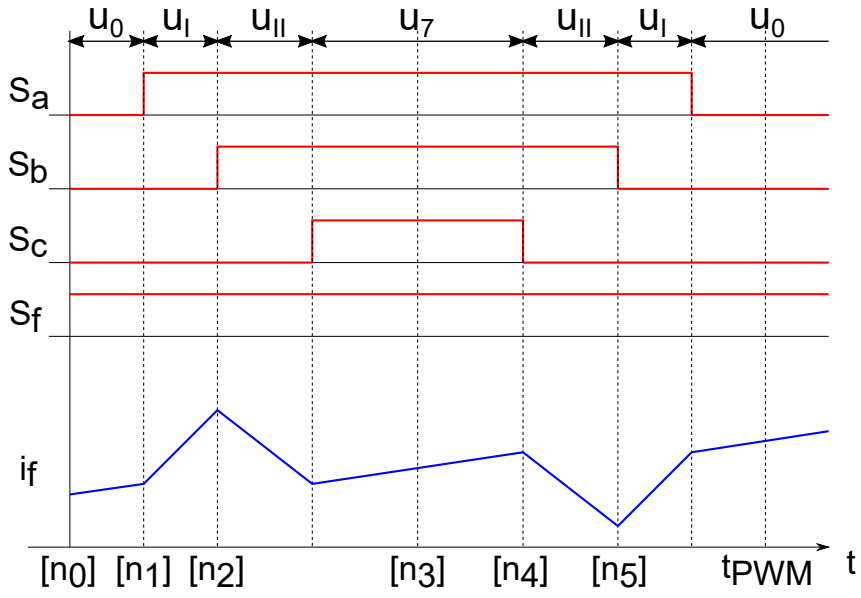

Figure 4.9: Concept of current sampling and PWM switching states [75]

In Figure 4.9, $[n_n]$ represents the time index for current sampling. Figure 4.9 shows the switching states of stator and field windings and the field current response for one PWM cycle. The switching state of the field winding, S_f, is assumed constant in Figure 4.9. The field current response contains both fundamental current response and mutual induction by the stator PWM switching.

While the zero vectors, u_0 and u_7, are applied to the stator winding, the field current shows the fundamental response without any mutual induction from the stator winding. The fundamental signal of the field current is expressed as

$$i_f(t) = \begin{cases} \frac{U_{DC}}{R_f}\left(1 - e^{-\frac{R_f}{L_f}t}\right), & \text{if } S_f = 1 \\ \frac{U_{DC}}{R_f}e^{-\frac{R_f}{L_f}t}, & \text{if } S_f = 0 \end{cases} \tag{4.35}$$

where U_{DC} is a DC-link voltage, which is set to 48 volts. The slope of the fundamental field current is decided by the resistance and self-inductance of the rotor winding, switching states of the rotor winding, and the DC-link voltage. The fundamental field current slope is found when a zero voltage vector is applied in the stator winding, and it can be calculated as

$$m_{n_1 n_0} = m_{fund.0} = \frac{i_f[n_1] - i_f[n_0]}{t[n_1] - t[n_0]} \tag{4.36}$$

$$m_{n_4 n_3} = m_{fund.7} = \frac{i_f[n_4] - i_f[n_3]}{t[n_4] - t[n_3]} \tag{4.37}$$

where $m_{fund.0}$ and $m_{fund.7}$ represent the field current slope by the stator zero vector u_0 and u_7. $m_{n_1 n_0}$ and $m_{n_4 n_3}$ represent the field current slope in the time intervals of $[n_0, n_1]$ and $[n_3, n_4]$.

While the active voltage vectors, u_I and u_{II}, are applied to the stator winding, the mutual induction from the stator winding occurs and is superposed onto the fundamental signal. The fundamental current slope in the active time is assumed the same as the current slope in the previous zero voltage vector period. By the superposition property, the field current slope in the active time can be expressed as

$$m_{n_2 n_1} = m_{fund.0} + m_{u_I} \tag{4.38}$$

$$m_{n_5 n_4} = m_{fund.7} + m_{u_{II}} \tag{4.39}$$

where m_{u_I} and $m_{u_{II}}$ represent the mutually induced field current slopes by active voltage I and II. From Figure 4.9, (4.38) and (4.39) can be calculated as

$$m_{n_2 n_1} = \frac{i_f[n_2] - i_f[n_1]}{t[n_2] - t[n_1]} \tag{4.40}$$

$$m_{n_5 n_4} = \frac{i_f[n_5] - i_f[n_4]}{t[n_5] - t[n_4]} \tag{4.41}$$

Subtracting (4.36) and (4.37) from (4.38) and (4.39), the slope of the mutually induced field current can be obtained as

$$\begin{aligned} m_{u_I} &= (m_{fund.0} + m_{u_I}) - m_{fund.0} \\ &= m_{n_2 n_1} - m_{n_1 n_0} \end{aligned} \tag{4.42}$$

$$\begin{aligned} m_{u_{II}} &= (m_{fund.7} + m_{u_{II}}) - m_{fund.7} \\ &= m_{n_5 n_4} - m_{n_4 n_3} \end{aligned} \tag{4.43}$$

From the current sampling method in Figure 4.9, (4.42) and (4.43) can be calculated as

$$m_{u_I} = \frac{i_f[n_2] - i_f[n_1]}{t[n_2] - t[n_1]} - \frac{i_f[n_1] - i_f[n_0]}{t[n_1] - t[n_0]} \tag{4.44}$$

$$m_{u_{II}} = \frac{i_f[n_5] - i_f[n_4]}{t[n_5] - t[n_4]} - \frac{i_f[n_4] - i_f[n_3]}{t[n_4] - t[n_3]} \tag{4.45}$$

As shown in (4.44) and (4.45), the current slope by the active voltage vector can be calculated with simple arithmetic operations. In (4.44) and (4.45), the HF response is separated from the fundamental response by subtracting the consecutive current slopes. Since this method does not require frequency demodulation methods, the result is not affected by phase delay problems.

By the geometric relationship in Figure 4.7, the two current slopes in (4.44) and (4.45) can be rewritten as

$$m_{u_I} = \frac{|u_I^*|}{M_{sf}} \cos \Delta\theta_I \tag{4.46}$$

$$m_{u_{II}} = \frac{|u_{II}^*|}{M_{sf}} \cos \Delta\theta_{II} \tag{4.47}$$

Combining (4.44)∼(4.47), $\cos\Delta\theta_I$ and $\cos\Delta\theta_{II}$ can be obtained as

$$\begin{aligned}\cos\Delta\theta_I &= m_{u_I}\frac{M_{sf}}{|u_I^*|}\\ &= (m_{n_2n_1}-m_{n_1n_0})\frac{M_{sf}}{|u_I^*|}\\ &= \left(\frac{i_f[n_2]-i_f[n_1]}{t[n_2]-t[n_1]}-\frac{i_f[n_1]-i_f[n_0]}{t[n_1]-t[n_0]}\right)\frac{M_{sf}}{|u_I^*|}\end{aligned} \tag{4.48}$$

$$\begin{aligned}\cos\Delta\theta_{II} &= m_{u_{II}}\frac{M_{sf}}{|u_{II}^*|}\\ &= (m_{n_5n_4}-m_{n_4n_3})\frac{M_{sf}}{|u_{II}^*|}\\ &= \left(\frac{i_f[n_5]-i_f[n_4]}{t[n_5]-t[n_4]}-\frac{i_f[n_4]-i_f[n_3]}{t[n_4]-t[n_3]}\right)\frac{M_{sf}}{|u_{II}^*|}\end{aligned} \tag{4.49}$$

By (4.31), the $\sin\Delta\theta_I$ is given as

$$\sin\Delta\theta_I = \frac{M_{sf}\frac{m_{u_I}}{|u_I^*|}-2M_{sf}\frac{m_{u_{II}}}{|u_{II}^*|}}{\sqrt{3}} \tag{4.50}$$

Therefore, the actual calculation equation of $\Delta\theta_I$ is derived as

$$\begin{aligned}\Delta\theta_I &= \arctan\left(\frac{\sin\Delta\theta_I}{\cos\Delta\theta_I}\right)\\ &= \arctan\left(\frac{\frac{m_{u_I}}{|u_I^*|}-\frac{2m_{u_{II}}}{|u_{II}^*|}}{\sqrt{3}\frac{m_{u_I}}{|u_I^*|}}\right)\\ &= \arctan\left(\frac{1}{\sqrt{3}}-\frac{2|u_I^*|}{\sqrt{3}|u_{II}^*|}\frac{m_{u_{II}}}{m_{u_I}}\right)\\ &= \arctan\left(\frac{1}{\sqrt{3}}-\frac{2|u_I^*|}{\sqrt{3}|u_{II}^*|}\frac{m_{n_5n_4}-m_{n_4n_3}}{m_{n_2n_1}-m_{n_1n_0}}\right)\end{aligned} \tag{4.51}$$

The rotor position can be estimated with the equation in (4.34) and the calculation result of $\Delta\theta_I$ in equation (4.51). In (4.34), $\angle u_I^*$ is a computed value for vector control in the previous sampling time, hence it is already known when the rotor position is calculated. Therefore, the rotor angle can be estimated with the proposed method.

In the case of the PWM switching of the field winding, the assumption of the constant S_f does not hold for the coinciding stator PWM cycle. Since the rotor switching can distort the slope of

the mutually induced field current, the estimation algorithm does not work, and the estimation result in the previous sampling time is retained for the field winding switching condition. The rotor switching can be shifted not to coincide with the stator switching. Thus the current slope distortion can be avoided. However, the switching shift is not considered in this study for further investigation on the proposed method.

The proposed position estimation method is based on the mutual induction by fundamental PWM switching. From the estimation algorithm, the proposed method has advantages as below:

1. The position estimation can be done in one PWM cycle time, which is 100 μs in this study. Although the slope of the induced field current can be obtained ideally within half PWM cycle, the two slopes are calculated separately in the first and the second half PWM cycle due to the response delay and inverter nonlinearity in practice. Nonetheless, one PWM cycle of the estimation time is much shorter than general signal injection methods.

2. The position estimation equation does not include any model parameters. The mutual inductance of the field winding was introduced at the beginning of the derivation. However, the parameter was canceled out in the fraction form during the derivation. Therefore, the proposed method does not require any parameter information.

3. The derivative of the mutually induced field current, which contains the position information, is obtained by calculating the field current slope. The current slope can be calculated with simple arithmetic operations. Since this method does not require filters or frequency demodulation methods, the phase delay is not present, and the gain tuning process is not necessary.

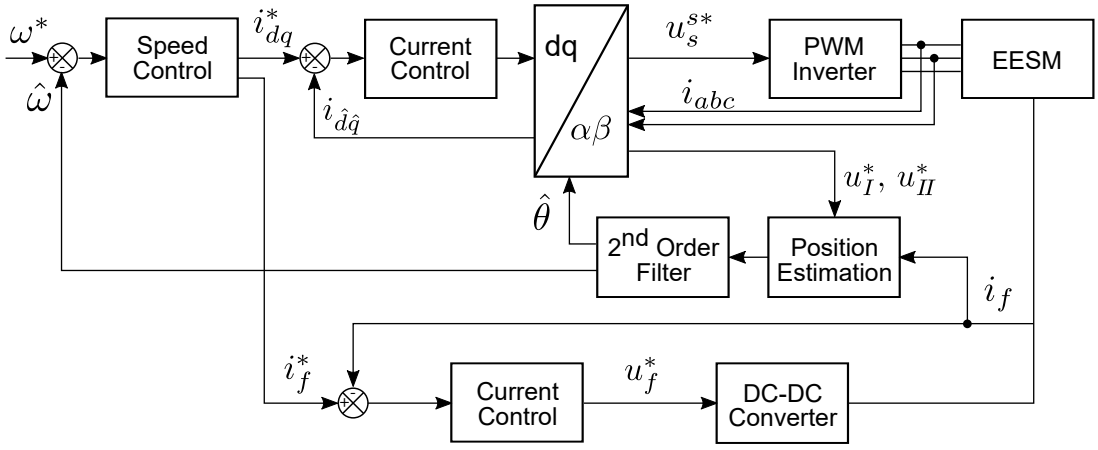

Figure 4.10: Block diagram of the proposed sensorless control method

The block diagram of the proposed sensorless control method is illustrated in Figure 4.10. The control part is a cascade structure of the speed controller and the current controller. The speed controller is a PI controller, and the control outputs are stator current reference and rotor current reference. Both current controllers are PI controllers and operate separately. The rotor position estimation block has input signals of the field current and the active voltage vector references. With the current oversampling and proposed estimation method, the rotor position is estimated and fed back to the speed controller and the reference frame transformation blocks via the second-order tracking type filter. The filter is proposed in [76] and applied to remove noise from the position estimation.

The proposed method has been derived in this section. As shown in the estimation algorithm, the method has a simple algorithm and does not require parameter information. The estimation method has high estimation dynamics to operate in a wide-speed range without combining other methods. The proposed method requires a high bandwidth current sensor and signal processing for the oversampled field current signal. Since the estimation works within one PWM period, practical issues regarding the nonlinearity of PWM switching and high-speed transient response need to be considered. The system hardware configurations and practical issues are explained in the following sections.

4.3 Practical Issues and Modification Methods

An electric machine model expresses the fundamental behavior of mechanical and electrical characteristics of a machine for the sake of stable mechanical operation and simplicity of machine control. As a result, inverter nonlinearities and transient current response by switching devices are not generally considered in the model. The proposed method utilizes the high-speed current response by MOSFET switching, which is not included in the model. Therefore, the high-speed current response is analyzed, and modification of the proposed method is suggested in this section. Additionally, the implementation of the proposed method requires a minimum time of active voltage vector to detect the measurable change of the current slope. Hence, modification methods to guarantee the minimum active time are proposed.

4.3.1 Current response delay

In the proposed method, the rotor position is estimated by the slope of the mutually induced field current. Therefore, detecting the exact time of the current response is crucial in the position estimation performance. In the field current response analysis, there are two dominant delay factors: The first factor is a dead time in between the switching of high-side and low-side of switching devices. The second factor is the current oscillation, which appears after voltage switching. The analysis of the time delay and modification methods are presented in this subsection

In the ideal PWM drive, gate drive signals for a high-side and a low-side MOSFET change simultaneously in a complementary manner. In an actual PWM drive, the dead time is essential to prevent a short circuit in inverter legs. The short circuit can occur without the dead time due to the turn-on delay time, rise time, turn-off delay time, and fall time of a MOSFET. Specifically, since the turn-off delay time is longer than the turn-on delay time, both switches can be on-state in the switching operation. Therefore, the turn-on signal should be delayed by the dead time after the turn-off signal for the other side of a MOSFET is applied. The dead time is illustrated in Figure 4.11.

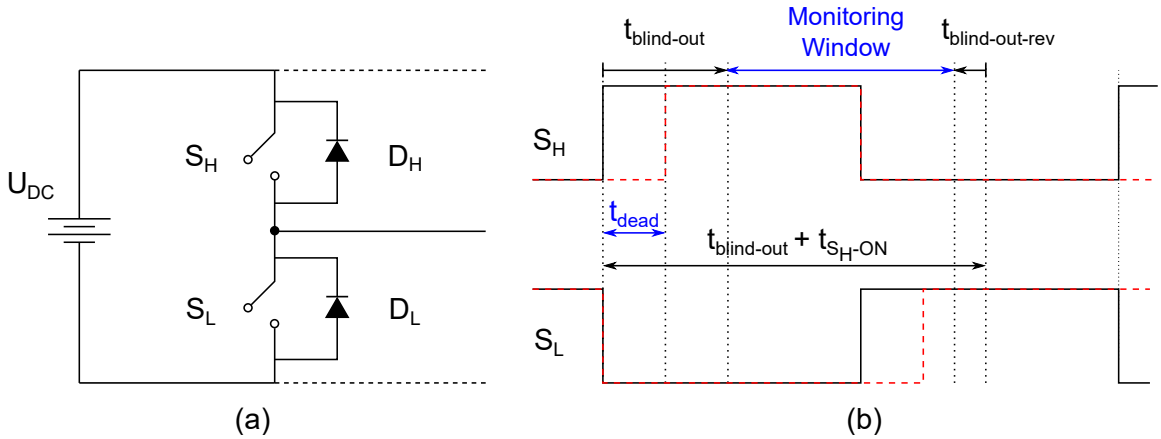

Figure 4.11: Dead time in gate drive signal: (a) conceptual inverter circuit and (b) PWM switching signal and timing sequence

For a conceptual explanation, one leg of a three-phase inverter circuit is shown in Figure 4.11 (a), and the corresponding ideal and actual gate signals are illustrated with a black line and red dashed line in Figure 4.11 (b). The current monitoring concept in the proposed method is also depicted in Figure 4.11 (b). By vector control and SVM algorithm, the gate drive signal is generated as the ideal gate signal. Based on the ideal gate signal, predefined dead time is

inserted by the gate signal drive software in the CPLD. The dead time is set to 2 μs[†].

As a result of the dead time, a current monitoring window needs to be shifted to implement the proposed method. The current monitoring window, in which the mutually induced field current is measured and calculated, coincides ideally with the gate signal command from the SVM algorithm. However, due to the dead time, the current monitoring window should be shifted by the dead time to measure the exact field current response. When the ideal gate signal for S_H is switched on, the actual stator voltage is applied after the dead time. Thus, the start of the current monitoring window is also delayed by the dead time from the ideal gate drive signal. When the gate signal for S_H is switched off, the direction of current flow remains the same by the body diode of a MOSFET. Hence, the end of the current monitoring window is also delayed by the dead time. Consequently, the current monitoring window is shifted by the dead time in implementing the proposed method.

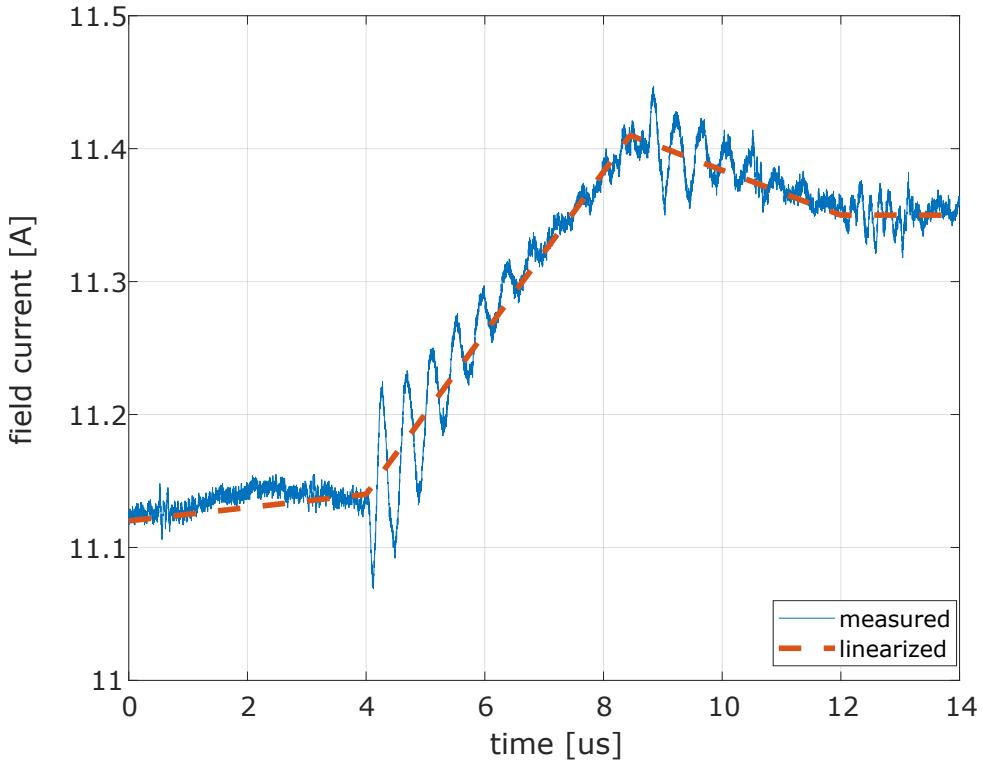

Figure 4.12: Field current oscillation by stator voltage switching

In the transient field current response, current oscillation is found after PWM switching. The measured field current oscillation by stator voltage switching is shown in Figure 4.12. Figure 4.12 shows the measured field current and the linearized field current while the stator

[†]2 μs of dead time in MOSFET drive is longer than general MOSFET drive system. The dead time setting followed the technical manual of the inverter in this study.

voltage is switching. The field current is measured by a current probe, which has 10 MHz bandwidth. The linearized field current is obtained by plotting a straight line in between the field current at the stator voltage switching. In Figure 4.12, as the stator voltage switches, the slope of the linearized signal is changed. In every current slope changing point, the field current oscillation is found. The oscillation occurs due to the parasitic line-to-line and line-to-earth capacitance of cables [77]. Since the current oscillation distorts the current slope calculation, the initial current measurement after the stator voltage switching is ignored. That means the start of the current monitoring window is delayed again. The time delay by the current oscillation is defined by the blind-out time, which was suggested in [77].

The blind-out time is a simple method to prevent the distortion of the current slope calculation by the current oscillation and the dead time for a current oversampling method. In the implementation of the proposed method, the current oversampling method is applied to detect the field current response by the stator voltage switching. The sampling rate is 20 MHz, which means 2,000 samples of field current are measured and processed per one PWM cycle. Since the huge numbers of data cannot be processed and transferred to the Pentium processor in a controller sampling time, the current sampling and the signal processing are handled by the FPGA. Although the blind-out time causes the loss of time to measure the current slope, it reduces the effect of current oscillation in the slope calculation. On the other hand, a 1.5 MHz bandwidth active low pass filter is applied to the current sensor output to reduce noise from the current sensor and the current oscillation.

The stator PWM switching command, field current, and the blind-out time are shown in Figure 4.13. The PWM command and the field current are captured by the SignalTap II Logic Analyzer provided by the FPGA manufacturer. That means the data in Figure 4.13 is identical to the data processed in the FPGA. The blind-out time is marked with gray color and set to 4 μs considering the dead time and the current oscillation. As shown in Figure 4.13, the change of current slope by the stator PWM switching appears clearly after the blind-out time. As a result, the slope calculation of field current is not distorted by the response delay. Also, it is found that the current sensor noise and the current oscillation after the PWM switching are reduced effectively by the active low pass filter.

The current monitoring window is set to 1 μs ($t_{blind-out-rev}$ in Figure 4.11 (b)) shorter than the active time. Ideally, the window size is the same as the active time, however as the turn-off time of a MOSFET is uncertain, the end of the current response can be variable. Therefore, the window size is reduced in the same manner as the blind-out time. The current monitoring concept is shown in Figure 4.11 (b). Figure 4.11 (b) shows the current monitoring window for

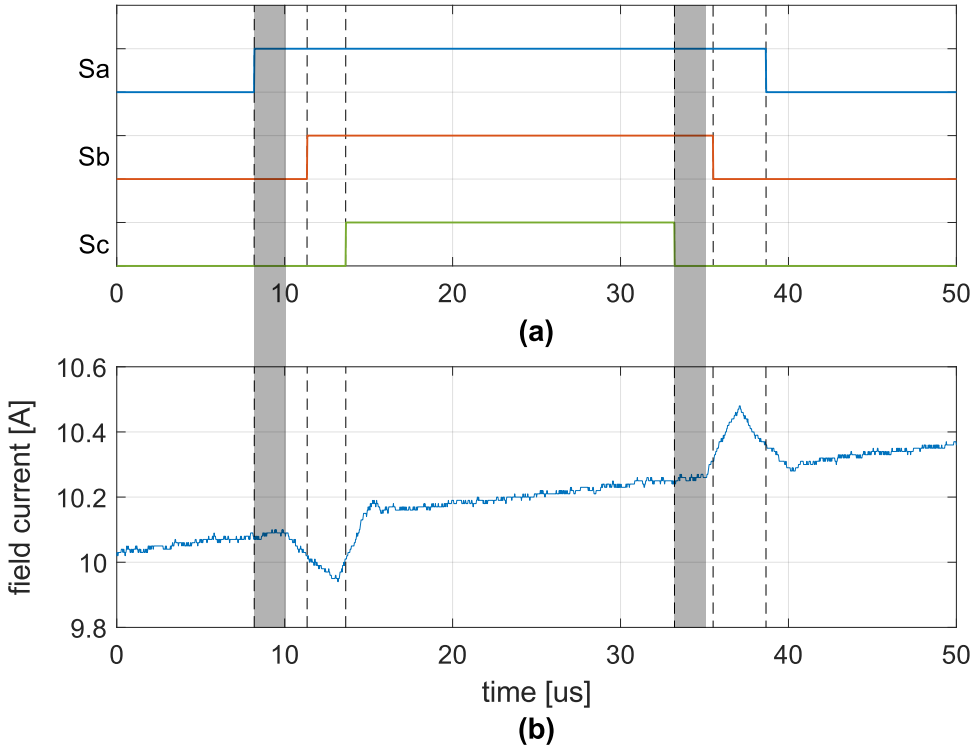

Figure 4.13: Implementation of blind-out time: (a) PWM switching command and (b) field current response

the case $S_H = 1$ only. In the implementation, the monitoring window for the $S_L = 1$ is also applied with the same concept.

4.3.2 Sector transition

The proposed method utilizes two active voltage vectors in the SVM method. Specifically, the mutually induced field current by both active voltage vectors is used as a fraction formula in the rotor position estimation in (4.51). As the inductance parameters are canceled out in the fraction formula, the proposed method can estimate the rotor position without parameter information. Therefore, both active voltage vectors should not be zero to obtain valid results. In the space vector diagram, the reference voltage vector rotates as the rotor rotates. The magnitudes of active voltage vectors with respect to the phase of the reference vector are shown in Figure 4.14.

In Figure 4.14 (a), black, red, and blue arrows represent the stator reference voltage vector, active voltage vector 1, and active voltage vector 2, respectively. While the reference vector is rotating with a constant magnitude value, the magnitudes of active voltage vectors are illustrated

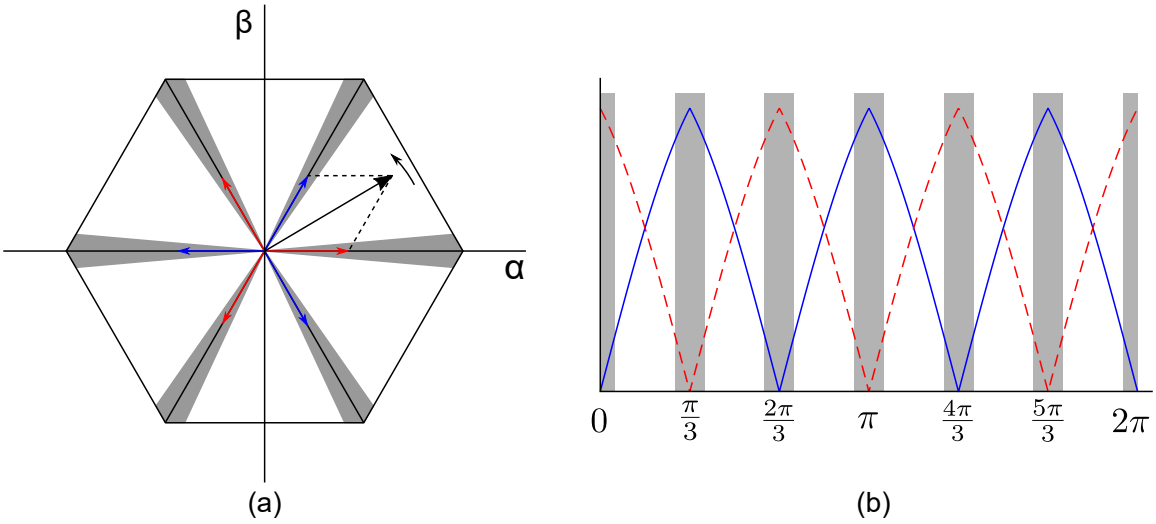

Figure 4.14: Sector transition and magnitude of active voltage vectors: (a) voltage vectors in SVM diagram and (b) magnitude of active voltage vectors

in Figure 4.14 (b). Since the reference vector is applied by a vector sum of two adjacent active vectors, each magnitude of the active vector reduces and increases alternately. When the reference vector is on the edges of a sector in the space vector diagram, the stator reference vector is generated by either active vector. Hence the other active vector is not applied. The sector edges are located at $(n-1)\pi/3$ radians where n is the sector number. In the sector edge area, which is marked with the gray color in Figure 4.14, either active voltage vector has too low magnitude to detect the field current slope. The low magnitude of the active vector means a short active time in the current slope calculation. Considering the blind-out time and the required time to detect the current slope change, the active time needs to be longer than a certain level of time. Therefore, a sector edge avoidance (SEA) method is proposed to guarantee the minimum active time for both active vectors.

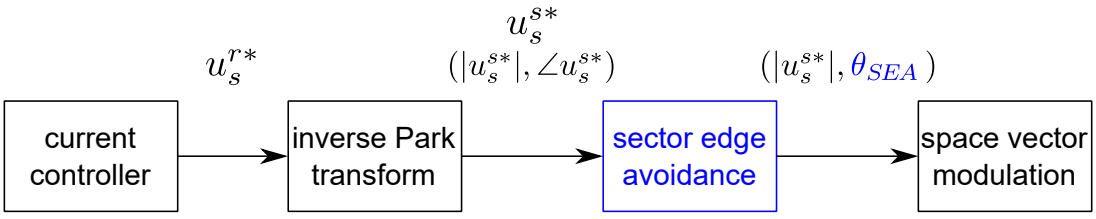

Figure 4.15: Block diagram of sector edge avoidance algorithm

The SEA method shifts the angle of the stator reference voltage vector to the boundary of the sector edge area when the original reference vector is located in the sector edge area. As a result, the SEA method guarantees the minimum active vector time. The method is implemented

between the current controller and the SVM algorithm in the vector control algorithm, as shown in Figure 4.15. The current controller and the inverse park transformation blocks send the stator reference voltage vector to the SEA block. The reference consists of the magnitude and the angle of the reference vector. The SEA algorithm does not modify the magnitude but the angle of the reference vector. The modified angle of the reference vector is given as

$$\theta_{SEA} = \begin{cases} \frac{n\pi}{3} + \theta_{edge}, & \text{if } \frac{n\pi}{3} \leq \angle u_s^{s*} < \frac{n\pi}{3} + \theta_{edge} \\ \frac{n\pi}{3} - \theta_{edge}, & \text{if } \frac{n\pi}{3} - \theta_{edge} < \angle u_s^{s*} < \frac{n\pi}{3} \\ \angle u_s^{s*}, & \text{otherwise} \end{cases} \tag{4.52}$$

where n=0, 1, 2, 3, 4, 5, and θ_{edge} is the boundary angle of the sector edge area. The SEA algorithm guarantees the minimum active time to detect a valid change of field current slope. In terms of the position estimation equation in (4.51), the SEA method can prevent the divergence in calculating the rotor position. In the case of the short active time close to zero, the denominator in (4.32) can become zero. Thus the estimation result can diverge. The boundary angle of the sector edge area needs to be decided with the magnitude of the reference vector. Since the active time is calculated by both magnitude and angle of the reference vector, the boundary angle varies with respect to the magnitude of the reference vector. In this study, θ_{edge} is set to 5°, and the decision of the minimum magnitude of the reference vector is carried out in the following subsection.

The proposed estimation method can be solved by the SEA algorithm in the sector transition region by shifting the angle of the reference voltage vector. However, the angle shift results in the discontinuity of the reference voltage vector. Thus it can cause side effects, i.e., low control efficiency and torque ripples, especially in the low-speed range. Therefore, the threshold needs to be tuned for a better mechanical operation.

4.3.3 Insufficient stator voltage

In the SVM algorithm, the active time is computed from the magnitude and the angle of the reference voltage vector. The relationship between the reference vector and the corresponding active voltage vectors is depicted in Figure 4.16.

The reference voltage vector is a vector sum of the two adjacent active voltage vectors, u_1 and u_2. Therefore, both active vectors can be calculated by vector projection of the reference vector onto each axis of the active vector. The geometrical relationship in Figure 4.16 can be

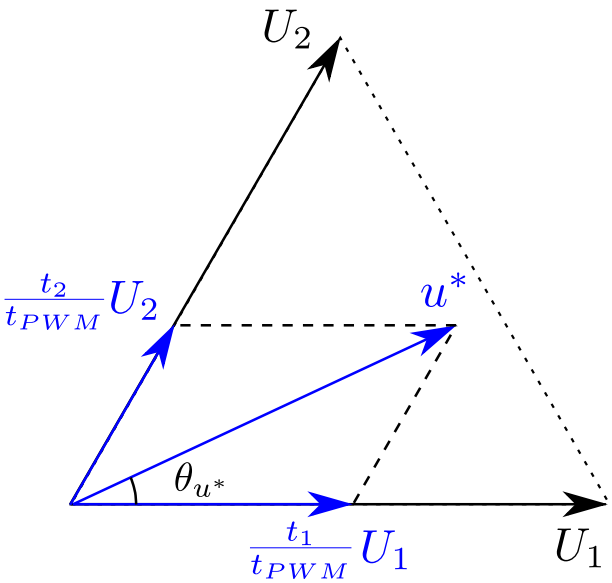

Figure 4.16: Reference voltage vector and active voltage vectors in SVM Diagram

expressed as

$$u^* = \frac{t_1}{t_{PWM}}U_1 + \frac{t_2}{t_{PWM}}U_2 \tag{4.53}$$

Supposing the reference voltage vector is in sector 1, t_1 and t_2 are given as

$$t_1 = t_{PWM}\frac{|u^*|}{\frac{2}{3}U_{DC}}\frac{\sin\left(\frac{\pi}{3} - \theta_{u^*}\right)}{\sin\frac{\pi}{3}} \tag{4.54}$$

$$t_2 = t_{PWM}\frac{|u^*|}{\frac{2}{3}U_{DC}}\frac{\sin\theta_{u^*}}{\sin\frac{\pi}{3}} \tag{4.55}$$

where θ_{u^*} is the angle of the reference vector. In sector 1, θ_{u^*} is bounded as $0 \leq \theta_{u^*} < \pi/3$.

As shown in (4.54) and (4.55), the active time is proportional to the magnitude of the stator reference voltage vector. Therefore, the low magnitude of the stator reference voltage vector appears as a short active time in the PWM switching sequence. In the low-speed region, the stator voltage level is low. Hence it yields short active time. The short active time needs to be longer than a certain time, considering the blind-out time and minimum time to measure a detectable change of field current. Otherwise, the insufficient active time results in an inaccurate calculation of the current slope. Therefore, a signal injection method is required to increase the active time.

Pulsating signal injection in the stator reference frame is proposed in this study. The main purpose of the signal injection is the extension of active time in the PWM switching sequence, and the concept of the proposed method is shown in Figure 4.17.

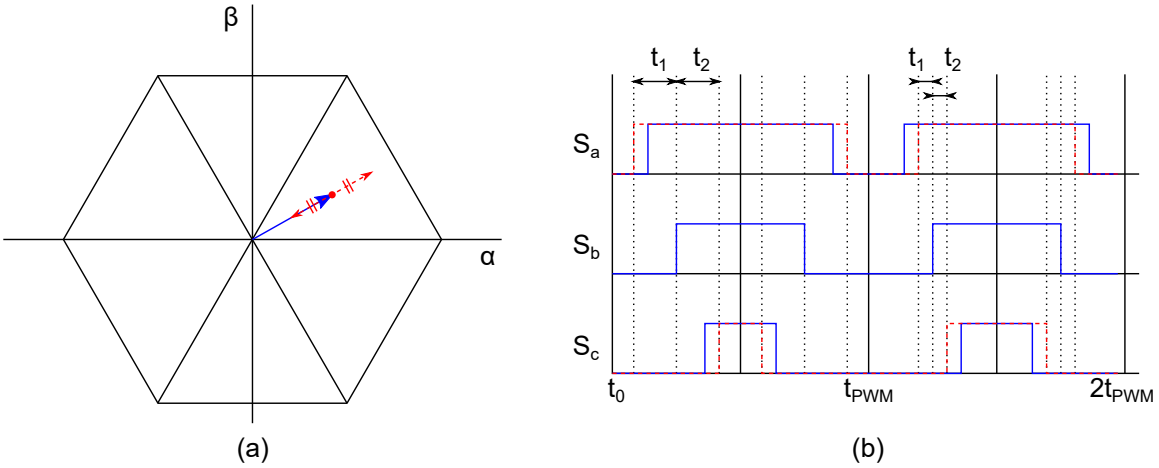

Figure 4.17: Signal injection concept: (a) in space vector diagram and (b) in PWM switching sequence

In Figure 4.17 (a), the blue line represents the fundamental reference voltage vector, and the red line represents the pulsating signal injection in the space vector diagram. Figure 4.17 (b) shows the gate signal for the fundamental reference vector and the signal injected reference vector with a blue line and a red dashed line in the PWM switching sequence. The pulsating signal is injected on the fundamental reference voltage with changing the sign of the signal in every PWM period. Therefore, the frequency of the pulsating signal is half of the PWM frequency. As shown in Figure 4.17 (b), the active time is increased in the first PWM period ($t_0 \sim t_{PWM}$) and decreased in the second period ($t_{PMW} \sim 2t_{PWM}$). The field current slope is calculated in the first PWM period, as well as the position estimation. In the second PWM period, the calculation result in the previous period is held without calculating a new current slope due to insufficient active time. The injected pulsating signal is expressed as

$$\boldsymbol{u}_{inj} = \begin{cases} (-1)^{k-1} \left(|U_{min}| - |\boldsymbol{u}^*| \right) \angle \boldsymbol{u}^*, & \text{if } |\boldsymbol{u}^*| < |U_{min}| \\ 0, & \text{otherwise} \end{cases} \tag{4.56}$$

where k and U_{min} represent the number of PWM cycles and the minimum magnitude of reference voltage vector to obtain field current derivative. The pulsating signal is injected when the fundamental reference voltage is less than U_{min}, and the calculation of the current slope works if k is an odd number. When the fundamental reference voltage is bigger than U_{min}, the signal

injection is not activated, and the position estimation is computed in every PWM cycle.

The value of U_{min} can be decided by considering the minimum active time. To calculate valid current slope, at least 1 μs of the current monitoring window is required under the sensor noise. Additionally, 1 μs reduction of the current monitoring window needs to be included in the minimum active time. Therefore, the minimum active time is set to 2 μs in the implementation of the proposed method. From the (4.54) and (4.55), the calculation result of U_{min} is 6.36 volts when the stator reference vector is on the boundary of the sector edge area. In the implementation, U_{min} is set to 7 volts.

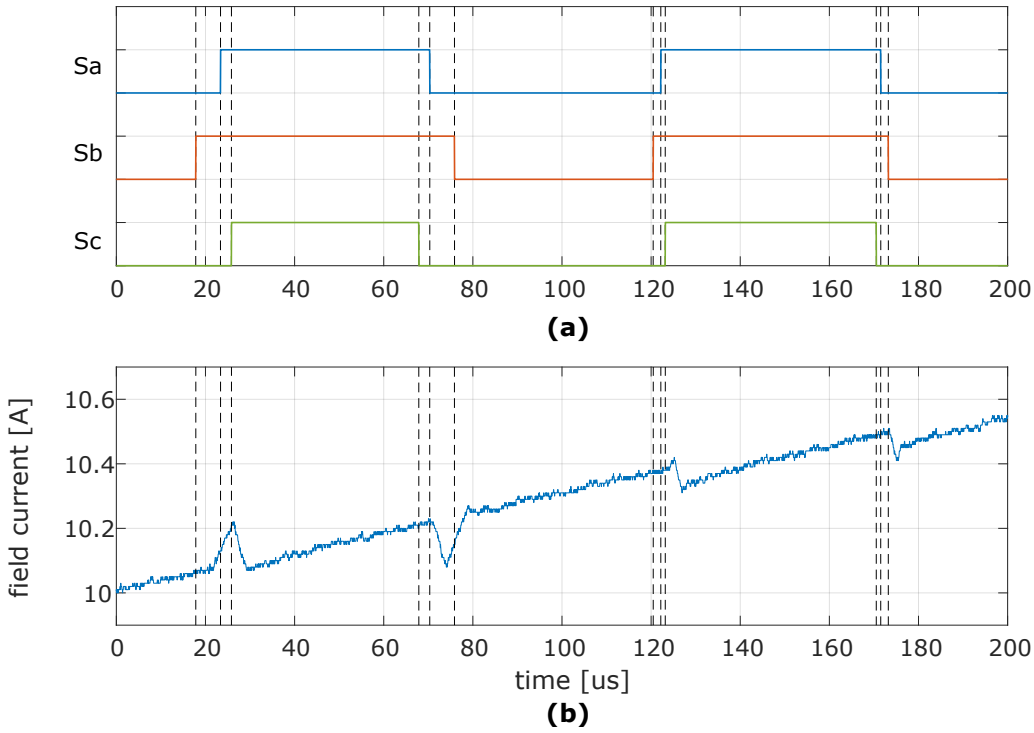

Figure 4.18: Experimental result of signal injection: (a) PWM switching sequence and (b) field current response

The proposed signal injection method is implemented in the position estimation method, and the injection signal and the corresponding field current are shown in Figure 4.18. The PWM switching signal and the field current are captured by FPGA for two PWM cycles. In the first cycle, the positive signal is injected. Thus the increase of active time is found. As a result, the slope of the field current shows a clear response in the cycle. In the second cycle, the active time is decreased as the negative signal is injected. Still, the change of the current slope is found in the second cycle. However, the current slope is not used since the insufficient active time

can yield an inaccurate estimation result. From Figure 4.18, it is found that the signal injection increased the active time and the change of field current while the current slope was maintained. It is advantageous to the current slope calculation, considering current response delay and signal noise. Therefore, the proposed signal injection method is applied to the sensorless control method in this study.

Regarding expected side effects of the proposed signal injection method, acoustic noise increases as the HF signal is injected. The noise occurs in the low-speed range, where the active time is insufficient. From the middle-speed range, the signal injection is not activated. Thus the acoustic noise by the signal injection disappears. On the other hand, the magnitude of the injection signal can be reduced with respect to the phase of the reference vector. Since the purpose of the signal injection is the minimum active time, the magnitude of the injection signal can vary with the reference vector angle. In terms of the mechanical operation, the signal injection does not affect mechanical operation since the injected signal frequency is much higher than the machine rotation speed, especially in the low-speed range. Also, the fundamental reference voltage remains the same as the original reference since the average value of the injection signal is zero. Hence, the effect of signal injection on the mechanical operation is insignificant.

The proposed signal injection differs from conventional signal injection methods: First, the pulsating signal is commonly injected in the estimated rotor reference frame, where amplitude modulation is the main estimation principle. However, the proposed method injects the signal in the stator reference frame to extend the active time from the PWM switching sequential point of view. Second, the frequency of the injected signal, half of a PWM frequency, is higher than the frequency of the conventional signal injection method, which is usually in the range of several hundred Hz to a few kHz [49]. It is beneficial to design a current controller, which is connected to the signal injection block in a cascade control structure. Due to the high frequency of the injected signal, the proposed method limits the bandwidth of a current controller less than conventional signal injection methods.

4.3.4 Field current adjustment

The proposed method exploits the change of field current, and the current change is emerged by mutual induction between stator and rotor windings. In terms of the signal-to-noise ratio (SNR), the more field current difference is induced, the higher SNR is obtained. Therefore, the relationship between the induced field current difference and the magnitude of field current is investigated. From the relationship, a field current adjustment method is suggested in this

subsection.

In the derivation of the proposed method, the derivative of field current by stator voltage switching is expressed in (4.15). Neglecting the stator voltage input and rotor position term, (4.15) shows the relationship between the derivative of field current and mutual inductance as

$$\frac{di_f}{dt} \propto \frac{1}{M_{sf}} \tag{4.57}$$

(4.57) shows that the derivative of field current is inverse proportional to the mutual inductance. Based on this property, the stator voltage input and the rotor position decide the field current response, as shown in (4.15). Therefore, the mutual inductance affects the basic field current response.

According to the identification of mutual inductance of EESM in 2.3.2, the mutual inductance decreases as the field current increases. The relationship is expressed as

$$M_{sf} \propto \frac{1}{|i_f|} \tag{4.58}$$

Due to the saturation effect in the field winding, the mutual inductance is inverse proportional to the magnitude of field current. Summarizing (4.57) and (4.58), the relationship between the derivative of field current and the magnitude of field current is given as

$$\frac{di_f}{dt} \propto |i_f| \tag{4.59}$$

Therefore, it is expected that the derivative of field current is increased as the magnitude of field current increases. To verify the relationship in (4.59), the difference of mutually induced field current (Δi_f) by stator voltage switching is measured. In the measurement, EESM is rotated by a load machine at 1,000 rpm, and the stator reference voltage is given as: $|u_s^{s*}| = 5$ (V), $\angle u_s^{s*} = 30°, 210°$. The experimental result is shown in Figure 4.19.

Figure 4.19 shows the difference of field current by stator voltage switching. Δi_{f_I} and $\Delta i_{f_{II}}$ are difference of mutually induced field current by active voltage vectors, u_I and u_{II}, and they are defined as

$$\Delta i_{f_I} = i_f[n_2] - i_f[n_1] \tag{4.60}$$

$$\Delta i_{f_{II}} = i_f[n_5] - i_f[n_4] \tag{4.61}$$

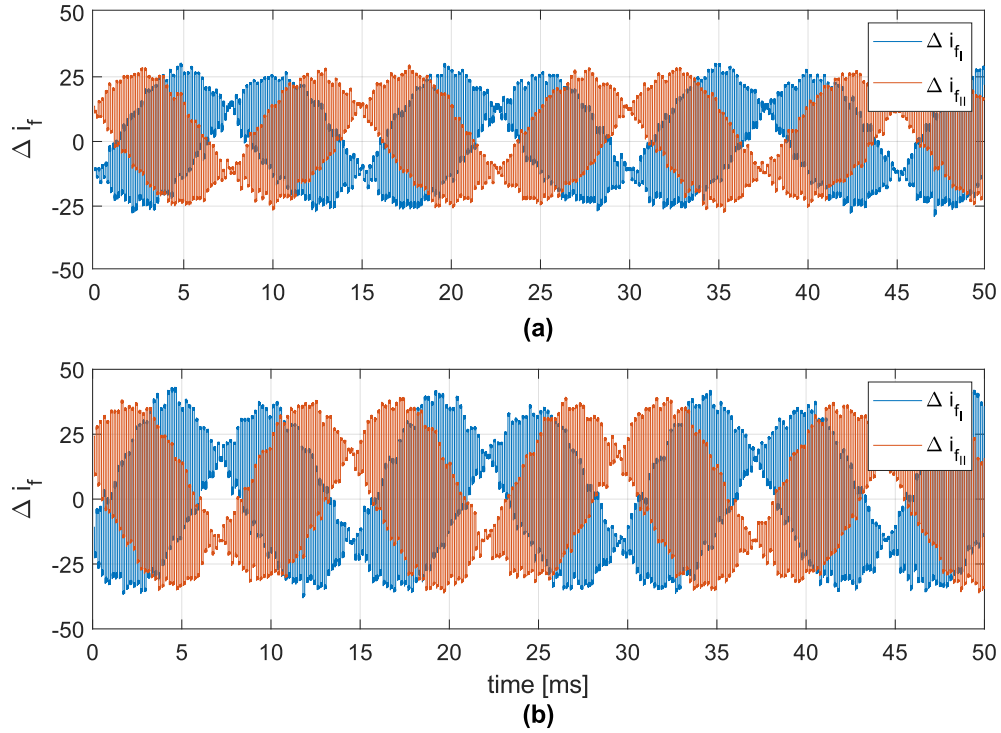

Figure 4.19: Difference of field current (Δi_f) by stator voltage switching: (a) $i_f = 5$ A and (b) $i_f = 10$ A

where $[n_n]$ represents the time index for current sampling, which was introduced in Figure 4.9.

The field current is controlled to 5 A and 10 A in Figure 4.19 (a) and (b). Except for the magnitude of the field current, other conditions, e.g., stator reference voltage, rotor position, and rotor speed, are the same in Figure 4.19 (a) and (b). As the stator voltage alternates 30 ° and 210 ° with PWM frequency, the difference of field current results in positive and negative values alternately with the PWM frequency. In both results, the patterns of the field current difference are the same, but the field current difference in Figure 4.19 (b) is about 30 % bigger than the results in Figure 4.19 (a). This results satisfies the relationship in (4.59). Therefore, it can be concluded that the difference of the mutually induced field current is proportional to the magnitude of field current, and it is due to the saturation effect in the field winding.

Considering the general sensor noise, the increase of the mutually induced field current is beneficial to SNR. Hence, the sensorless control performance can be improved by increasing the magnitude of the field current. However, the magnitude of field current is related to copper loss in the field winding. Therefore, the field current needs to be optimized in between the sensorless control performance and the copper loss of field winding. In this study, the field

current is controlled to 10 A. However, there is a chance to improve the sensorless control method by adjusting the field current in case of the low mutually induced field current.

4.4 Test Bench Hardware Configuration

The test bench for the proposed method consists of EESM, a real-time system controller, two inverters, high-speed current sensors, and a load machine. The picture of the test bench is shown in Figure 4.20.

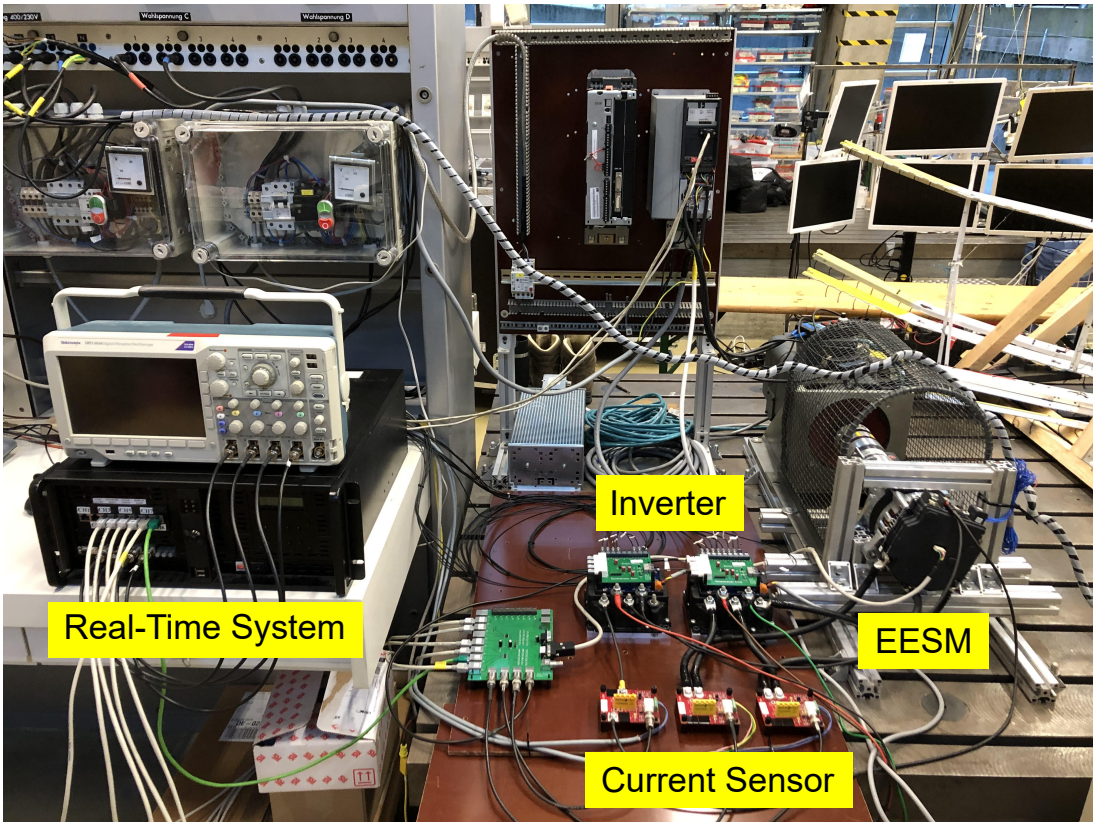

Figure 4.20: Picture of the test bench for sensorless EESM drive

In order to implement and validate the proposed method, a test bench for sensorless EESM drive has been built, as shown in Figure 4.20. The main requirements for the test bench are given as

- Three-phase PWM drive with 10 kHz frequency
- Field winding PWM drive with 1 kHz frequency

- High-speed Analog-to-Digital Converter (ADC) and signal processing for current oversampling
- 48-volt system

The EESM installed in the test bench has three-phase stator windings and one rotor winding. To drive the machine, two general-purpose 48-volt inverters are used, and each inverter is connected to the stator and the rotor winding separately. Three current sensors measure two phase stator current and field current, and the measured signal is feedback to the controller. The real-time system computes the rotor position and EESM vector control with protection functions, such as phase and field winding over current and DC over voltage protections. The load machine and the inverter for the load machine apply load torque to the EESM. Technical data of the test bench are given in Appendix C.

The real-time system consists of a Pentium processor, a field-programmable gate array (FPGA) board, and a complex programmable logic device (CPLD) board. The block diagram of the real-time system is illustrated in Figure 4.21.

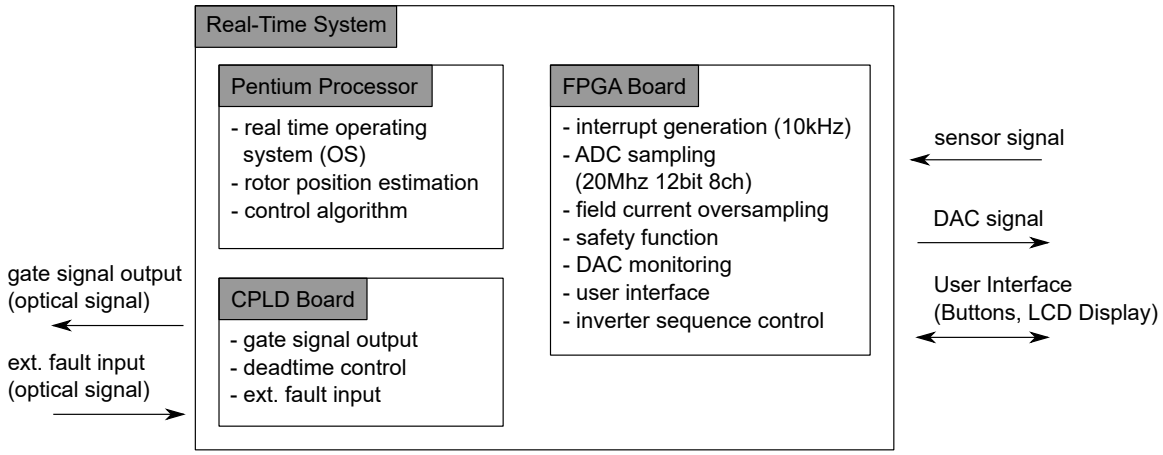

Figure 4.21: Block diagram of real-time system

The Pentium processor has two main tasks: First, the real-time operating system (RTOS) runs on the Pentium processor, and the RTOS manages data processing within a bounded time. Second, the Pentium processor computes the proposed position estimation algorithm and the sensorless vector control algorithm. Sensor input data and control output data are transferred from/to the FPGA board via CPLD Board. The Pentium processor used in the test is the Pentium 4 CPU 3.40 GHz.

The FPGA board plays a main role in the real-time system. It handles system clocks and generates the interrupt signal for the control algorithm in the Pentium processor. Sensor in-

put signals are sampled in the FPGA with a 20 MHz sampling rate. Thanks to the parallel computing structure, the FPGA can handle the current oversampling and related signal processing within a sampling time. Also, safety functions, such as over current protection, over voltage protection, and computing overload protection, are carried out in the FPGA. For the interface with users and inverters, peripheral devices (e.g., buttons, an LCD, a digital to analog (D/A) board) drive and the inverter sequence control are handled by the FPGA. The Cyclone III FPGA is used in the test.

The CPLD is in charge of the interface between the Pentium processor and the FPGA board. It has optical transmitters to drive inverters. The PWM output computed by the FPGA is transferred to the CPLD, and the signal is converted to the optical signal with a dead time processing. External fault signals from inverters are connected to the optical receivers in CPLD to protect the system from an inverter failure. The CPLD used in the test is the MAX II CPLD.

Detailed information regarding other components of the test bench is as below:

- Inverter
  - The inverter used in the test bench is a general-purpose inverter manufactured by Semikron. The nominal DC-link voltage is 48 volt, and the maximum power is up to 55 kW. It is a three-phase two-level inverter, and a metal-oxide-semiconductor field-effect transistor (MOSFET) is used as a switching device. One inverter is connected to the stator windings, and the other is connected to the rotor winding. The rotor winding drive circuit is an H-bridge circuit, and the circuit is composed by using the two legs of the inverter. The electric circuit diagram is depicted in Figure 4.22.
- Current sensor
  - The main hardware requirement of the proposed method is a high-bandwidth current sensor. Since current oversampling is required for the calculation of the current derivative, high-speed current sensing is mandatory. The current sensors used in the experiment are CMS3025 and CMS3100 manufactured by Sensitec. The sensor is based on the magnetoresistive effect, and the maximum bandwidth is 2 MHz. Considering the 10 kHz PMW frequency, the current sensor bandwidth is 200 times faster than the PWM switching frequency. Two current sensors (CMS3100) are used for stator current measurement, and one current sensor (CMS3025) is used for rotor current measurement as shown in Figure 4.22.
- EESM

  - The machine has a salient pole rotor structure and does not have damper winding in the rotor. DC current is applied to the rotor winding via brush and slip ring. The stator winding is a distributed winding type. Further information is given in Appendix B.

- Load machine and inverter

  - The load machine is ABB BSM100C-4150AA. The rated torque is 20 Nm, and the maximum peak torque is 60 Nm. The inverter for the load machine is ABB ACS880-11. The maximum output power is 17 kW.

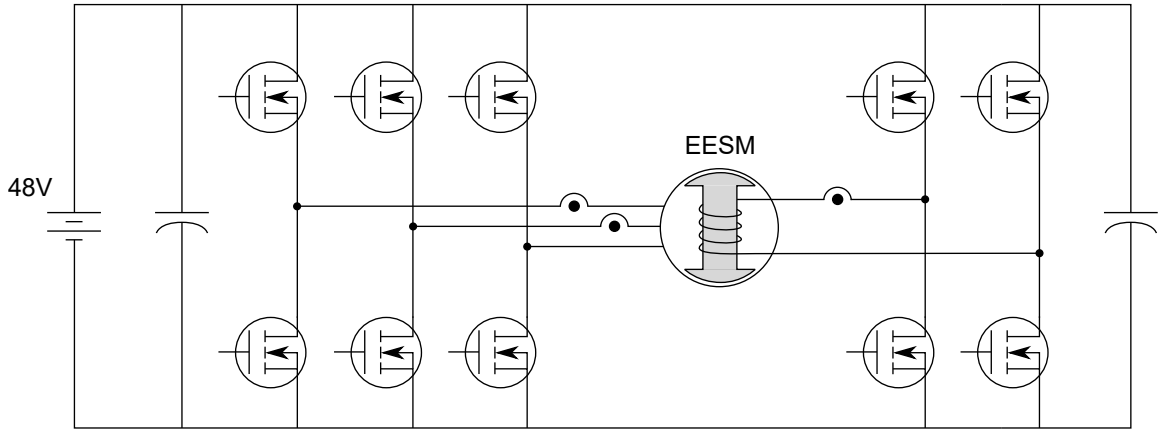

Figure 4.22: Electric Circuit Diagram of EESM Drive

4.5 Experimental Results

The proposed sensorless control method with modification methods was validated with experimental results. The rated speed of the EESM in this study is 1,850 rpm. A step speed reference from 0 to the rated speed under no load condition was tested to validate the wide-speed operation range. The experimental result is shown in Figure 4.23.

As shown in Figure 4.23, the proposed sensorless control method has driven the machine from a stationary to the rated speed, 1,850 rpm. The maximum transient estimation error at the beginning of the rotation is 0.89 radian, and the average value of the absolute estimation error in the constant rotor speed range is 0.09 radian. The biggest error in the transient estimation error is expected to occur due to the dynamic change of the stator current, but the rotor speed reached the reference speed in about 1.5 s.

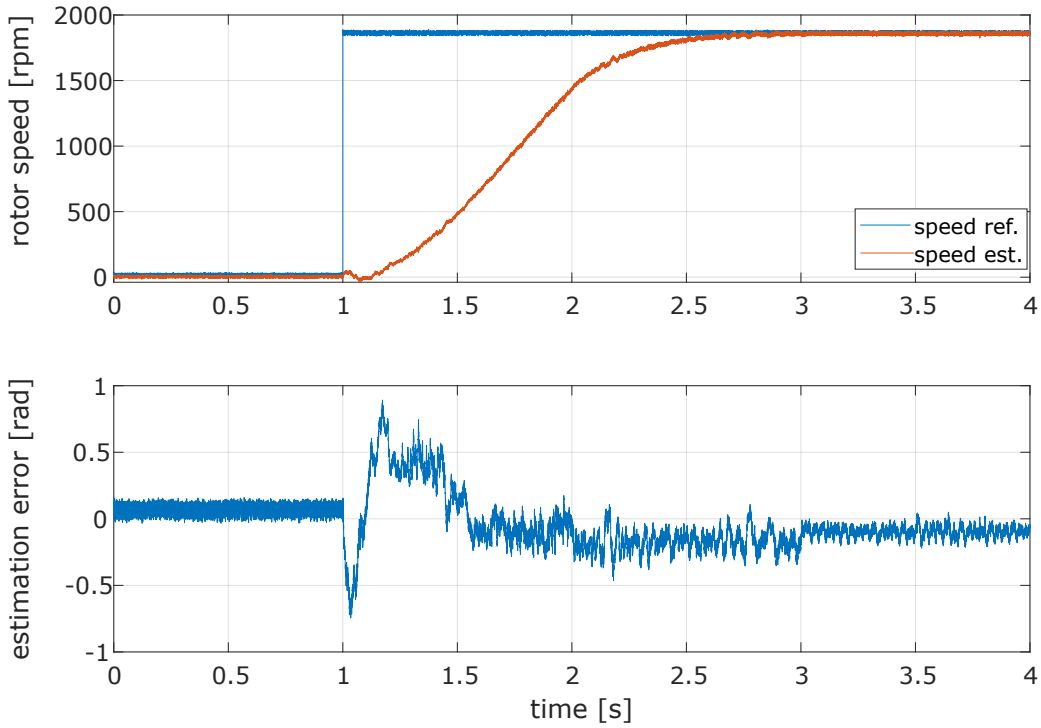

Figure 4.23: Sensorless speed control from a standstill to the rated speed

To validate the bidirectional operation and the zero speed control performance, reverse rotation from 1,000 rpm to -1,000 rpm under no load condition was tested, and the experimental result is shown in Figure 4.24.

Figure 4.24 shows sensorless control performance in reverse rotation under no load condition. The maximum estimation error is -1.1 radian, and it occurred around zero speed. When the rotor speed is in the constant speed range, $0 \sim 1$ and $2 \sim 3$ s, the average estimation error is 0.04 radian. The estimation error was increased around zero speed. However, the proposed method has controlled the machine in reverse rotation without divergence.

Finally, the proposed sensorless control was validated in a load condition. The rated torque of the test machine is 10.5 Nm. The experimental result of the sensorless control in a 100 % load condition is shown in Figure 4.25. The load torque was applied from 2 s and reached the rated torque at around 4.5 s. The rated torque was decreased to 0 Nm from about 8 s to 10.5 s. The field current was controlled to 10 A for the load condition. Maximum torque per ampere (MTPA) control was not implemented in the test. To utilize the reactance torque for the full load condition, d-axis current was controlled to -10 A. During the test the estimated q-axis current reached up to 150 A in the load condition. The maximum estimation error was 1.18 rad and occurred while the load torque was decreasing from the rated torque. The average value of the

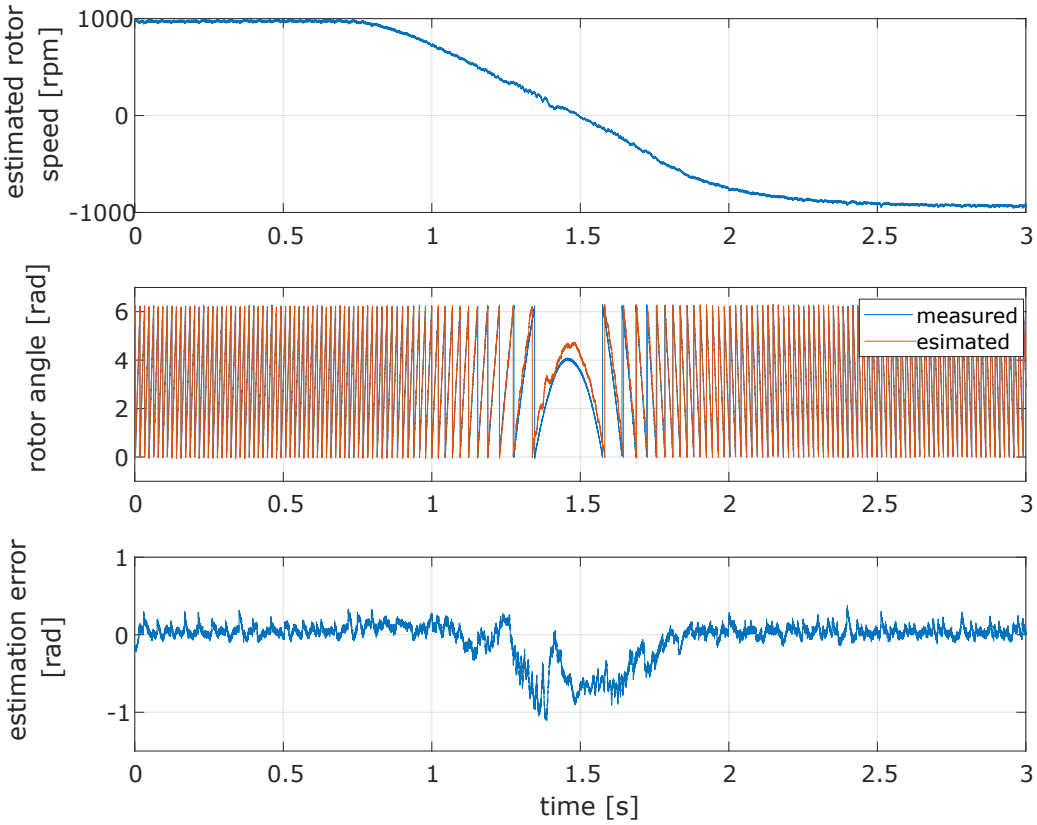

Figure 4.24: Sensorless speed control in reverse rotation

absolute estimation error during the rated torque was 0.38 radian. The period of the rated torque condition is from 4.5 to 8 s. In comparison with the estimation error in the rated speed under no load condition, the average estimation error was increased from 0.09 to 0.38 rad. However, the estimation error was limited under certain level without any divergence. As a result, the sensorless speed control has worked in the 100 % load condition.

In this section, the proposed sensorless control is validated experimentally in zero to rated speed, reverse rotation, and load condition. During the sensorless control, the position estimation error was increased in the transient, but the sensorless speed control worked without divergence. In the steady-state operation, the estimation error converged in limited error range. Consequently, the proposed method achieved satisfactory performance in various test conditions.

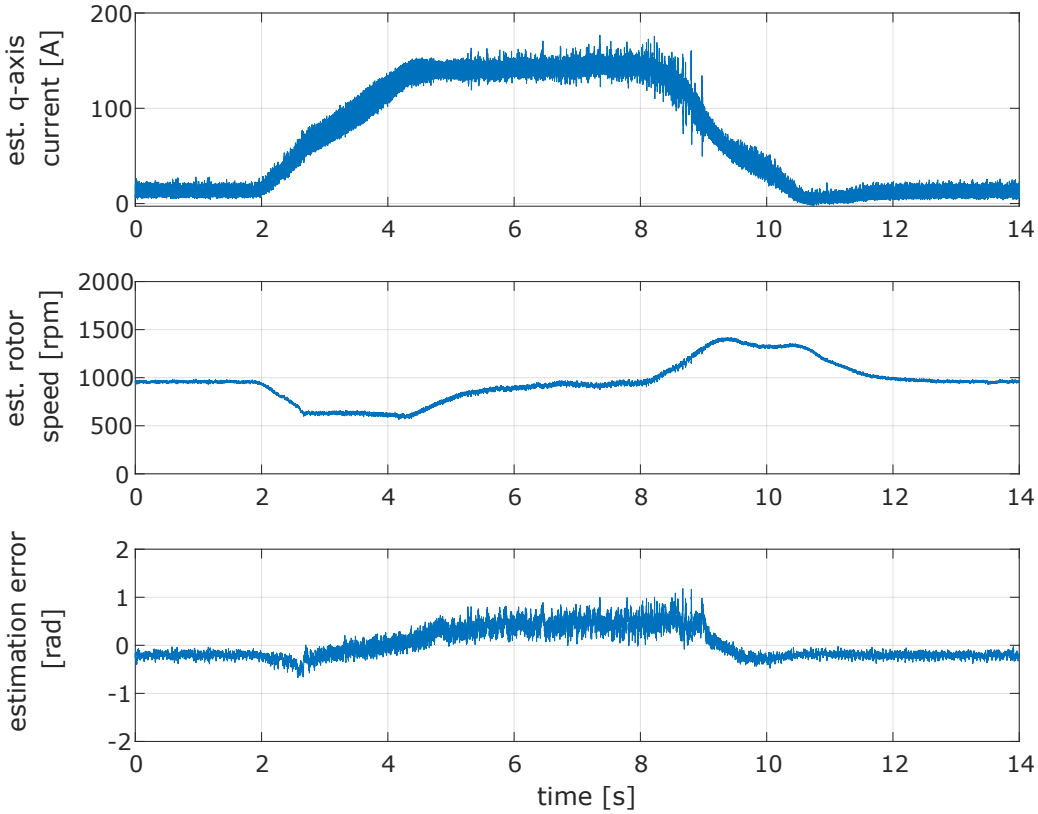

Figure 4.25: Sensorless speed control in a load condition

CHAPTER 5

Conclusion

The PWM-based sensorless control of EESM using mutual induction was proposed, implemented, and validated in this thesis. Based on the characteristic that the mutual inductance is a function of the rotor position, the mutually induced field current was exploited to estimate the rotor position. To extract the mutually induced field current from the fundamental field current signal, a fundamental stator PWM switching signal was employed as an excitation signal. The field current response by the PWM excitation was calculated with the oversampling process and the signal processing, which consists of simple arithmetic operations. As a result, the HF mutual induction components in the field current were obtained and used in the position estimation. In the realization of the proposed method, three dominant practical issues were analyzed, and related modification methods were suggested:

- The current response delay due to the nonlinearity of the inverter and the current oscillation were analyzed, and the current monitoring window was redefined by the blind-out time.
- The sector edge avoidance was applied to prevent the divergence of the position estimation around the sector edge area.
- The signal injection method was used to extend the insufficient active time in the low-speed range.

The proposed estimation method and modification methods were implemented in the real-time system consisting of a Pentium processor, an FPGA, and a CPLD. To detect the HF field current response, a 2 MHz high bandwidth magnetoresistive sensor was used to measure the mutually induced field current. The experimental results validated the proposed sensorless control method for a zero speed to the rated speed operation, a reverse rotation, and a full load condition. The proposed sensorless control showed a bigger estimation error in a transient state compared to the existing methods. However, the sensorless speed control was achieved in various conditions without divergence.

Based on the estimation principle and algorithm, the proposed method has advantages as follows.

- The proposed method utilizes the mutually induced field current by the active voltage vector in SVM. Therefore, the position can be estimated within one PWM cycle or two PWM cycles if the signal injection is applied due to the insufficient stator voltage. This high dynamic estimation results in a wide-speed range sensorless control with a single algorithm. The high dynamics is also beneficial to the design of the current controller. Due to the half PWM frequency signal injection, the bandwidth of the current controller is limited to less than general signal injection methods.

- The proposed method does not rely on any model parameter information. As the inductance parameters were canceled out in the derivation of the estimation algorithm, the rotor position could be estimated only with the reference voltage and current derivative. Therefore, the algorithm does not need measurements of inductance for a LUT nor a parameter identification method. Besides, the proposed method does not require a polarity check algorithm nor an initial position detection method since this method is based on the structural saliency of EESM.

- The HF field current was extracted from the fundamental current response by simple arithmetic operations in the proposed method. Therefore, complex frequency demodulation methods or signal filters are not required.

For the realization, the proposed method requires a special system configuration. A high bandwidth current sensor and high-speed signal processing are mandatory to detect the current response by active voltage vectors. Thus, the estimation algorithm and related current sampling methods need more optimization in order to apply the proposed method with a conventional system configuration.

In terms of the position estimation error, the proposed method resulted in a bigger error than existing sensorless control methods, especially for the transient state. Also, the modification methods, signal injection, and sector edge avoidance can cause a reduction of the control performance and efficiency, especially for the low-speed range. However, those disadvantages can be overcome by improving the signal processing of the mutually induced field current. By signal reconstruction or effective noise suppression, the derivative of the field current can be obtained in a short period of time. Therefore, the modification methods may not be required by improving the signal processing method.

The EESM gives more freedom to the design of sensorless control methods. The interaction between the stator and rotor winding can be employed in both the excitation and the detection of position-related saliencies. The proposed method provides a novel perspective in the design of the sensorless control of EESM. As a result, it was proved that the mutual induction by the fundamental PWM excitation can be used in the sensorless control of EESM.

APPENDIX A

Abbreviations

AC	Alternating Current
ADC	Analog to Digital Converter
AFO	Active Flux Observer
BPF	Bandpass Filter
CPLD	Complex Programmable Logic Device
D/A	Digital to Analog
DC	Direct Current
DO	Disturbance Observer
DSP	Digital Signal Processor
EESM	Electrically Excited Synchronous Machine
EKF	Extended Kalman Filter
EMF	Electromotive Force
EV	Electric Vehicle
FEA	Finite Element Analysis
FEM	Finite Element Method
FFT	Fast Fourier Transform
FOC	Field-Oriented Control

FPGA	Field-Programmable Gate Array
HF	High-Frequency
IC	Integrated Circuit
IM	Induction Machine
IPMSM	Interior Permanent Magnet Synchronous Machine
LPF	Low Pass Filter
LUT	Lookup Table
MOSFET	Metal-Oxide-Semiconductor Field-Effect Transistor
MRAS	Model Reference Adaptive System
MTPA	Maximum Torque per Ampere
PLL	Phase-Locked Loop
PM	Permanent Magnet
PWM	Pulse-Width Modulation
R2S	Rotor to Stator
RDC	Resolver-to-Digital Converter
RTOS	Real-Time Operating System
S2R	Stator to Rotor
S2S	Stator to Stator
SEA	Sector Edge Avoidance
SNR	Signal-to-Noise Ratio
SVM	Space Vector Modulation
SynRM	Synchronous Reluctance Machine
WFSM	Wound Field Synchronous Machine
WRSM	Wound Rotor Synchronous Machine

APPENDIX B

EESM Parameters

The EESM used in the experiment is a salient pole type EESM. It is a prototype machine to develop a mild hybrid system for a vehicle. Parameters and information of the EESM are summarized in Table B.1.

The picture of EESM used in this thesis is shown in Figure B.1. The EESM has an external diameter of 165 mm, and the length is 110 mm. The machine is connected to a crankshaft of the engine via a rubber belt. For the belt connection, a pulley is attached at the end of the rotor shaft of EESM.

Figure B.2 shows a picture of a rotor structure of EESM used in the test. The rotor has 8

Parameter	Value
Maximum Power	10 kW
Maximum Torque	43.2 Nm (@ 1,850 rpm)
Maximum Speed	12,000 rpm
Number of Poles	8
Stator Resistance	4.37 $m\Omega$
Rotor Resistance	1,035 $m\Omega$
Stator Inductance	11.69 μH
Rotor Inductance	25.79 μH
Moments of Inertia	4.5 gm^2

Table B.1: List of EESM parameters

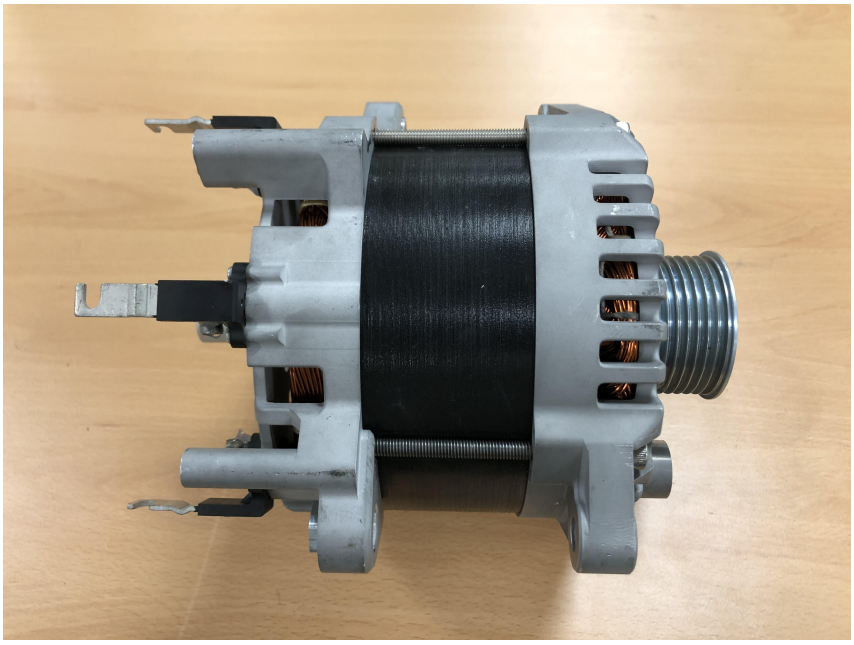

Figure B.1: Picture of EESM

poles, and the slip ring is found in the rotor shaft. The diameter of the rotor is 103 mm, and its length is 46 mm.

Figure B.2: Picture of EESM rotor

APPENDIX C

Technical Data of Test Bench

C.1 Current Sensor

The current sensors used for the test bench are CMS3025 and CMS3100. Both models are highly dynamic sensors based on the magnetoresistance effect and produced by Sensitec GmbH. CMS3025 and CMS3100 are used to measure the field current and stator current of EESM. The technical data of the sensors for the field winding and the stator winding are summarized in Table C.1 and Table C.2.

Model	Parameter	Value
CMS3025	Supply Voltage	Typical $\pm$ 15 V
	Nominal Current	25 A
	Measuring Range	- 100 $\sim$ 100 A
	Frequency Bandwidth	Minimum 2 MHz
	Typical Accuracy	$\pm$ 0.6 $\%$ of nominal current
	Maximum Accuracy	$\pm$ 0.8 $\%$ of nominal current

Table C.1: Technical data of current sensor for field winding

Model	Parameter	Value
CMS3100	Supply Voltage	Typical $\pm$ 15 V
	Nominal Current	100 A
	Measuring Range	- 400 $\sim$ 400 A
	Frequency Bandwidth	Minimum 1.5 MHz, typical 2.0 MHz
	Typical Accuracy	$\pm$ 0.8 $\%$ of nominal current
	Maximum Accuracy	$\pm$ 1.3 $\%$ of nominal current

Table C.2: Technical data of current sensor for stator winding

Parameter	Value
Nominal DC voltage	48 V
Maximum DC voltage	72 V
Continuous output current	270 Arms
Overload output current	460 Arms
DC bus capacitor	14.4 mF
Switching frequency	Maximum 24 kHz
Ambient temperature	-40 $\sim$ 85 $^{\circ}C$

Table C.3: Technical data of inverter

C.2 Inverter

The inverter used in this dissertation is SKAI3 LV manufactured by SEMIKRON. SKAI3 LV is a 48 V three-phase MOSFET inverter. Two SKAI3 LV inverters are used to drive EESM: one for three-phase stator winding and the other for rotor winding. A brief technical data of the inverter are summarized in Table C.3.

C.3 Load machine

The load machine used in the test is ABB BSM100C-4150AA. The machine type is a PMSM, and the technical data is given in Table C.4.

Parameter	Value
Continuous stall torque	20 Nm
Continuous stall current	16.8 Arms
Rated power	4.48 kW
Rated speed	2,400 rpm
Peak current	42.9 Arms
Maximum speed	7,000 rpm

Table C.4: Technical data of load machine

List of Figures

List of Tables

Bibliography

[1] T. Jahns, "Getting rare-earth magnets out of EV traction machines: A review of the many approaches being pursued to minimize or eliminate rare-earth magnets from future EV drivetrains," *IEEE Electrification Magazine*, vol. 5, no. 1, pp. 6–18, mar 2017.

[2] F. Un-Noor, S. Padmanaban, L. Mihet-Popa, M. Mollah, and E. Hossain, "A comprehensive study of key electric vehicle (EV) components, technologies, challenges, impacts, and future direction of development," *Energies*, vol. 10, no. 8, aug 2017.

[3] D. G. Dorrell, "Are wound-rotor synchronous motors suitable for use in high efficiency torque-dense automotive drives?" in *IECON 2012 - 38th Annual Conference on IEEE Industrial Electronics Society*, 2012.

[4] I. Boldea, L. N. Tutelea, L. Parsa, and D. Dorrell, "Automotive electric propulsion systems with reduced or no permanent magnets: An overview," *IEEE Transactions on Industrial Electronics*, vol. 61, no. 10, pp. 5696–5711, oct 2014.

[5] S. Estenlund, M. Alakula, and A. Reinap, "PM-less machine topologies for EV traction: A literature review," in *2016 International Conference on Electrical Systems for Aircraft, Railway, Ship Propulsion and Road Vehicles & International Transportation Electrification Conference (ESARS-ITEC)*, 2016.

[6] J. K. Noland, S. Nuzzo, A. Tessarolo, and E. F. Alves, "Excitation system technologies for wound-field synchronous machines: Survey of solutions and evolving trends," *IEEE Access*, vol. 7, 2019.

[7] M. Koteich, A. Messali, and S. Daurelle, "Self-sensing control of the externally-excited synchronous machine for electric vehicle traction application," in *2017 IEEE International Symposium on Sensorless Control for Electrical Drives (SLED)*, 2017.

[8] T. Muneer, R. Milligan, I. Smith, A. Doyle, M. Pozuelo, and M. Knez, "Energetic, environmental and economic performance of electric vehicles: Experimental evaluation," *Transportation Research Part D: Transport and Environment*, vol. 35, pp. 40–61, mar 2015.

[9] W. Liu, *Hybrid Electric Vehicle System Modeling andControl 2nd edition*. Wiley, Mar. 2017. [Online]. Available: https://www.ebook.de/de/product/26873558/wei_liu_hybrid_electric_vehicle_system_modeling_andcontrol_2e.html

[10] A. Emadi, *Advanced Electric Drive Vehicles*. CRC Press, Taylor & Francis Group, 2015.

[11] G. Friedrich, "Experimental comparison between wound rotor and permanent magnet synchronous machine for integrated starter generator applications," in *2010 IEEE Energy Conversion Congress and Exposition*, 2010.

[12] B. Koo, I. Jeong, and K. Nam, "12 slot - 10 pole excited synchronous motor design for ISG applications," in *2014 International Conference on Electrical Machines (ICEM)*, 2014.

[13] C. Rossi, D. Casadei, A. Pilati, and M. Marano, "Wound rotor salient pole synchronous machine drive for electric traction," in *Conference Record of the 2006 IEEE Industry Applications Conference 41st IAS Annual Meeting*, 2006.

[14] L. Huang, Z. Zhu, and W. Chu, "Optimization of electrically excited synchronous machine for electrical vehicle applications," in *8th IET International Conference on Power Electronics, Machines and Drives (PEMD 2016)*, 2016.

[15] J. Tang, "Design and control of electrically excited synchronous machines for vehicle applications," Ph.D. dissertation, Chalmers University of Technology, 2021.

[16] J. de Santiago, H. Bernhoff, B. Ekergård, S. Eriksson, S. Ferhatovic, R. Waters, and M. Leijon, "Electrical motor drivelines in commercial all-electric vehicles: A review," *IEEE Transactions on Vehicular Technology*, vol. 61, no. 2, pp. 475–484, feb 2012.

[17] H. Krupp and A. Mertens, "Rotary transformer design for brushless electrically excited synchronous machines," in *2015 IEEE Vehicle Power and Propulsion Conference (VPPC)*, 2015.

[18] A. D. Gioia, I. P. Brown, Y. Nie, R. Knippel, D. C. Ludois, J. Dai, S. Hagen, and C. Alteheld, "Design and demonstration of a wound field synchronous machine for electric vehicle traction with brushless capacitive field excitation," *IEEE Transactions on Industry Applications*, vol. 54, no. 2, pp. 1390–1403, mar 2018.

[19] M. Maier and N. Parspour, "Operation of an electrical excited synchronous machine by contactless energy transfer to the rotor," *IEEE Transactions on Industry Applications*, vol. 54, no. 4, pp. 3217–3225, 2018.

[20] J. Tang and Y. Liu, "Comparison of copper loss minimization and field current minimization for electrically excited synchronous motor in mild hybrid drives," in *2017 19th European Conference on Power Electronics and Applications (EPE'17 ECCE Europe)*, 2017.

[21] J. Choi, I. Jeong, K. Nam, and S. Jung, "Sensorless control for electrically energized synchronous motor based on signal injection to field winding," in *IECON 2013 - 39th Annual Conference of the IEEE Industrial Electronics Society*, 2013.

[22] A. Rambetius and B. Piepenbreier, "Sensorless control of wound rotor synchronous machines using the switching of the rotor chopper as a carrier signal," in *2013 IEEE International Symposium on Sensorless Control for Electrical Drives and Predictive Control of Electrical Drives and Power Electronics (SLED/PRECEDE)*, 2013.

[23] J. Schuster, V. Ketchedjian, and J. Roth-Stielow, "Sensorless position estimation for an externally excited synchronous machine over the whole speed range," in *PCIM Europe 2018; International Exhibition and Conference for Power Electronics, Intelligent Motion, Renewable Energy and Energy Management*, 2018.

[24] A. Rambetius, S. Ebersberger, M. Seilmeier, and B. Piepenbreier, "Carrier signal based sensorless control of electrically excited synchronous machines at standstill and low speed using the rotor winding as a receiver," in *2013 15th European Conference on Power Electronics and Applications (EPE)*, 2013.

[25] A. Rambetius and B. Piepenbreier, "Sensorless control of wound field synchronous machines for the whole speed range," in *Proceedings of PCIM Europe 2015; International Exhibition and Conference for Power Electronics, Intelligent Motion, Renewable Energy and Energy Management*, 2015.

[26] I. Boldea, G. Andreescu, C. Rossi, A. Pilati, and D. Casadei, "Active flux based motion-sensorless vector control of DC-excited synchronous machines," in *2009 IEEE Energy Conversion Congress and Exposition*, 2009.

[27] Y. Hua, M. Sumner, G. Asher, Q. Gao, and K. Saleh, "Improved sensorless control of a permanent magnet machine using fundamental pulse width modulation excitation," *IET Electric Power Applications*, vol. 5, no. 4, 2011.

[28] D. Paulus, P. Landsmann, and R. Kennel, "General arbitrary injection approach for synchronous machines," in *2013 IEEE International Symposium on Sensorless Control for Electrical Drives and Predictive Control of Electrical Drives and Power Electronics (SLED/PRECEDE)*, 2013.

[29] S. Kim, J.-I. Ha, and S.-K. Sul, "PWM switching frequency signal injection sensorless method in IPMSM," *IEEE Transactions on Industry Applications*, vol. 48, no. 5, pp. 1576–1587, sep 2012.

[30] S.-K. Sul, *Electric Machine Drive Systems*. John Wiley & Sons, Inc., 2010.

[31] P. Krause, O. Wasynczuk, S. Sudhoff, and S. Pekarek, *Analysis of Electric Machinery and Drive Systems*. John Wiley & Sons, Inc., 2013.

[32] D. Schröder, *Elektrische Antriebe - Grundlagen Mit durchgerechneten Übungs- und Prüfungsaufgaben*, 6th ed. Springer Berlin Heidelberg, 2013.

[33] Y. Zhou and Y. Hu, "A novel direct torque control for electrically excited synchronous motor drives with high power factor and low ripples in flux and torque," in *2008 IEEE Power Electronics Specialists Conference*, 2008.

[34] I. Jeong, J. Kim, Y. Kim, and K. Nam, "Extended MTPA with cross coupling inductances for electrically excited synchronous motors," in *2013 IEEE Energy Conversion Congress and Exposition*, 2013.

[35] D. Uzel and Z. Peroutka, "Optimal vector control for wound rotor salient pole synchronous motors over full speed range," in *2015 17th European Conference on Power Electronics and Applications (EPE'15 ECCE-Europe)*, 2015.

[36] Y. Kim and K. Nam, "Copper-loss-minimizing field current control scheme for wound synchronous machines," *IEEE Transactions on Power Electronics*, vol. 32, no. 2, pp. 1335–1345, Feb. 2017.

[37] A. Girardin and G. Friedrich, "Optimal control for a wound rotor synchronous starter generator," in *Conference Record of the 2006 IEEE Industry Applications Conference Forty-First IAS Annual Meeting*, 2006.

[38] M. Margner and W. Hackmann, "Control challenges of an externally excited synchronous machine in an automotive traction drive application," in *2010 Emobility - Electrical Power Train*, 2010.

[39] O. Haala, B. Wagner, M. Hofmann, and M. Marz, "Optimal current control of externally excited synchronous machines in automotive traction drive applications," *International Journal of Electrical and Computer Engineering*, vol. 7, no. 9, 2013.

[40] R. Wang, M. Bash, and S. D. Pekarek, "Excitation strategies for a wound rotor synchronous machine drive," in *SAE Technical Paper Series*. SAE International, 2014.

[41] W. Q. Chu, Z. Q. Zhu, J. Zhang, X. Liu, D. A. Stone, and M. P. Foster, "Investigation on operational envelops and efficiency maps of electrically excited machines for electrical vehicle applications," *IEEE Transactions on Magnetics*, vol. 51, no. 4, pp. 1–10, apr 2015.

[42] Q. K. Nguyen, J. Schuster, and J. Roth-Stielow, "Energy optimal control of an electrically excited synchronous motor used as traction drive," in *2015 9th International Conference on Power Electronics and ECCE Asia (ICPE-ECCE Asia)*, 2015.

[43] I. Jeong, "Flux linkage modeling and torque calculation by fourier series and taylor series expansion," Ph.D. dissertation, Department of Electronics and Electrical Engineering, Pohang University of Science of Technology, 2015.

[44] O. Laldin, S. D. Sudhoff, and S. Pekarek, "An analytical design model for wound rotor synchronous machines," *IEEE Transactions on Energy Conversion*, vol. 30, no. 4, pp. 1299–1309, dec 2015.

[45] M. Mabhula and M. Kamper, "Saliency and mutual inductance effect in cylindrical wound-rotor synchronous motor," in *2017 IEEE Workshop on Electrical Machines Design, Control and Diagnosis (WEMDCD)*, 2017.

[46] C. Paul, *Inductance : Loop and Partial*. Wiley IEEE, 2010.

[47] T. A. Lipo, *Analysis of Synchronous Machines*. CRC Press, 2012.

[48] M. Pacas, "Sensorless drives in industrial applications," *IEEE Industrial Electronics Magazine*, vol. 5, no. 2, pp. 16–23, jun 2011.

[49] F. Briz and M. Degner, "Rotor position estimation," *IEEE Industrial Electronics Magazine*, vol. 5, no. 2, pp. 24–36, jun 2011.

[50] P. Jansen and R. Lorenz, "Transducerless position and velocity estimation in induction and salient AC machines," *IEEE Transactions on Industry Applications*, vol. 31, no. 2, pp. 240–247, 1995.

[51] J.-I. Ha and S.-K. Sul, "Sensorless field orientation control of an induction machine by high frequency signal injection," in *IAS '97. Conference Record of the 1997 IEEE Industry Applications Conference Thirty-Second IAS Annual Meeting*, 1997.

[52] M. Corley and R. Lorenz, "Rotor position and velocity estimation for a salient-pole permanent magnet synchronous machine at standstill and high speeds," *IEEE Transactions on Industry Applications*, vol. 34, no. 4, pp. 784–789, 1998.

[53] M. Linke, R. Kennel, and J. Holtz, "Sensorless speed and position control of synchronous machines using alternating carrier injection," in *IEEE International Electric Machines and Drives Conference, 2003. IEMDC'03.*, 2003.

[54] S.-I. Kim, J.-H. Im, E.-Y. Song, and R.-Y. Kim, "A new rotor position estimation method of IPMSM using all-pass filter on high-frequency rotating voltage signal injection," *IEEE Transactions on Industrial Electronics*, vol. 63, no. 10, pp. 6499–6509, oct 2016.

[55] M. Laumann, C. Weiner, and R. Kennel, "Arbitrary injection based sensorless control with a defined high frequency current ripple and reduced current and sound level harmonics," in *2017 IEEE International Symposium on Sensorless Control for Electrical Drives (SLED)*, 2017.

[56] G.-D. Andreescu, C. Pitic, F. Blaabjerg, and I. Boldea, "Combined flux observer with signal injection enhancement for wide speed range sensorless direct torque control of IPMSM drives," *IEEE Transactions on Energy Conversion*, vol. 23, no. 2, pp. 393–402, jun 2008.

[57] S.-C. Agarlita, I. Boldea, and F. Blaabjerg, "High-frequency-injection-assisted "active-flux"-based sensorless vector control of reluctance synchronous motors, with experiments from zero speed," *IEEE Transactions on Industry Applications*, vol. 48, no. 6, pp. 1931–1939, nov 2012.

[58] F. J. W. Barnard, W. T. Villet, and M. J. Kamper, "Hybrid active-flux and arbitrary injection position sensorless control of reluctance synchronous machines," *IEEE Transactions on Industry Applications*, vol. 51, no. 5, pp. 3899–3906, sep 2015.

[59] Z. Chen, "Sensorless control of permanent magnet synchronous machines with multiple saliencies," Ph.D. dissertation, Technical University Munich, 2016.

[60] S.-K. Sul, Y.-C. Kwon, and Y. Lee, "Sensorless control of IPMSM for last 10 years and next 5 years," *CES Transactions on Electrical Machines and Systems*, vol. 1, no. 2, pp. 91–99, 2017.

[61] K. H. Nam, *AC Motor Control and Electrical Vehicle Applications*. CRC Press, 2018.

[62] A. Rambetius and B. Piepenbreier, "Carrier signal based sensorless control of wound field synchronous machines using the rotor winding as the receiver: Rotating vs. alternating carrier," in *Proceedings of PCIM Europe 2015*, 2015.

[63] X. Deng, L. Wang, J. Zhang, and Z. Ma, "Rotor position detection of synchronous motor based on high-frequency signal injection into the rotor," in *2011 Third International Conference on Measuring Technology and Mechatronics Automation*, 2011.

[64] D. Uzel, V. Smidl, and Z. Peroutka, "Resolver motivated sensorless rotor position estimation of wound rotor synchronous motors with kalman filter," in *IECON 2013 - 39th Annual Conference of the IEEE Industrial Electronics Society*, 2013.

[65] R. M. Llorente, *Practical Control of Electric Machines*. Springer-Verlag GmbH, 2020. [Online]. Available: https://www.ebook.de/de/product/38780881/ruben_molina_llorente_practical_control_of_electric_machines.html

[66] A. Griffo, D. Drury, T. Sawata, and P. H. Mellor, "Sensorless starting of a wound-field synchronous starter/generator for aerospace applications," *IEEE Transactions on Industrial Electronics*, vol. 59, no. 9, pp. 3579–3587, sep 2012.

[67] A. Rambetius and B. Piepenbreier, "Comparison of carrier signal based approaches for sensorless wound rotor synchronous machines," in *2014 International Symposium on Power Electronics, Electrical Drives, Automation and Motion*, 2014.

[68] S. Morimoto, K. Kawamoto, M. Sanada, and Y. Takeda, "Sensorless control strategy for salient-pole PMSM based on extended EMF in rotating reference frame," *IEEE Transactions on Industry Applications*, vol. 38, no. 4, pp. 1054–1061, jul 2002.

[69] A. Rambetius, S. Luthardt, and B. Piepenbreier, "Speed estimation and compensation for harmonics in sensorless wound rotor synchronous machines," in *2014 IEEE 5th International Symposium on Sensorless Control for Electrical Drives*, 2014.

[70] E. Sariyildiz, R. Oboe, and K. Ohnishi, "Disturbance observer-based robust control and its applications: 35th anniversary overview," *IEEE Transactions on Industrial Electronics*, vol. 67, no. 3, pp. 2042–2053, mar 2020.

[71] S. Li, J. Yang, W.-H. Chen, and X. Chen, *Disturbance Observer-based Control : Methods and Applications*. CRC Press, Taylor & Francis Group, 2014.

[72] P. Dai, Y. Lv, N. Xu, and H. Xie, "Speed sensorless control of electrically excited synchronous motor based on the reduce-order state observer flux observation," in *2016 IEEE 11th Conference on Industrial Electronics and Applications (ICIEA)*, 2016.

[73] M. Koteich, A. Maloum, G. Duc, and G. Sandou, "Observability analysis of sensorless synchronous machine drives," in *2015 European Control Conference (ECC)*, 2015.

[74] S.-H. Kim, *Electric Motor Control: DC, AC, and BLDC Motors*. Elsevier Science Publishing Co Inc, 2017.

[75] H. B. Chung and R. Kennel, "PWM-based sensorless control of electrically excited synchronous machine using mutual inductance," in *2020 International Symposium on Power Electronics, Electrical Drives, Automation and Motion (SPEEDAM)*, 2020.

[76] D. Paulus, J.-F. Stumper, and R. Kennel, "Sensorless control of synchronous machines based on direct speed and position estimation in polar stator-current coordinates," *IEEE Transactions on Power Electronics*, vol. 28, no. 5, pp. 2503–2513, may 2013.

[77] P. Landsmann, "Sensorless control of synchronous machines by linear approximation of oversampled current," Ph.D. dissertation, Technical University Munich, 2014.